High Resolution Scanning Probes of Ferroelectric Thin Films

by

Hongzhou Ma

B.S, Beijing University, Department of Physics, 1991

M.S, University of Pittsburgh, Department of Physics and Astronomy, 2001

Submitted to the Graduate Faculty of

University of Pittsburgh in partial fulfillment

of the requirements for the degree of

Doctor of Philosophy

University of Pittsburgh

2007

UNIVERSITY OF PITTSBURGH

Faculty of Arts and Science

This dissertation was presented

by Hongzhou Ma

It was defended on

March 21st, 2007

and approved by

Jeremy Levy, Professor, Physics and Astronomy

Hrvoje Petek, Professor, Physics and Astronomy

Robert Coalson, Professor, Chemistry and Physics

Xiaolun Wu, Professor, Physics and Astronmy

Gilbert Walker, Professor, Chemistry, University of Toronto

Dissertation Advisor: Jeremy Levy, Professor, Physics and Astronomy

High Resolution Scanning Probes of Thin Film Ferroelectrics

Hongzhou Ma, PhD

University of Pittsburgh, 2007

Advances in materials growth techniques enable precise control over the growth of novel functional materials such as ferroelectric thin films, which are interesting from both a physics and applications perspective. Physical properties of ferroelectric thin films differ a lot from their bulk counterparts, mainly due to the lattice mismatch at the film-substrate interface and differential thermal contraction experienced during growth. Those property anomalies are confined to a narrow range usually thinner than 1000 nm. High-resolution probes are important for understanding the spatial and temporal properties of these systems. We have developed mechanical and optical scanning probe techniques and used them to investigate various strain-engineered ferroelectric thin films. These optical and scanning probe techniques are designed to detect ferroelectric domain dynamics. Our experimental results either give direct evidence to verify material functionality, or reveal the relation between nano-scale dynamics to their macroscopic properties.

TABLE OF CONTENTS

LIST OF FIGURES

PREFACE

Ferroelectrics are dielectric materials that below a certain temperature range exhibit spontaneous electric polarization. This polarization may be reversed by applying an electric field above a certain value known as the coerce field.

Thin film ferroelectric materials are interesting from both a technological and scientific perspective. Their nonlinear dielectric and optical properties are useful in a variety of applications. The thickness of thin film ferroelectrics is usually below 1 micrometer. As a consequence, the voltage required to perform either polarization reversal or dielectric constant tuning can be made small. This property makes it a good candidate for modern electronics which require low voltages and small size. Ferroelectrics are piezoelectric, which means that strain couples to electric fields; for this reason ferroelectric materials are commonly used in microelectromechanical systems (MEMS) such as ultrasonic micromotors. Pyroelectricity is another useful property that relates to the change of polarization with temperature; this effect is used for infrared detectors. The remnant polarization is used for the next generation of high-density nonvolatile Ferroelectric Random Access Memories (FeRAM). The large tunability of the dielectric constant with voltage is used for frequency-agile microwave electronics.

In this thesis, our focus has been on observing and understanding nanoscale domain dynamics in ferroelectric thin films using a combination of scanning probe and optical microscopies. Many interesting properties were revealed. 1) Lattice-scale domain dynamics detected by piezoforce microscopy (PFM); 2) Nanometer-scale domain patterning of ferroelectric/silicon heterostructures was performed and measured; 3) Electro-optic measurements were performed on $SrTiO_3/DyScO_3$ using Confocal Scanning Optical Microscopy (CSOM); 4) A time-resolved Apertureless Near-Field Scanning Optical Microscope (ANSOM) was developed which provides sub 10ps temporal and sub-50 nm spatial resolution; this instrument was used for nanoscale dynamic imaging of ferroelectric films. Our work

demonstrates a way to directly view the complex nanoscale domain structures and dynamics associated with various macroscopic properties of thin film ferroelectrics.

This work was supported by the DARPA FAME and National Science Foundation through grants DMR-0103354 and DMR-0333192

1.0 INTRODUCTION

Ferroelectric materials represent a category of polar dielectrics which possess at least two thermodynamically stable electric polarization states in the absence of externally applied electric fields. These polarization states are referred to as "spontaneous" because they appear and are stable in the absence of any external driving field. By applying an electric field, the polarization state can be switched. Figure 1 shows schematically what a typical dielectric hysteresis loop looks like. After being exposed to an external electric field E that is greater than the coercive field E_c, the ferroelectric will be poled. A non-zero remnant polarization P_r remains when the electric field is removed, provided that the temperature is below the ferroelectric phase transition temperature T_c. By applying an opposing electric field larger in magnitude than the coercive field E_c, the polarization can be reversed.

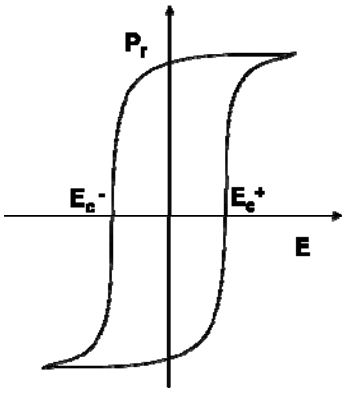

Figure 1 Schematic of dielectric hysteresis loop for a ferroelectric exposed to external switching electric field

A particular class of ferroelectrics relevant to this thesis possesses the perovskite structure, as depicted in Fig. 2. Its relatively simple composition and structure (ABO_3) give rise to a wide class of interesting ferroelectric, magnetic and other properties. The name of perovskite structure is derived from the mineral "perovskite" whose composition is Calcium Titanium

Oxide ($CaTiO_3$). In an ABO_3 structure, the A site consists of a monovalent or divalent metallic atom, while the B site is tetravalent or pentavalent. O represents Oxygen atoms located at the center of each of the six faces of the unit cell. The symmetry of this lattice structure is a result of the equilibrium relevant to thermodynamics, electric interactions of ions, strain and stress due to defects and quantum effects. The lattice usually possesses higher symmetry at high temperature and lower symmetry at lower temperature, but with a few exceptions at special cases. For example, in the cubic phase, the system has the lowest free energy when all atoms are seated at symmetrical sites in the absence of external fields. In this case, the material is a normal dielectric, showing no spontaneous polarization or hysteresis.

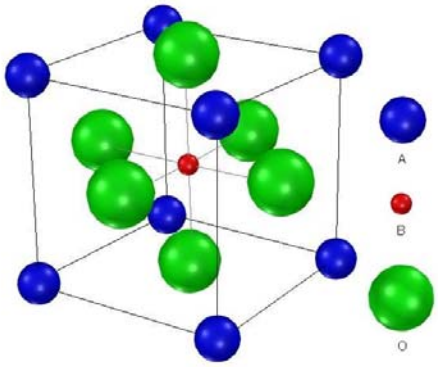

Figure 2 ABO_3 Perovskite structure in the cubic phase.

At temperatures below T_c, the system undergoes a phase transition, and the symmetry of the lattice structure is reduced. Some systems transform from cubic into tetragonal, as shown in Figure 3. In the tetragonal phase, the system usually has two energy minima when the B and O atoms are displaced from their symmetric locations in opposite directions. Because the B sites are cations and O sites are anions, the system will have a net electric dipole moment, which is usually referred to as the spontaneous polarization $\boldsymbol{P_s}$. A material is called ferroelectric if the spontaneous polarization $\boldsymbol{P_s}$ can be reversed by an externally applied electric field.

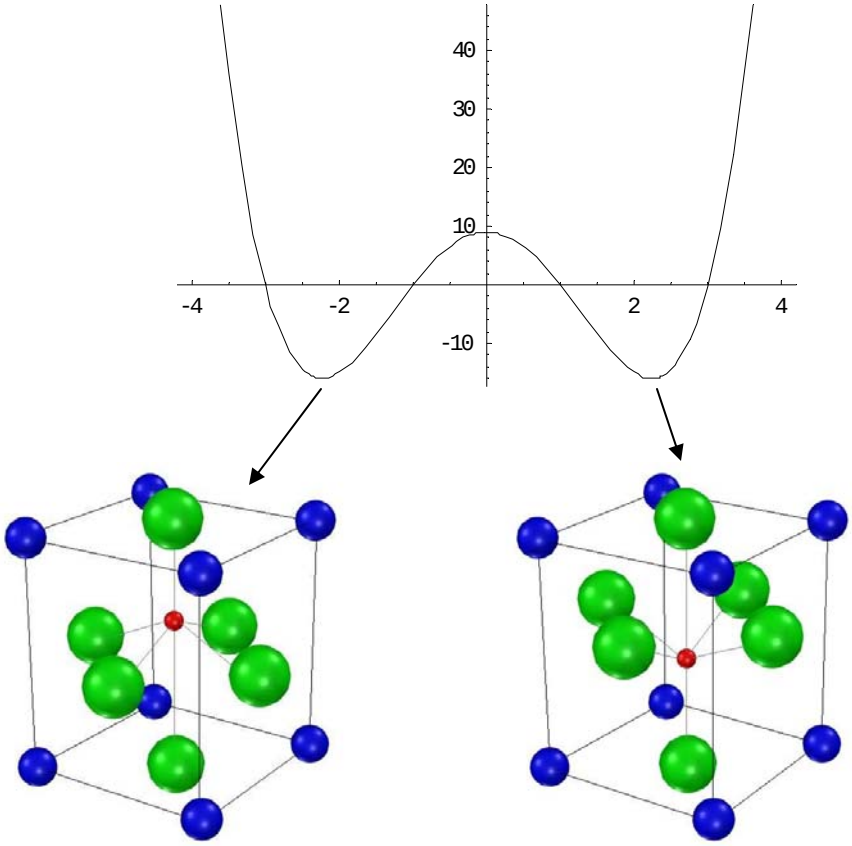

Figure 3 Ferroelectric polarization states of tetragonal lattice structure

A thermodynamic description begins with the Gibbs free energy, defined below:

$$G = U - TS - X_{ij}x_{ij} - D_iE_i \tag{1}$$

Its differential form is given by

$$dG = -SdT - x_{ij}dX_{ij} - D_idE_i \tag{2}$$

where the related physical quantities are entropy S, system temperature T, strain x, stress X, electric displacement D, electric field E.

From Eq. (2), one obtains

$$S = (\frac{\partial G}{\partial T})_{X,E} \quad x_{ij} = (\frac{\partial G}{\partial X_{ij}})_{T,E} \quad D_i = (\frac{\partial G}{\partial E_i})_{T,X} \tag{3}$$

Due to their structural specialty, ferroelectric materials exhibit physical effects useful for various applications. These effects can be expressed as the differential relation between *S, x* and *D*

$$dS = (\frac{\partial S}{\partial T})_{X,E} dT + (\frac{\partial S}{\partial X_{ij}})_{T,E} dX_{ij} + (\frac{\partial S}{\partial E_i})_{X,T} dE_i \quad (4)$$

heat capacity *piezocaloric effect* *electrocaloric effect*

$$dx_{ij} = (\frac{\partial x_{ij}}{\partial T})_{X,E} dT + (\frac{\partial x_{ij}}{\partial X_{kl}})_{T,E} dX_{kl} + (\frac{\partial x_{ij}}{\partial E_k})_{X,E} dE_k \quad (5)$$

thermal expansion *elecstic compliance* *converse piezoelectricity*

$$dD_i = (\frac{\partial D_i}{\partial T})_{X,E} dT + (\frac{\partial D_i}{\partial X_{kl}})_{T,E} dX_{kl} + (\frac{\partial D_i}{\partial E_j})_{X,T} dE_j \quad (6)$$

pyroelectric effect *direct piezoelectricity* *dielectric permittivity*

Among those physical effects defined in Eq.s. (4-6), a few are somehow related to the research work in the following sections.

1.1.1 Curie Temperature

In the absence of external electric field and pressure, Eq. (1) is reduced to

$$G = U - TS \quad (7)$$

At or close to absolute zero teperature, a perovskite crystal stabilizes with structure that the internal energy U is minimized. As pointed out by H.A Jahn and E. Teller in 1937, any nonlinear molecular system in a degenerate electronic will be unstable and will undergo distortion to form a system of lower energy thereby removing the degeneracy[1]. The Jahn-Teller theorem predicted that the distortion should occur for the octahedral crystal field. A lower symmetry structure other than the cubic phase has lower degeneracy in its electron orbits. Hence the electronic energy of system is lower. For this reason, at lower temperature, a pervskite crystal structure generally is not cubic. For example, when $BaTiO_3$ is cooled from room temperature down to -90°C, its crystal structure undergoes a series of transition from more symmetrical cubic phase to less symmetrical rhombohedral phase, with tetragonal, monoclinic phases as intermediate state.

The Jahn-Teller distortion has less effect on crystal structure at higher temperature. A structure with higher symmetry may have a softer or lower frequency phonon spectrum than the

lower symmetry one. As the temperature is increased, the softer phonons will be more highly excited. Since the entropy increases with the level of degeneracy and the occupancy, considering the *TS* term in Eq. (7), above a critical temperature, the system's free energy may be reduced when the structure undergo a transition into a higher symmetry one[2].

The large dielectric constant and spontaneous polarization near phase transition temperature are interpreted with soft optical phonon. The static dielectric constant is related to its phonon mode frequency by the Lyddane-Sachs-Teller (LST) relation[3]

$$\omega_T^2 / \omega_L^2 = \varepsilon(\infty) / \varepsilon(0) \tag{8}$$

ω_T is the frequency of transverse optical phonon at zone center and ω_L is the frequency of longitudinal mode. $\varepsilon(0)$ is the static dielectric constant and $\varepsilon(\infty)$ is the dielectric costant at optical frequency. For soft modes with $\omega_T \rightarrow 0$, we see that $\varepsilon(0) \rightarrow \infty$, the crystal is unstable. In this case the ferroelectric material undergoes a structural phase transition from a high-temperature non-ferroelectric ("paraelectric") phase to a low-temperature ferroelectric phase. This transition occurs at a critical temperature T_c. As the temperature approaches T_c from the high-temperature side, the dielectric constant follows the Curie-Weiss law, $\varepsilon \approx \frac{C}{T - T_0}$, where $T_0 \leq T_c$ is the Curie-Weiss temperature.

The transition can be of first or second order, which is defined in terms of the discontinuity of the partial derivative of the Gibbs free energy (Eq. 1) at T_c. At zero external field, the spontaneous polarization $P^s{}_i = D_i = (\frac{\partial G}{\partial E_i})_{T,X}$, has a discontinuity at T_c for a first-order phase transition (Figure 4a), at which we do not find $\omega_T \rightarrow 0$ or $\varepsilon(0) \rightarrow \infty$. The LST relation suggests that the $\varepsilon(0)$ extrapolate to a singularity at temperature $T_0 < T_c$. In case of a second-order phase transition, P_s is continuous at T_c, while $(\frac{\partial P^s{}_i}{\partial T})_X \Big|_{E=0, T=Tc} = (\frac{\partial G}{\partial T \partial E_i})_X$ has discontinuity (Figure 4b). In this case, $T_c = T_0$.

There is another class of ferroelectric materials which exhibits a diffuse phase transition with a broadened maximum in the dielectric permittivity, as well as strong frequency dispersion in the permittivity (Figure 4c). Chemical and structural heterogeneity is believed to contribute to relaxor behavior. Relaxor ferroelectrics are interesting candidate for frequency-agile microwave

elctronics (FAME). One of the ferroelectric thin films we have investigated ($SrTiO_3/DyScO_3$) exhibits relaxor behavior.

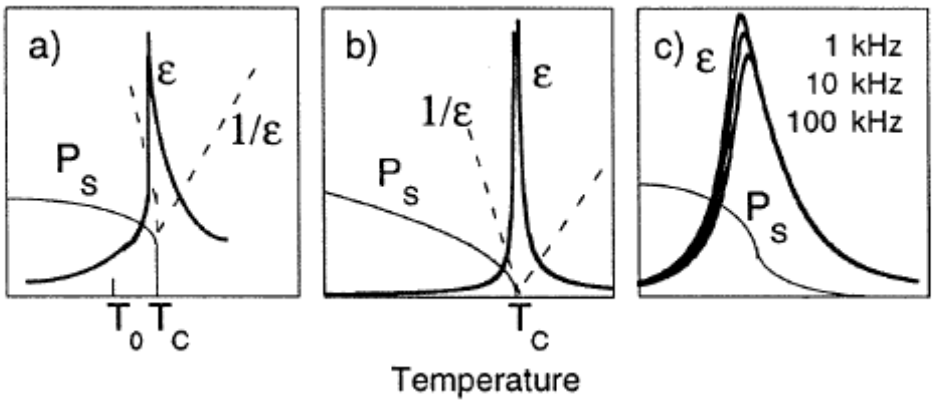

Figure 4 Dielectric behavior of first-order, second-order and relaxor like transition.

1.1.2 Piezoelectricity

Ferroelectric materials also possess piezoelectricity – when a stress is applied, a ferroelectric material develops an electric moment proportional to the magnitude of the stress. The stress is expressed as a second-rank tensor σ_{ij}, and the electric polarization is represented by a vector quantity ***P***. To describe piezoelectricity as a physical property that relates the electric polarization and stress requires a third-rank tensor. In general, their relation is in the form:

$$P_i = d_{ijk}\sigma_{jk} \tag{9}$$

The converse piezoelectric effect also exists. When an electric field is applied, the dimensions of the piezoelectric material will change slightly, corresponding to strain created in the material.

$$x_{ij} = d^t_{ijk}E_k \tag{10}$$

Here d^t_{ijk} is called the converse piezoelectric tensor. Indeed, based on thermodynamic theory, it can be demonstrated[4] that $d^t_{kij} = d_{ijk}$.

The piezoelectric properties of ferroelectrics are widely used in transducer, ultrasonic detectors, sonar, accelerometers and piezo igniters. The converse piezoelectric properties are used for position actuators and for ultrasound generation. Nanopositioning stages are often made

from piezoelectric stacks, and with them one can achieve sub-atomic accuracy. Converse piezoelectricity is also used to determine crystallographic orientation. Piezoforce microscopy (PFM) uses the converse piezoelectric effect to image thin-film ferroelectric nanometer structures.

1.1.3 Pyroelectricity

Pyroelectricity is the property of a special group of crystals such that upon temperature changes electric dipole moment increases or decrease along one of the crystal axis and therefore net electric charges accumulate at corresponding surfaces by charge migration within the crystal or external loop, as indicated in Figure 5. The pyroelectric coefficient is defined as $\mathbf{p} = (\partial \mathbf{P}_s / \partial \theta)_{T,E}$. $\mathbf{P}_s$ is the spontaneous polarization. θ is temperature. The constraints are constant stress *T* and electric field *E*. Though this property will not be covered by this research, pyroelectricity cannot be neglected. It represents a group of materials possess relatively large and useful interaction coefficients between thermal, mechanical, electrical, and optical properties. Pyroelectric materials are solely determined by their crystal structure. Among 32 point group crystals, 10 polar groups are pyroelectrics. They are called polar because they show spontaneous polarization at certain temperature range in the absence of external electric field. These ten groups[4] are 1, m, 2,mm2, 3, 3m, 4, 4mm, 6 and 6mm. However, only those polar crystals whose polarization can be switched by external electric field are called ferroelectric materials. Indeed, ferroelectric are a sub-group of pyroelectric material and is called ferroelectric pyroelectrics. They usually carry larger pyroelectric coefficients compared to non-ferroelectric pyroelectrics[5]. Pyroelectric phenomena have been known for 24 centuries. People noticed that some minerals had the properties to attract small objects. Now we know clearly that it is due to the electrostatic charge created by temperature changes on pyroelectrics. But it was not attributed to electricity at that time until two millennia later in 1717 by physician and chemist Louis Lemery. The term pyroelectric was introduced in 1824 by David Brewster (well known by a series of important works in optics, including the "Brewster Angle" named after him) and ferroelectricity was discovered a century later in 1920 by Joseph Valasek. Pyroelectrics has found its application in infrared detectors; the charge it creates on surface is so high that recently it even found application in nuclear fusion experiments[6,7].

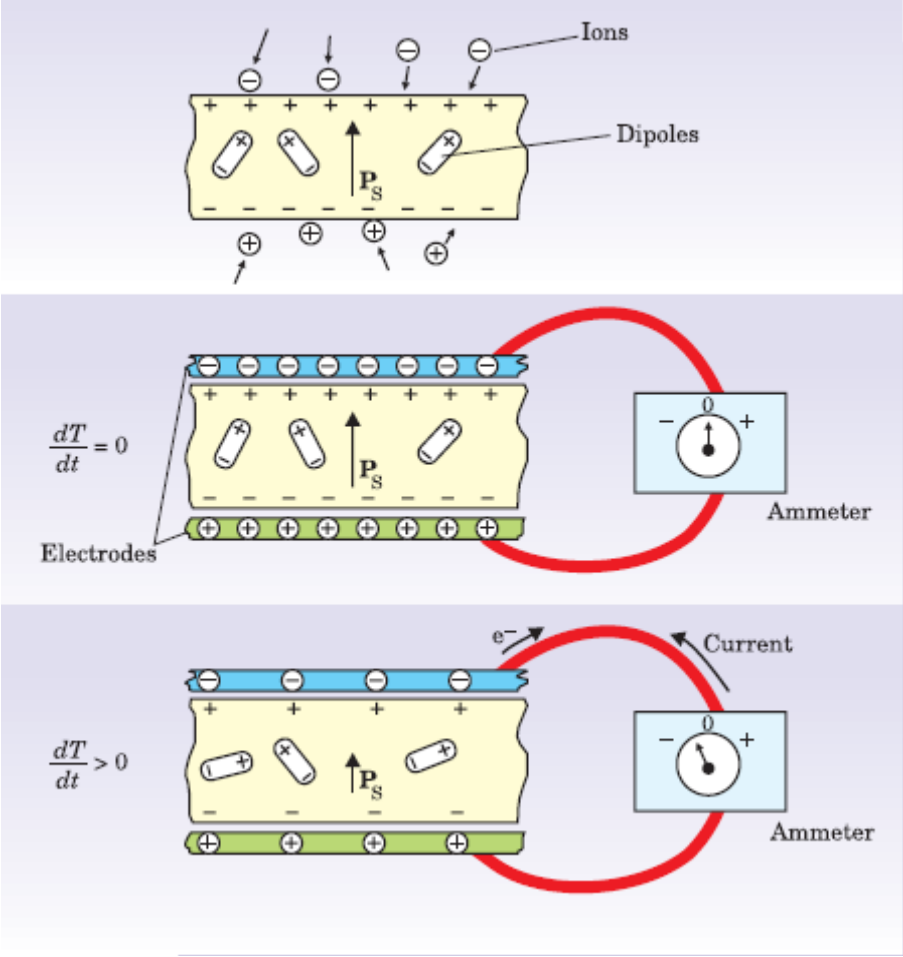

Figure 5 If a pyroelectric crystal with an intrinsic dipole moment (top) is fashioned into a circuit with electrodes attached on each surface (middle), an increase in temperature T prompts the spontaneous polarization P_S to decrease as the dipole moments, on average, diminish in magnitude. The horizontal tilting of the dipoles, pictured at bottom, signifies the effect. A current flows to compensate for the change in bound charge that accumulates on the crystal edges. (Adapted from ref 8)**.**

1.1.4 Barkhausen pulses

Barkhausen noise, an effect first associated with ferromagnetism, was discovered by Heinrich Georg Barkhausen[9] in 1919. When a ferromagnet is magnetized or demagnetized with a smoothly changing external field, the magnetization does not always increase or decrease continuously. Instead, there appear to have some random steps or jumps. Barkhausen noise demonstrated the existence of ferromagnetic domains. The induced magnetic dipole orientation

change affects the whole domain instead of individual atoms. Similar phenomena exist in ferroelectrics. Ferroelectric Barkhausen noise in the switching current was observed when voltages were applied to some ferroelectric crystals[10,11,12]. In Chapter 3, Barkhausen noise, along with lattice-scale domain motion, is observed using contact-mode AFM.

1.1.5 Birefringence and Electro-optic effect

Ferroelectrics have anisotropic crystal structures. Its refractive index varies for different light polarizations at a given wavelength – a property called birefringence. To give a clear description of the optical properties of ferroelectrics, one can start with the equation for electromagnetic wave propagation in dielectric media, which is based on Maxwell equations:

$$\mathbf{k}\times(\mathbf{k}\times\mathbf{E})+\mu_0\boldsymbol{\varepsilon}\omega^2\mathbf{E}=0 \tag{11}$$

Here the dielectric constant $\boldsymbol{\varepsilon}$ is a symmetric second-rank tensor, and $\mathbf{k}$ is the wave vector. The dielectric constant in general depends on ω, the angular frequency of light wave, i.e., $\varepsilon=\varepsilon(\omega)$. We will assume the magnetic permeability to be 1 , i.e., $\mu=\mu_0$, which is a good approximation for most ferroelectrics. We can express ε explicitly in matrix form:

$$\varepsilon=\begin{pmatrix}\varepsilon_{11} & \varepsilon_{12} & \varepsilon_{13}\\ \varepsilon_{21} & \varepsilon_{22} & \varepsilon_{23}\\ \varepsilon_{31} & \varepsilon_{32} & \varepsilon_{33}\end{pmatrix} \tag{12}$$

The values of ε_{ij} is constrained by symmetry rules such that

$$\varepsilon_{ij}=\varepsilon_{ji} \tag{13}$$

Because ε_{ij} is a real symmetric matrix, it can be made diagonal in an appropriately rotated coordinate system. Along the principal axes, we have

$$\varepsilon=\begin{pmatrix}\varepsilon_x & 0 & 0\\ 0 & \varepsilon_y & 0\\ 0 & 0 & \varepsilon_z\end{pmatrix}=\begin{pmatrix}n_x^2 & 0 & 0\\ 0 & n_y^2 & 0\\ 0 & 0 & n_z^2\end{pmatrix} \tag{14}$$

In Eq. (11), the dielectric impermeability is usually used in place of the second range dielectric constanct tensor, which has the matrix form:

$$\eta_{ij} = \varepsilon_{ij}^{-1} = (\frac{1}{n^2})_{ij} = \begin{pmatrix} \eta_{11} & \eta_{12} & \eta_{13} \\ \eta_{21} & \eta_{22} & \eta_{23} \\ \eta_{31} & \eta_{32} & \eta_{33} \end{pmatrix} \tag{15}$$

It is defined by the equation

$$\eta\varepsilon = \varepsilon_0, \quad \text{where } \eta_{ij} = \eta_{ji} \ . \tag{16}$$

From the Fresnel formulas, the fraction of light reflected at the air-ferroelectric interface at normal incidence is given by $r = (n\text{-}1)^2/(n+1)^2$. When imaged with polarized light, ferroelectric domains with principal axes oriented along different directions will appear bright under transmission. Figure 6 shows a 90˚ degree domain in a bulk $BaTiO_3$ crystal[13].

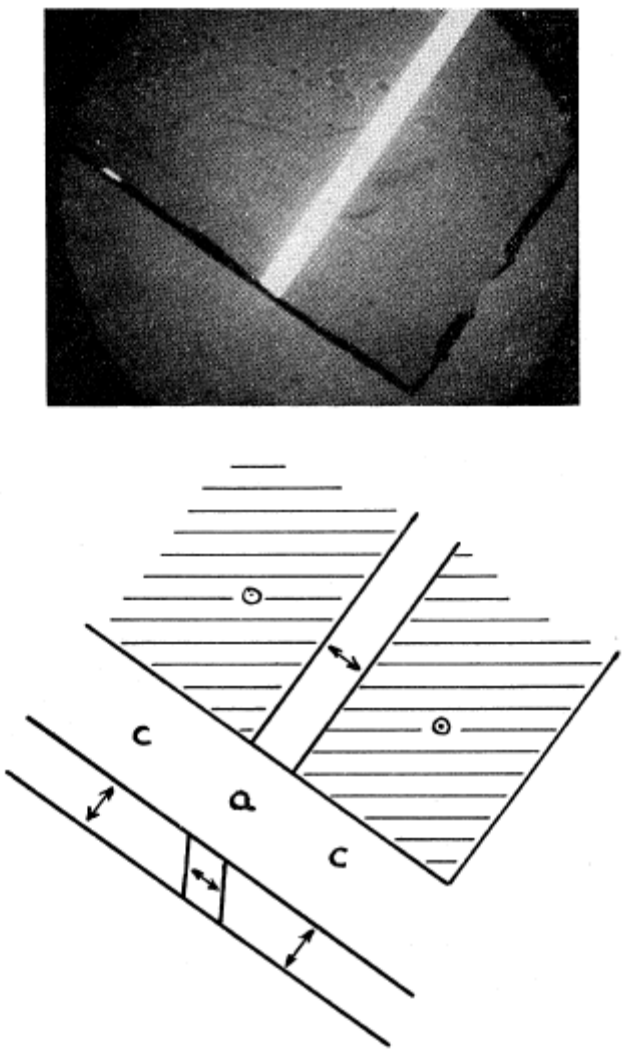

Figure 6 90° domain walls (45° lines) in a bulk $BaTiO_3$ crystal. In the diagram, c labels c domains (optical axis out of crystal surface) and a labels a domains (optical axis in-plane) as indicated by arrows. From Ref. [14]

Usually, polarization measurement is sufficient to tell the difference between 90° domains. But because of the symmetry between 180˚ domains, direct polarization measurements are unable to discriminate them. To investigate 180˚ domain walls, commonly a DC electric field is applied to crystal to break this symmetry. Under an applied electric field, ferroelectric domains of various orientations undergo refractive index changes at different levels, a phenomenon called electro-optical effect.

In certain types of crystals, including ferroelectrics, the application of an electric field will change the refractive index. This is generally known as an electro-optic effect and is traditionally defined in terms of the change in the impermeability tensor

$$\Delta\eta_{ij} = \Delta(\frac{1}{n^2})_{ij} = r_{ijk}E_k + s_{ijkm}E_kE_m \tag{17}$$

where r_{ijk} is the linear electro-optical tensor (third rank) and s_{ijkm} is the quadratic electro-optic tensor (fourth rank). The non-zero components of linear and quadratic electro-optic are strongly constrained by the crystal symmetry. In the case of $r_{ijk,}$ symmetry considerations requires that[4,15]

$$r_{ijk} = r_{jik} \tag{18}$$

Therefore the number of independent components in the r_{ijk} tensor is reduced to 18. Instead of using all 3 indices *i,j,k* to label those component, they are contracted using the following convention:

$$\begin{pmatrix} r_{11k} & r_{12k} & r_{13k} \\ r_{21k} & r_{22k} & r_{23k} \\ r_{31k} & r_{32k} & r_{33k} \end{pmatrix} \rightarrow \begin{pmatrix} r_{1k} & r_{6k} & r_{5k} \\ r_{6k} & r_{2k} & r_{4k} \\ r_{5k} & r_{4k} & r_{3k} \end{pmatrix} \tag{19}$$

And r_{ijk} is usually written in a 6×3 matrix form

$$r_{ijk} = \begin{pmatrix} r_{11} & r_{12} & r_{13} \\ r_{21} & r_{22} & r_{23} \\ r_{31} & r_{32} & r_{33} \\ r_{41} & r_{42} & r_{43} \\ r_{51} & r_{52} & r_{53} \\ r_{61} & r_{62} & r_{63} \end{pmatrix} \tag{20}$$

The story is not finished here regarding the crystal symmetry issues. We know that the electro-optic tensor as a physical quantity obeys the coordinate transformation law. The transformation of coordinate means a change from one set of mutually orthogonal axes (x_1, x_2, x_3) to another with the same origin (x'_1, x'_2, x'_3). The change can include rotation, mirroring, or inversion.

$$\begin{pmatrix} x_1' \\ x_2' \\ x_3' \end{pmatrix} = \begin{pmatrix} a_{11} & a_{12} & a_{13} \\ a_{21} & a_{22} & a_{23} \\ a_{31} & a_{32} & a_{33} \end{pmatrix} \bullet \begin{pmatrix} x_1 \\ x_2 \\ x_3 \end{pmatrix} \tag{21}$$

Under this transformation each index will be affected,

$$r_{ijk}' = a_{il}a_{jm}a_{kn}r_{lmn} \tag{22}$$

Consider the orthorhombic structure mm2 group as an example (as will be used for electro-optic effect calculation in Chapter 4). This point group has two mirror planes (*xz* and *yz*) and one 2-fold rotation axis (*z*). A mirror operation about the *xz* plane is described by the following transformation matrix:

$$\begin{pmatrix} 1 & 0 & 0 \\ 0 & -1 & 0 \\ 0 & 0 & 1 \end{pmatrix}$$

This transformation produces the following constraints on the electro-optic tensor:

$$r_{63}' = r_{123}' = r_{213}' = a_{11}a_{22}a_{33}r_{123} = -r_{123} = -r_{213} = -r_{63} \tag{23}$$

We know under the symmetry transformation, all physical quantities remain unchanged, so $r_{63}' = r_{63}$. Therefore $r_{63} = -r_{63}$ and $r_{63} = 0$. Following the same procedure to do all the symmetry transformation, one obtains that:

$r_{12} = r_{22} = r_{32} = r_{41} = r_{43} = r_{52} = r_{61} = r_{63} = 0$, due to the symmetry operation about the *xz* plane. $r_{11} = r_{21} = r_{31} = r_{41} = r_{52} = r_{53} = r_{62} = r_{63} = 0$, due to the symmetry operation about the y*z* plane. $r_{11} = r_{12} = r_{21} = r_{22} = r_{31} = r_{32} = r_{43} = r_{53} = r_{61} = r_{62} = 0$, due to 2-fold rotation symmetry effect about the z axis.

Only r_{13}, r_{23}, r_{33}, r_{42}, and r_{51} can be non-zero. So the electro-optic coefficient for orthorhombic crystal structure with mm2 symmetry has the following form:

$$r_{ijk} = \begin{pmatrix} 0 & 0 & r_{13} \\ 0 & 0 & r_{23} \\ 0 & 0 & r_{33} \\ 0 & r_{42} & 0 \\ r_{51} & 0 & 0 \\ 0 & 0 & 0 \end{pmatrix} \tag{24}$$

In Figure 7, a $BaTiO_3$ bulk crystal is observed with electric field applied normal to the paper plane (the plane of observation). Both DC and AC field are applied. Polarized strobe light synchronized to an applied AC voltage shows the contrast between 180° domains.

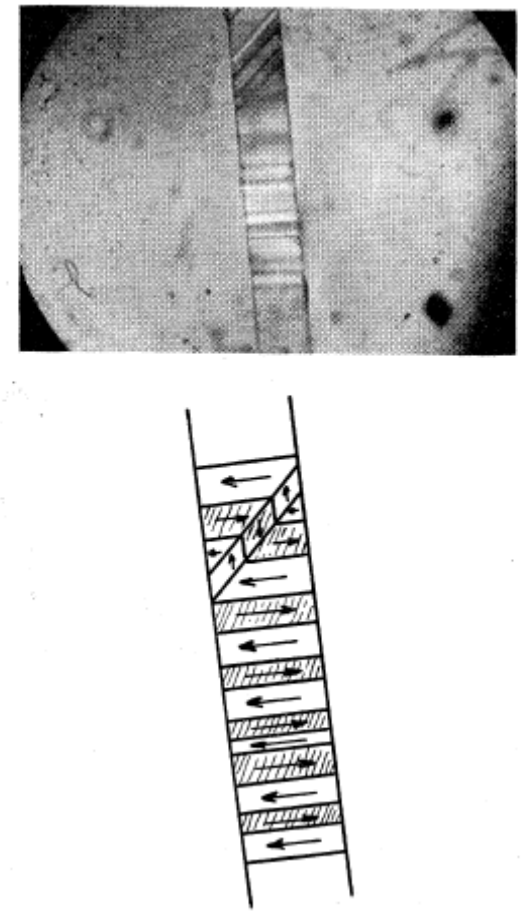

Figure 7 Voltage applied normal to the plane of paper. The electric field induces rotation of principal axis of each domain. 180° domains rotates reversely such that they are not always symmetric to all light polarization orientation

1.2 THIN FILM FERROELECTRICS

Research on thin film ferroelectric has made substantial progress thanks to novel nano fabrication techniques[16]. The thickness of thin film ferroelectrics are usually below 1 micrometer. The voltage required to perform either polarization reversal or dielectric constant tuning is small. This advantage makes it a good candidate for modern electronics which require low power consumption and small size. Its piezoelectricity is commonly used in microelectromechanical system (MEMS), such as ultrasonic micromotors and deformable mirrors. Its pyroelectricity has been used for infrared detectors. The remnant polarization is

used for the next generation of high density nonvolatile memories, FeRAM. The high tuning factor is employed for frequency agile materials for electronics and can be used in microwave electronics such like phased array antennas. Thin film ferroelectrics have properties that can vary significantly from their bulk counterparts due to effects from strain, interface, substrate, and electrodes. For example, the lattice mismatch and differential thermal coefficient of expansion between substrate and film causes strain in the material, breaks the symmetry and changes the phase transition temperature.

Similar to ferromagnetic materials, ferroelectrics generally exhibit complex domain structures. The equilibrium domain structure depends on a delicate balance of electromagnetic strain and thermal energies. It is the origin of some of the macroscopic properties such as domain creep, Barkhausen noise, fatigue, relaxor behavior, dielectric tuning, etc.

A number of microscopic methods have been developed to observe static domain structures, including Piezoforce Microscopy, Electro-optic Microscopy, and Near-field scanning optical microscopy. These methods vary in sensitivity and resolution, and their utility depends on the questions being asked. The optical birefringence measurements can discern 90° domain walls. The Piezo Force Microscopy (PFM) is a powerful tool for visualizing domain structures through their piezoelectric response, with high resolution down to 10 nm[17,18,19]. In addition to high spatial resolution, we also need the technique to resolve domain dynamics with picosecond time resolution in order to probe microwave-frequency domain dynamics. The technique described in this thesis uses an ultrafast laser, which has an ultimate temporal resolution of ~100 fs.

.

1.3 STRAIN ENGINEERING

The origin of macroscopic strain is the lattice mismatch between the film and substrate. The defect in the film will also generate strain and contribute to inhomogeneous properties. Strain has a strong impact on the lattice structure and ferroelectric phase-transition temperature[20,21,22], as shown in Figure 8, as well as related dielectric, piezoelectric and electrooptic properties. The strain effect is largest for coherent films before relaxation occurs[23]. The critical coherent thickness is ~2-4 nm. Above that value, the strain in the film start to relax and lattice misfit dislocations start to appear until it relaxes to bulk lattice constant. Recent film growth techniques can extend this range by 2 or 3 times but it is still too thin for industrial applications (120 nm)

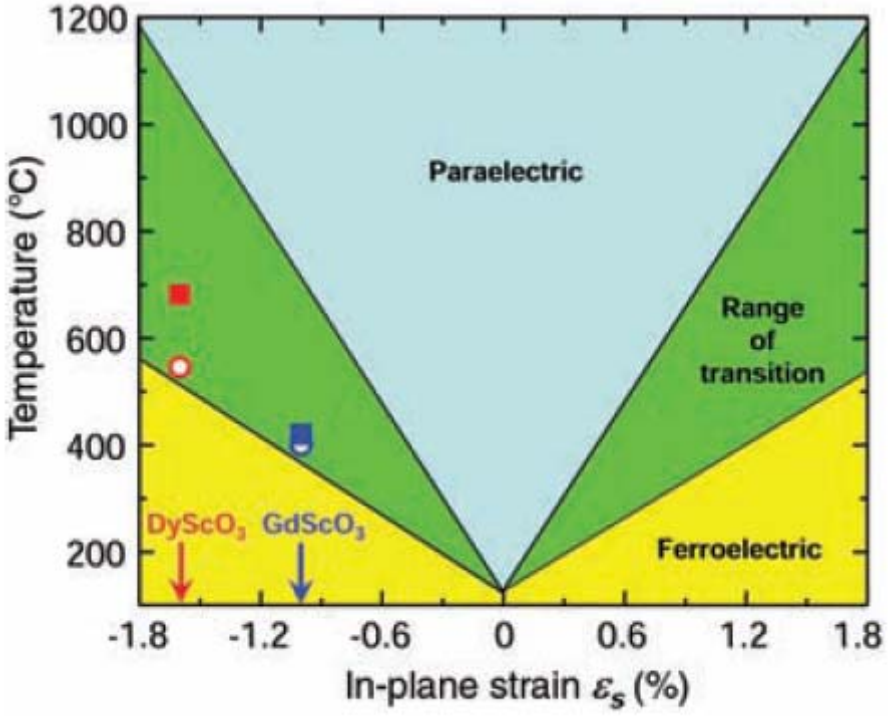

Figure 8 Expected phase transition temperature of (001) $BaTiO_3$ under biaxial in-plane strain. $\varepsilon_s = (a^{\parallel} - a_0)/a_0$, where $a^{\parallel}$ is the inplane lattice parameter of a biaxially strained (001) $BaTiO_3$ film and a_0 is the lattice parameter of free standing cubic $BaTiO_3$. Positive values represent tensile strain and negative values represent compressive strain. (Adapted from Ref .[24])

Because of the strain effect, ferroelectric thin films possess properties not available to bulk. One way of performing strain engineering is to carefully choose the substrates or surfaces whose lattice constant closely (but not perfectly) matches that of the film. $BaTiO_3$ thin films epitaxially grown on $GdScO_3$ and $DyScO_3$ by MBE are biaxial compressed and show phase transition temperature close to 500°C and remnant polarization 250% higher than bulk material[24] (Figure 8). This makes it a good candidate for lead-free non-volatile memory and electro-optic devices. Bulk $SrTiO_3$ remains paraelectric down to 0 K due to quantum fluctuation[25]. Recently $SrTiO_3$ grown on $DyScO_3$ by oxide molecular beam epitaxy (oxide-MBE) (Figure 9) method shows room-temperature ferroelectricity, high dielectric permeability (Figure 12) at microwave frequencies and a sharp field dependence[26]. These properties are very useful for field tunable devices.

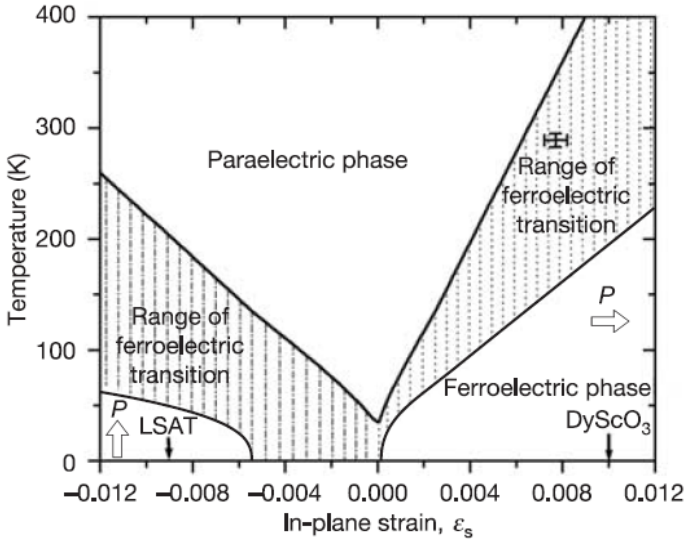

Figure 9 Expected shift of Tc of (100) $SrTiO_3$ with biaxial in-plane strain, based on thermodynamic analysis. The arrows indicate the predicted direction of the polarizaiotn for strained $SrTiO_3$; in-pane for biaxial tensile strain and out-of-plane for biaxial compressive strain.

Another way of to control strain is through annealing[27]. After epitaxial growth of film, an annealing procedure at various temperatures and with various oxygen pressures can be added to adjust the oxygen vacancy density to the film. This will effectively change lattice constants. Both in-plane and our-of-plane lattice constant can be varied in this way. Therefore the tetragonality varies(Figure 10). A high film figure of merit (roughly the fractional change in

dielectic constant at a fixed electric field, divided by the quality factor of a resonant circuit involving the ferroelectric tuning capacitor) can be achieved[28].

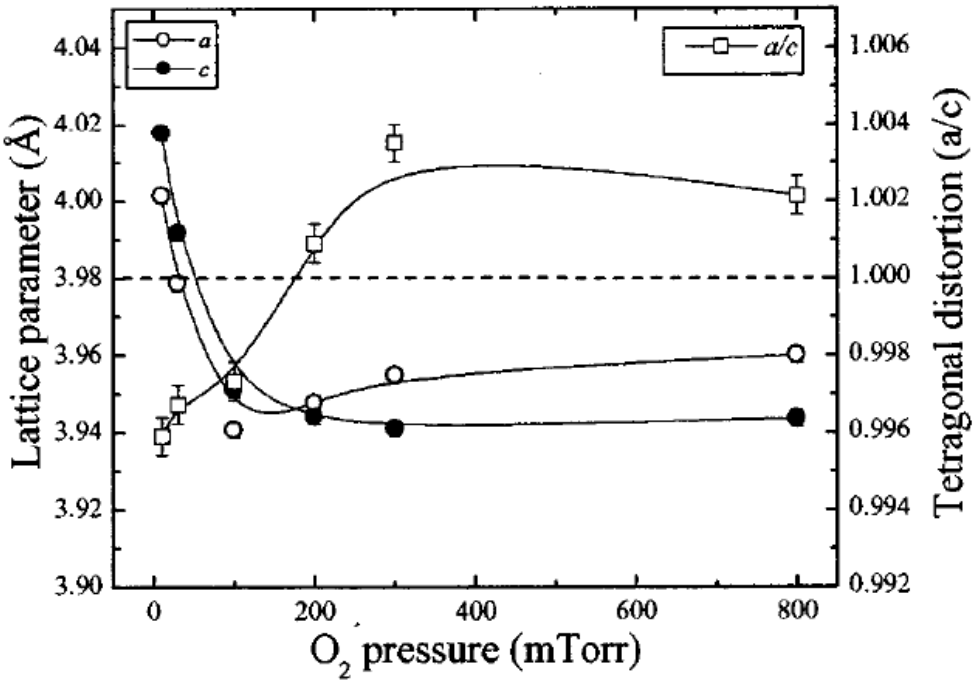

Figure 10 Oxygen deposition pressure dependent measured lattice parameters along in-plane (a) and surface normal (c) direction of epitaxial $Ba_{0.4}Sr_{0.6}TiO_3$ films on MaO single crystals, and calculated tetragonal distortion (*D=a/c*). (Adapted from ref. [28])

At some cases the lattice mismatch is not favorable. A buffer layer can be added between substrate and film[27]. For example, ferroelectric $BaTiO_3$ grown on silicon substrates would be very interesting for non-volatile memory devices. However, when it is grown on silicon substrate, the lattice mismatch is too large; relaxation of the film, combined with differential thermal contraction upon cooling, results in in-plane polarization. A $(BaSr)TiO_3$ buffer layer can be added to match the lattice constant to create an out-of plane polarization [29,30]

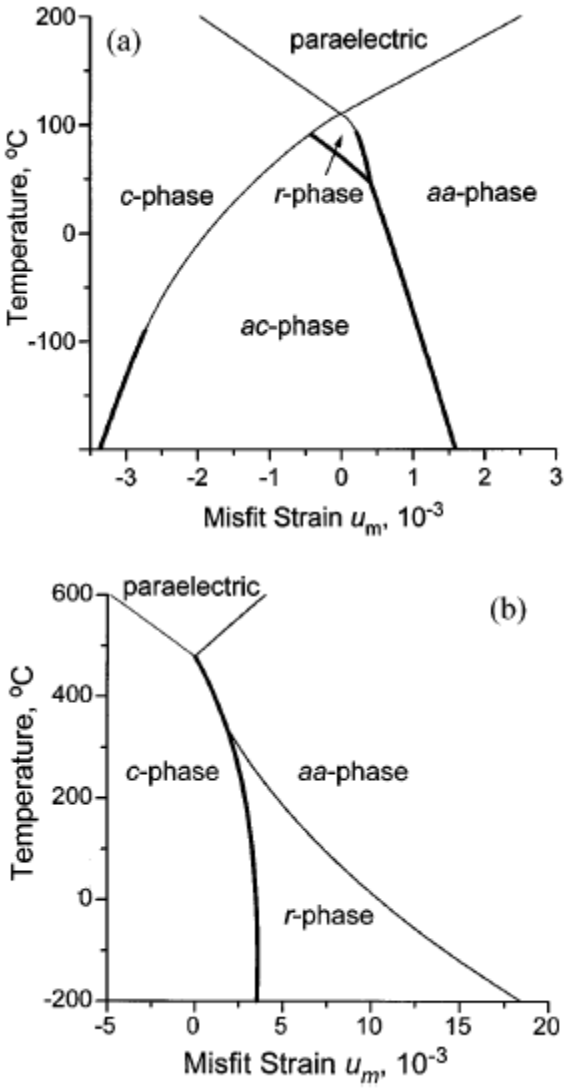

Figure 11 Phase diagrams of (001) single-domain $BaTiO_3$ (a) and $PbTiO_3$ (b) thin films epitaxially grown on different cubic substrates providing various misfit strains um in the heterostructures. Adapted from Ref. [21].

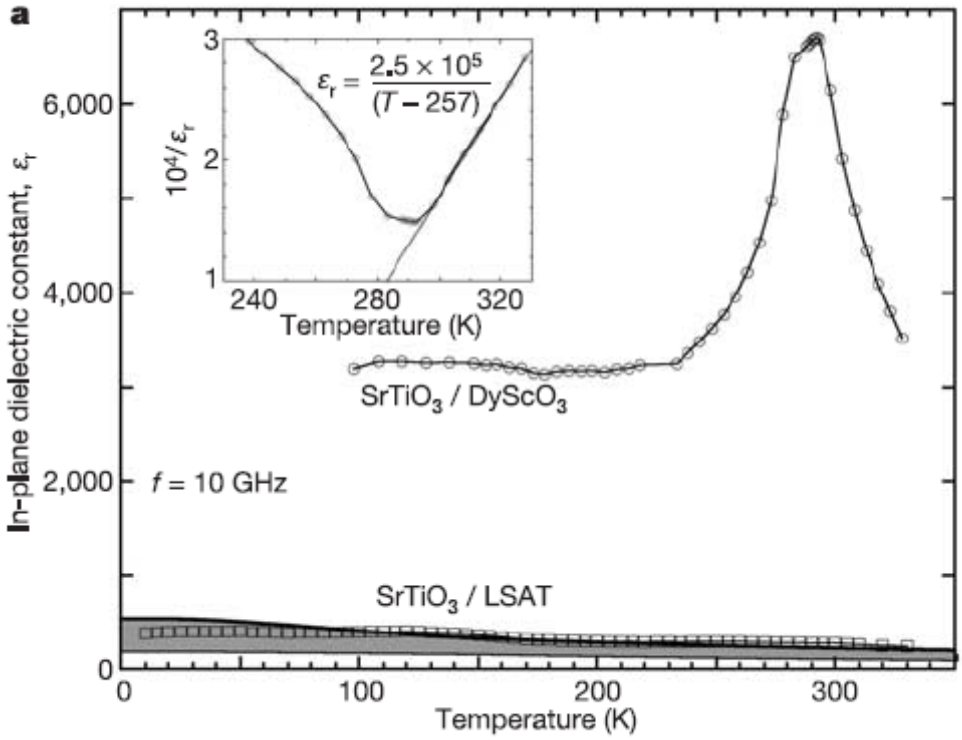

Figure 12 In-plane dielectric constant (ε_r) in strained epitaxial $SrTiO_3$ films as a function of temperatue at a measurement frequency f=10 GHz. $SrTiO_3$/$DyScO_3$ is under biaxial tensile strain and $SrTiO_3$/LSAT is under biaxial compressive strain. The peak in ε_r of about 7,000 indicate the T_c of $SrTiO_3$ under 0.8% lattice mismatch is about 293 K. Adapted from Ref [26].

2.0 INSTRUMENTATION AND FERROELECTRIC MEASURMENTS

The experiments that were conducted for this thesis were performed in large part using instrumentation that was home-designed and built. Apertureless Near-Field Scanning Optical Microscopy (ANSOM) is a relatively new technique that provides sub-wavelength spatial resolution and can be combined with femtosecond optical sources to achieve high spatial and temporal resolution for domain dynamics in ferroelectrics. Our system is composed of a home-built inverted atomic force microscope and confocal scanning optical microscope. The working principle of our systems is explained in this chapter.

2.1 ATOMIC FORCE MICROSCOPY (AFM)

Atomic Force Microscopy[31] (AFM) is now a common technique and a standard for high resolution surface characterization[32] [33]and nano-manipulation. A sharp tip works like a record needle stylus to produce a height map of the surface of interests. A feedback loop controls the tip-surface separation at a constant value, usually a few nanometers or a few angstroms. AFM was invented after Scanning Tunneling Microscope (STM) which uses a metallic tip and relies on quantum mechanical tunneling of electrons from tip to the conductive surface, usually in vacuum. By contrast, AFM can work in the air and even in liquids; proper choice of tip material and tip shape greatly enhance the amount of signal one obtains from an experiment.

In our experiment we have two different kinds of AFM probes: Cantilever-based probes (Figure 14) and tuning fork-probes (Figure 16, Figure 17). Cantilevers are usually made of silicon or silicon nitrite (Figure 15), and the sharp ends have a typical radius of curvature below 20 nm. The back of the cantilever is coated with a high quality reflective metal, such as aluminum, gold or platinum. Light from a diode laser is focused onto the back of the cantilever

and reflected light is detected by a segmented photodiode. The mechanical motion of the cantilever is detected by measuring the laser spot displacement on the diode. The sample is brought close to the tip, and raster scanned in the x,y direction perpendicular to tip axis. The separation between AFM tip and sample surface is controlled with a piezo-driven XYZ stage and PID feedback loop. The motion of the cantilever is detected as the displacement of laser spot on the segmental quadruple photo detectors. The displacement is converted into electric signal and used as PID process variable. There are collective interactions between sample surface and tip end, including van der Waals (vdW) force, chemical force, image force, capacitance force and static electric force due to tip and surface charging[34]. For ferroelectric samples, the vdW force, and capacitance force are relevant. The vdW force is an attractive interaction of fluctuating dipoles in the atoms of the tip and surface. The interaction potential of two point dipole takes the form[35]

$$V(r) = -\frac{C}{r^6}, \quad F(r) = -C\frac{6}{r^7}$$

The actual geometry of tip and surface affects this expression. For a conical or pyramid shaped tip, the vdW interaction between tip and a flat surface is [36]

$$V(r) = C\ln(r), \quad F(r) = -C\frac{1}{r}$$

When the tip-sample separation becomes comparable to interatomic distances, the vdW force between the front atom at the very end of tip and sample atom closest to it will dominate and the chemical bonding can also occur. The short distance potential takes the form[36]

$$V(r) = -C_2[2(\frac{a}{r})^6 - (\frac{a}{r})^7]$$

Combining the above two equations, the tip-sample interaction potential is schematically plotted versus separation in Figure 13.

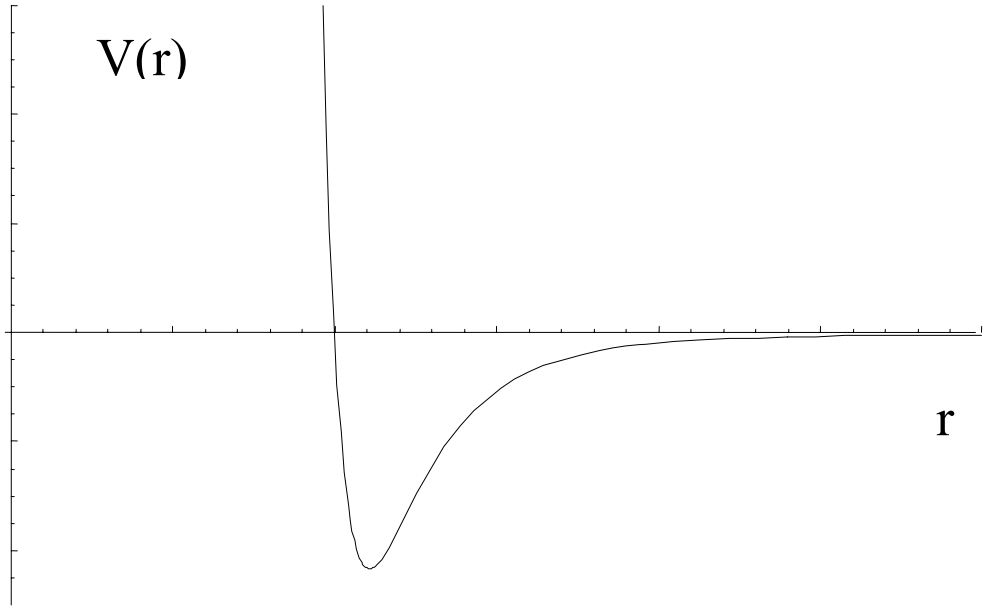

Figure 13 Potential V(r) plotted as a function of the tip-surface separation r.

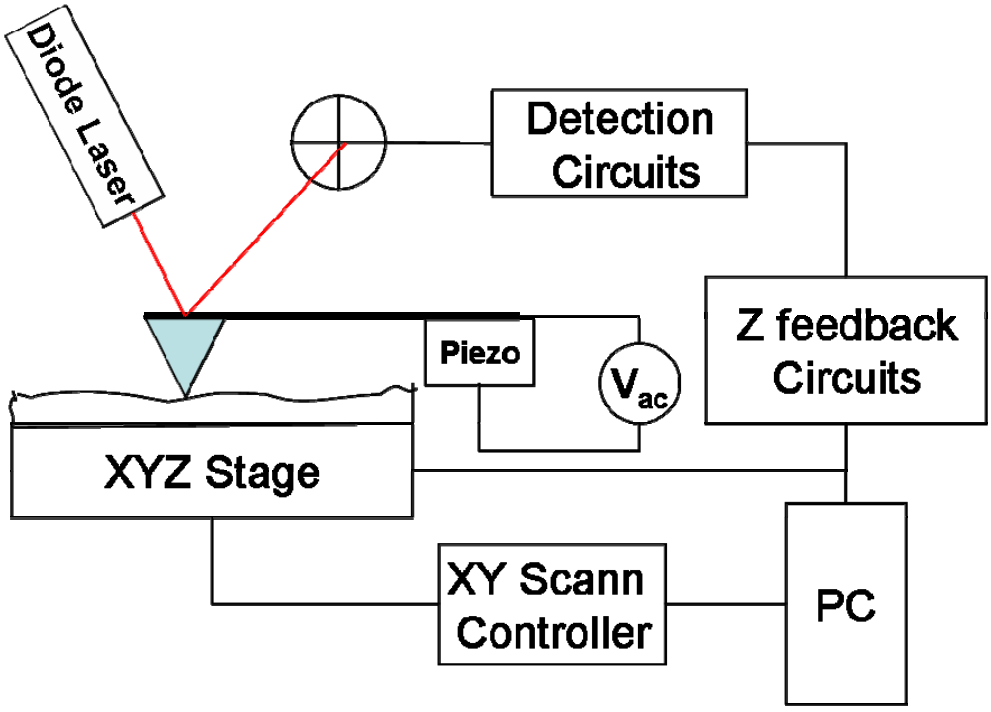

Figure 14 Cantilever Based AFM

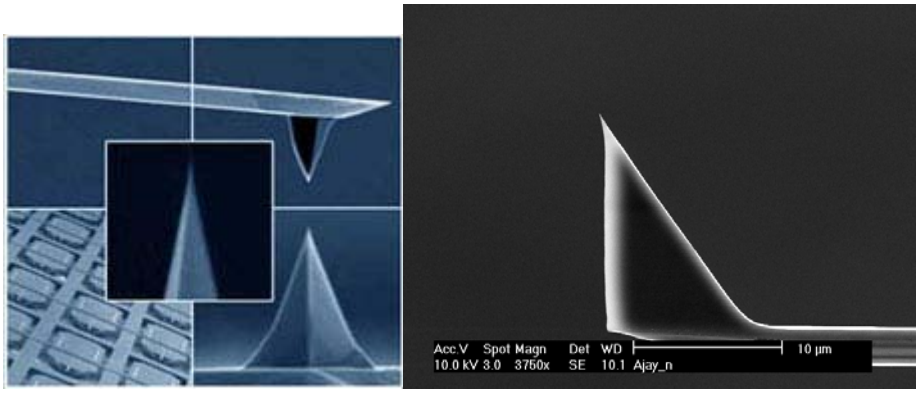

Figure 15 AFM Cantilever and tips (from NanoScience Instruments website).

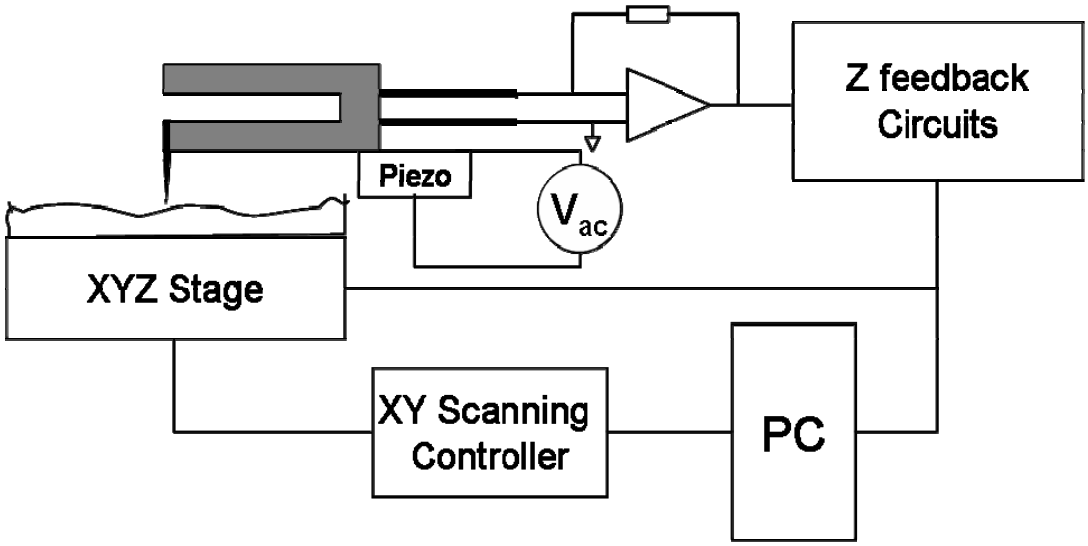

Figure 16 Tuning fork based Atomic Force Microscope.

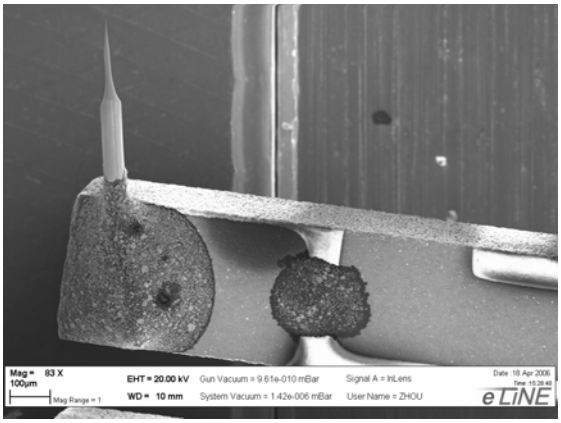

Figure 17 Quartz tuning fork with tungsten tip bonded.

Our AFM (Figure 18) works in contact mode, Non-contact mode (intermittent contact) or non-contact mode.

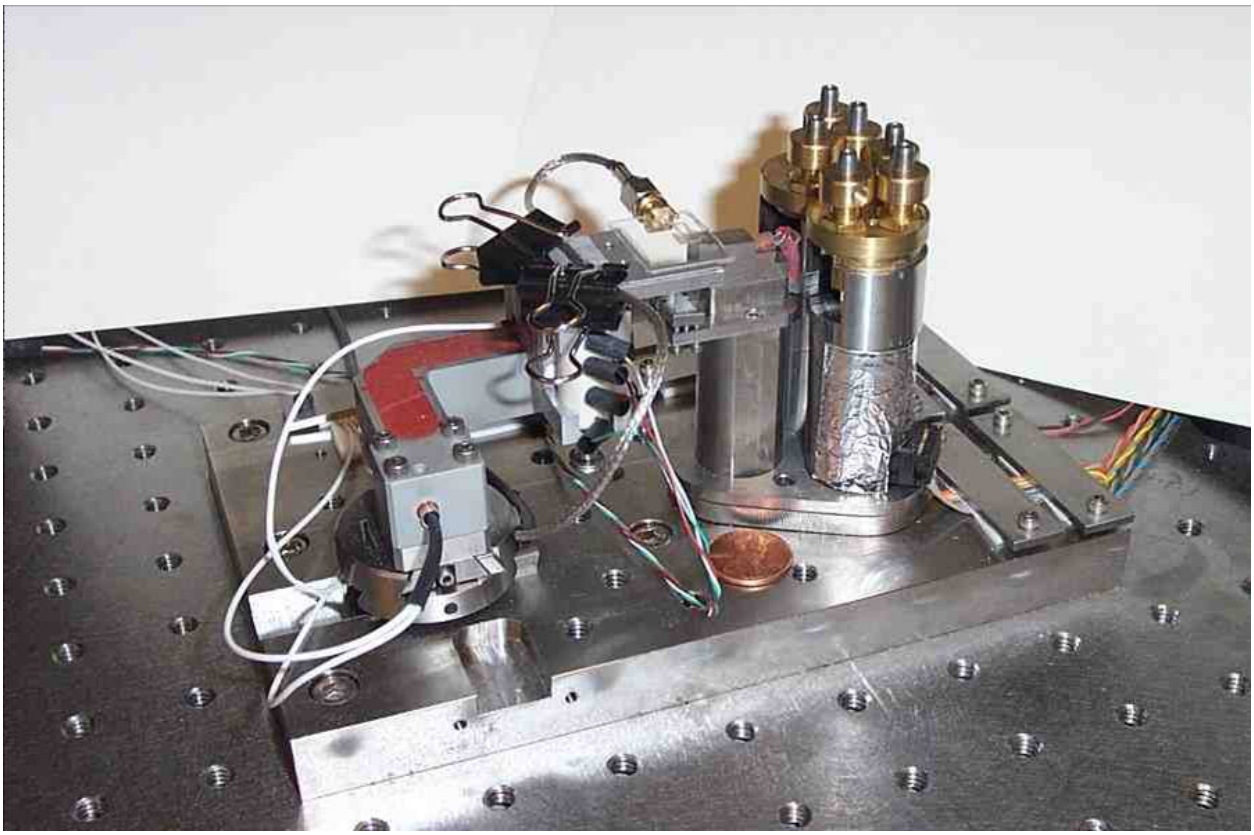

Figure 18 Home built atomic force microscope. The tip is inverted to scan from the sample bottom for convenient arrangement of optics.

Before explaining these different modes, we have to keep in mind that on the material surface there is always absorbed water or gas layers in the ambient condition, even when the relative humidity is close to 0%[37]. The thickness is usually below 1 nm, but thick enough to affect the AFM tip behavior and scan results.

Contact Mode

In contact mode, the AFM tip is brought closest to the surface and penetrates the absorbed liquid layer. The short-range interatomic interaction dominates the force applied to the tip by the sample surface. Atomic and even sub-atomic resolution can be resolved in this mode[33] [32]. The cantilevers working in this mode are soft (typical material is Si_3N_4), with a relatively small effective spring constant 0.1-1 N/m to avoid damage to the sample surface and/or the tip

itself. The feedback loop keeps track of the cantilever beam deflection angle and controls the sample stage height to keep it constant.

Non-contact mode

In non-contact mode, the cantilevers' spring constants are usually one order of magnitude larger than in contact mode. A small piezoelectric transducer is placed near the cantilever and drives it at the cantilever's resonant frequency, using a fixed driving amplitude. As the tip is brought close to the sample surface, the tip will interact with the surface and then retract. Under suitable conditions it is possible for the tip to penetrate the liquid layer. The capillary force of the liquid can capture the tip if the amplitude is below the range 20-100 nm. When the tip interacts with the surface, the damping between the tip and surface shifts the resonant frequency, causing the amplitude of resonance to decrease; when the tip is far apart from surface, the tip has more room to oscillate and the amplitude will restore. The PID control will maintain the tip-surface the separation so that the oscillation amplitude is fixed.

If the cantilever oscillation amplitude is kept at small value (<20 nm), the tip has to work in the weak interaction regime where the vdW force dominates. The tip-surface separation is larger (>1 nm) compared with previous two modes. The tip does not touch the surface and is away from the liquid layer. Since the there is not dampening to the tip, the vdW potential will affect the resonant oscillation frequency. The resonant frequency is used as a process variable for feedback control[38].

2.1.1 Piezo Force Microscopy

The working principle of Piezo Force Microscopy is depicted in the schematic diagram shown in Figure 19. A triangular silicon nitrite cantilever is used with a tip situated at its apex. It has typically a low spring constant k~0.01 N/m and a fundamental resonant frequency 7 kHz in its free state in air. When this AFM works in contact mode, the tip end is constrained by the sample surface and only higher-order mechanical vibrations are allowed. Considering the triangular shape, there will be a set of eigenmodes of vibration, as indicated in Figure 20, where schematically one is sketched in Figure 20 b). In that mode, both the tip end and base of the cantilever are treated as fixed. In general, the touch-down frequency differs from the free-state

resonant frequency. All these vibrations can be detected by the laser deflection system. The deflection of the cantilever can induce both vertical and lateral motions of laser spot, each of which can be detected by a pair of photodiode as labeled in Figure 19. To measure the piezo response of ferroelectrics, we applied AC electric field across interdigitated electrodes. If the sample is piezoelectric, which is always true for ferroelectrics, the electric field induces a small mechanical vibration on the sample surface. This vibration is coupled to the cantilever through the tip-sample interaction. The resonant curves of such cantilever are measured as shown in Figure 22 and Figure 22 for vertical and lateral modes. When the tip touches the sample surface, it is assumed to be fixed. The vibration mechanism is different from the case of non-contact mode AFM. Topographic features can still be measured by detecting the reflected spot position on quadruple photodetectors. In addition, the vibration motion of tip is measured by lock-in detection. In this case, the tip can also work as a mechanical preamplifier to detect small localized vibrations on the sample surface at the cantilever's resonant frequencies.

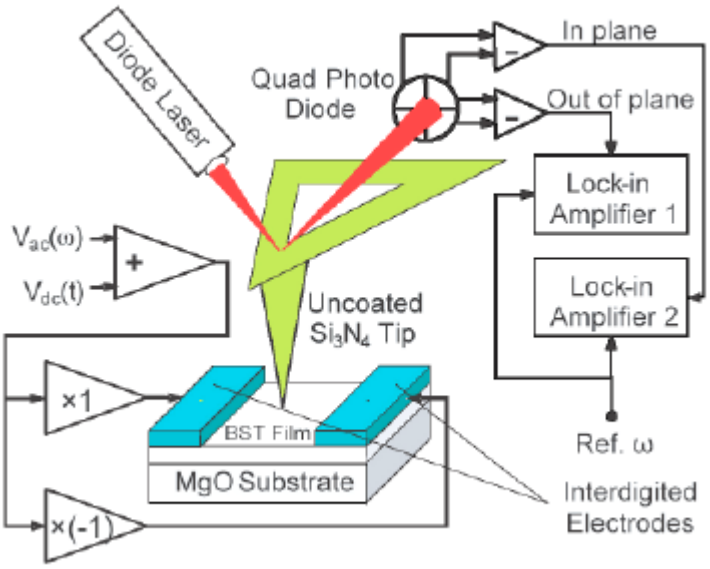

Figure 19 Piezoforce microscope configured for in-plane ferroelectric polarization detection

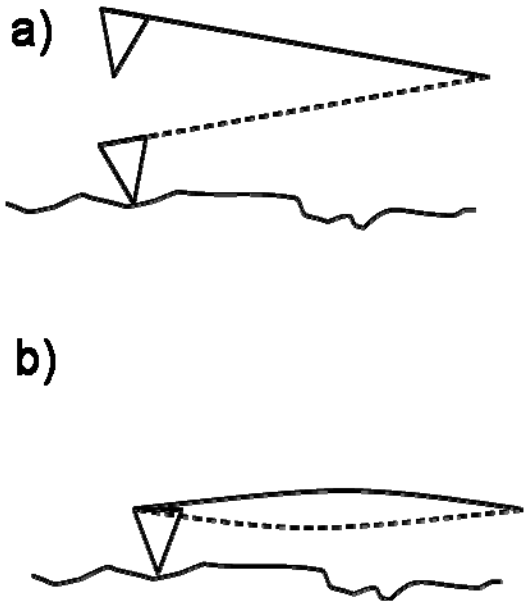

Figure 20 Non-contact mode a) and contact mode with high order vibration b). In a), the tip end is free. In b), the tip end is fixed. The resonant frequency strongly depends on tip-sample boundary condition.

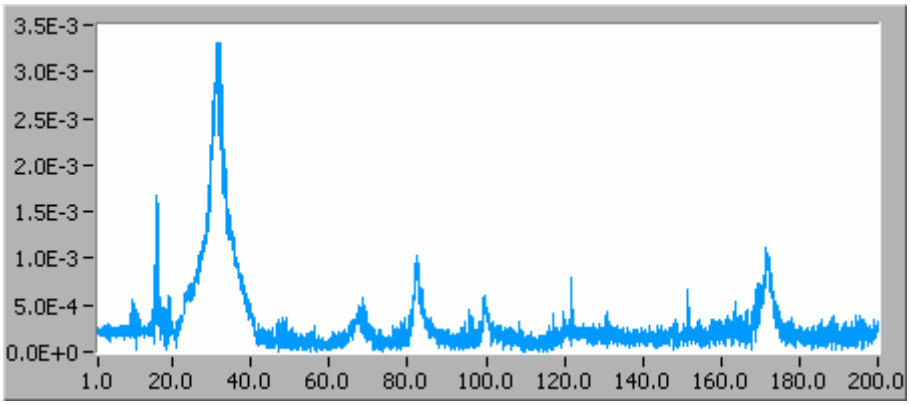

Figure 21 Resonant curve of silicon cantilever measured when touch down in contact mode. Vertical motion is recorded

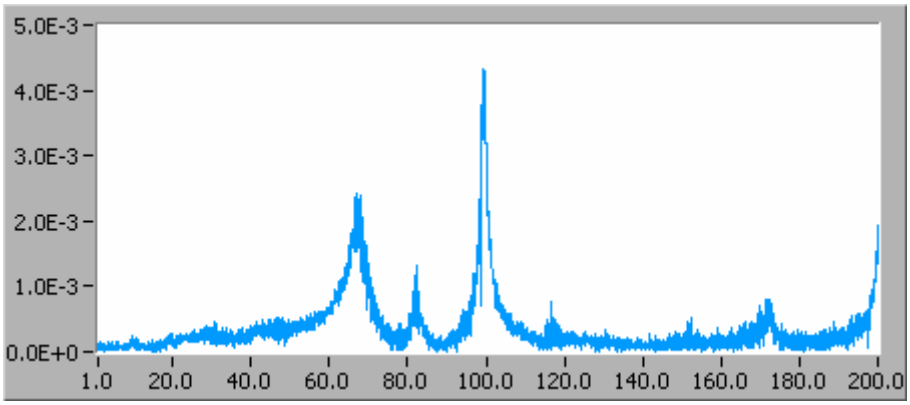

Figure 22 Resonant curve of silicon cantilever measured when touch down in contact mode. Lateral motion is recorded. Horizontal axis: Hz. Vertical axis: amplitude of oscillation, arbitrary unit.

One of the images obtained from the PFM is shown in Figure 23. Image b) shows the surface profile (topographic). The grain size is in the range of 400-500 nm. Image a) indicates the error signal of PID process variable, which ideally is zero. Image c) is the amplitude of cantilever oscillation which is proportional to the local surface vibration. Image d) shows the phase of oscillation, which measures the domain orientation. Image c) and d) provides further information which is not revealed by contact-mode AFM. Comparing these two channels, we can tell that there are domain walls exist within single grains, as in region 2 and 3. Domain walls may go across several adjacent grains, as in region 1.

The AFM scanning stage is itself based on PZT, a ceramic piezoelectric material. Due to piezoelectric hysteresis and thermal drift, the scanner usually won't repeat its position between consequent image acquisitions even when same control signals are applied (open loop). To compare between images of various bias electric field, we interleave scan lines[39] to maximize overlap of images acquired under varying conditions. A comparison of piezo force effect at different DC electric fields is shown in Figure 24.

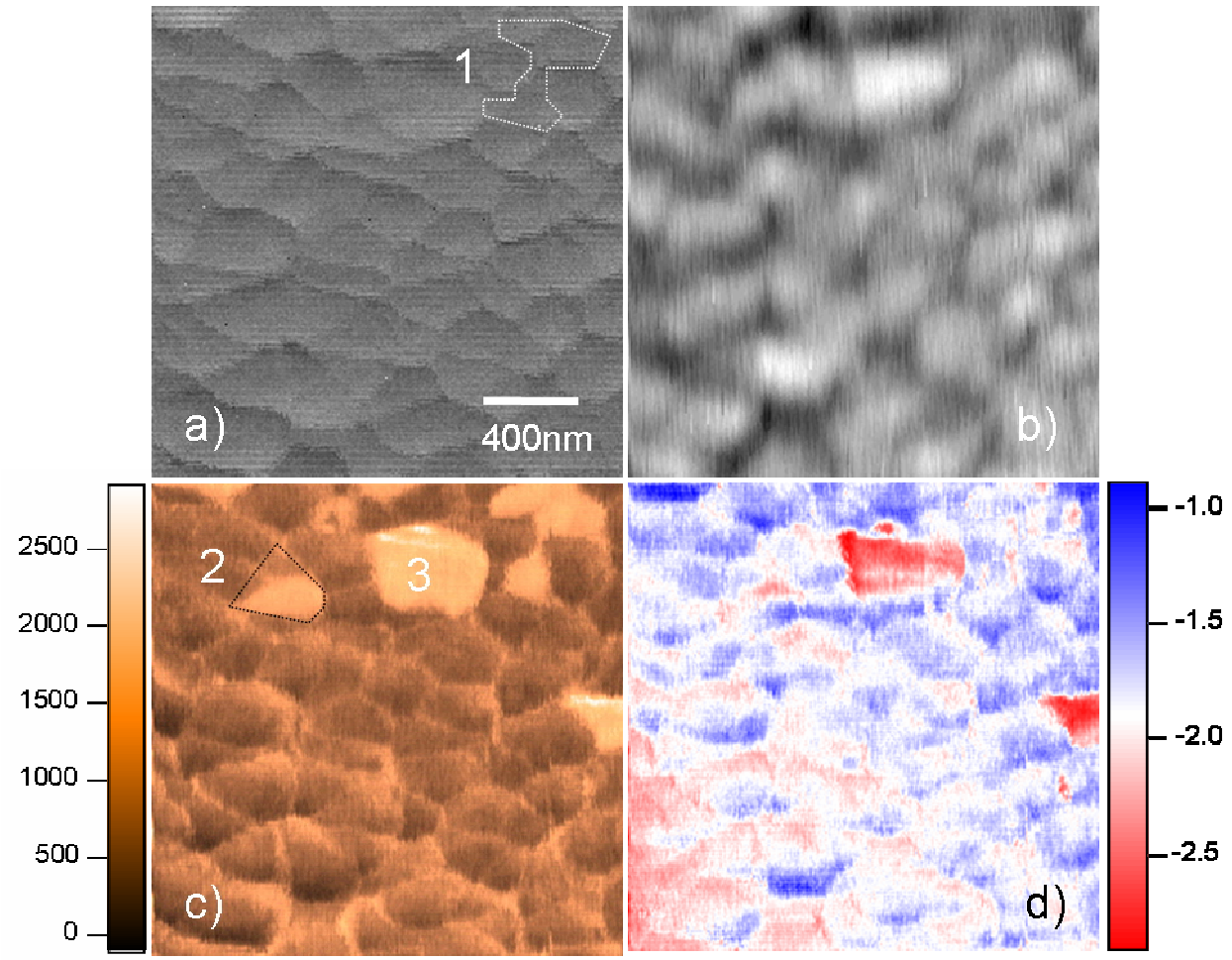

Figure 23 2x2μm PFM scan of BST/MgO sample. a) error message of AFM feedback control. b) Topography. c) Amplitude of PFM response. d) Relative Phase of PFM response.

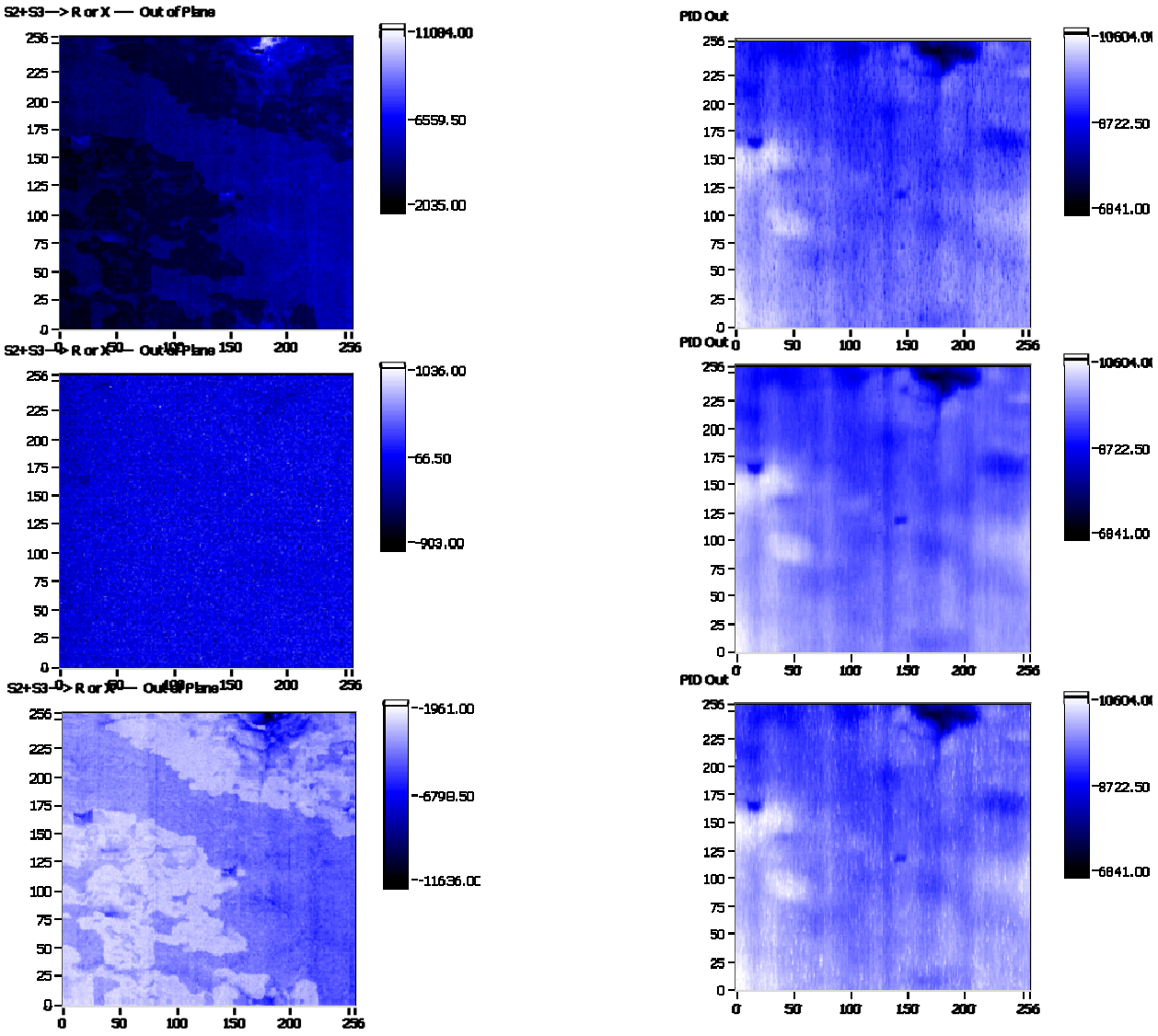

Figure 24 PFM images (left column) at different electric fields. The fields are, from top to bottom: +20kV/cm, 0, -20kV/cm. Topographic images (right column) are recorded simultaneously showing no change in height at different fields. The size of images are 5 μm×5 μm. Gray scales are in arbitrary units.

2.1.2 Ferroelectric Domain Patterning with Piezo Force Microscopy

Epitaxial $BaTiO_3$ film grown on silicon substrate has been extensively studied. The successful integration of ferroelectric material with semiconductors is the foundation for various novel functional electronic devices. Due to the lattice mismatch and differential thermal expansion between $BaTiO_3$ and silicon, most reported $BaTiO_3$/Si films are in-plane polarized. This is not

favorable to some applications like ferroelectric memory devices and a proposed quantum computer scheme[40]. Ferroelectric memory devices require top and bottom electrodes. In the suggested quantum computing scheme, spin coupling in the underlying silicon is controlled by the out-of-plane polarization of an overlying ferroelectric film. Schlom et al. have carried out a careful analysis and successfully developed such films. Their solution is to use a $(Ba_xSr_{1-x})TiO_3$ buffer layer in between $BaTiO_3$ and underlying silicon[29] (Figure 25). A series of such films with variation in Ba-Sr ratio and buffer layer thickness were grown and sent to investigate on our home-built AFM as well as on a commercial AFM to verify their ferroelectric out-of-plane polarizations.

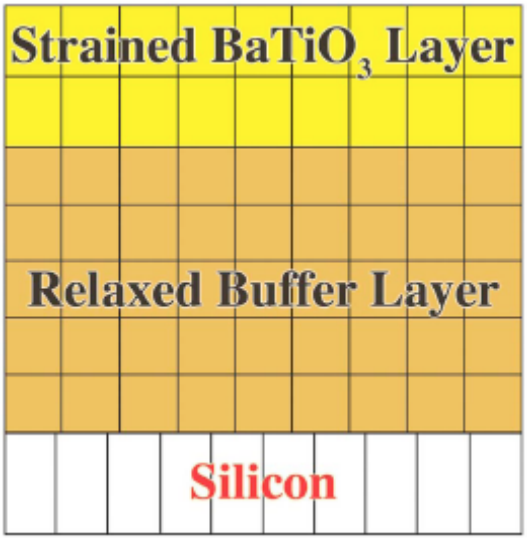

Figure 25 Diagram of $BaTiO_3$/Silicon heterostructure

Our home-built AFM was configured to write and read out-of-plane domains, as in Figure 26. For conductivity, we sputter deposited the tip side of our silicon nitrite cantilever with about 20 nm gold. We grounded the cantilever, and applied DC and/or AC voltage through the back of the silicon substrate. The silicon is p-doped and has electrical conductivity of 0.012 $mOhm^{-1}$ cm^{-1} (www.chemicool.com), so it can be used as a bottom electrode. Patterns were written to the film through application of a DC voltage synchronized to the raster scan of the sample stage. This step poles the ferroelectric film and creates nano-scale domains as a result of the localized electric field confined by the tip-film boundary condition, as sketched by the inset of Figure 26. The amplitude of the AC signal, 0.1~0.2 Volts rms, is small compared

with the DC voltage which is several Volts. The AC detection loop is usually disabled in the writing step, however, it can be enabled to monitor the writing procedure with negligible effect on the creation or erasure of domains. A photodiode is used to detect the cantilever motion. A PID loop uses the DC component of the photodiode signal as a process variable to adjust the sample z stage. The computer records the PID feedback as the surface profile. A lock-in amplifier amplifies the out-of-plane signal AC component at the driving frequency. During the reading step, the DC signal is disabled. The phase channel of the lock-in amplifier provides information about the domain orientation. Figure 27 shows a checker pattern written on a $BaTiO_3$/BSTO/Si(P^-) structure.

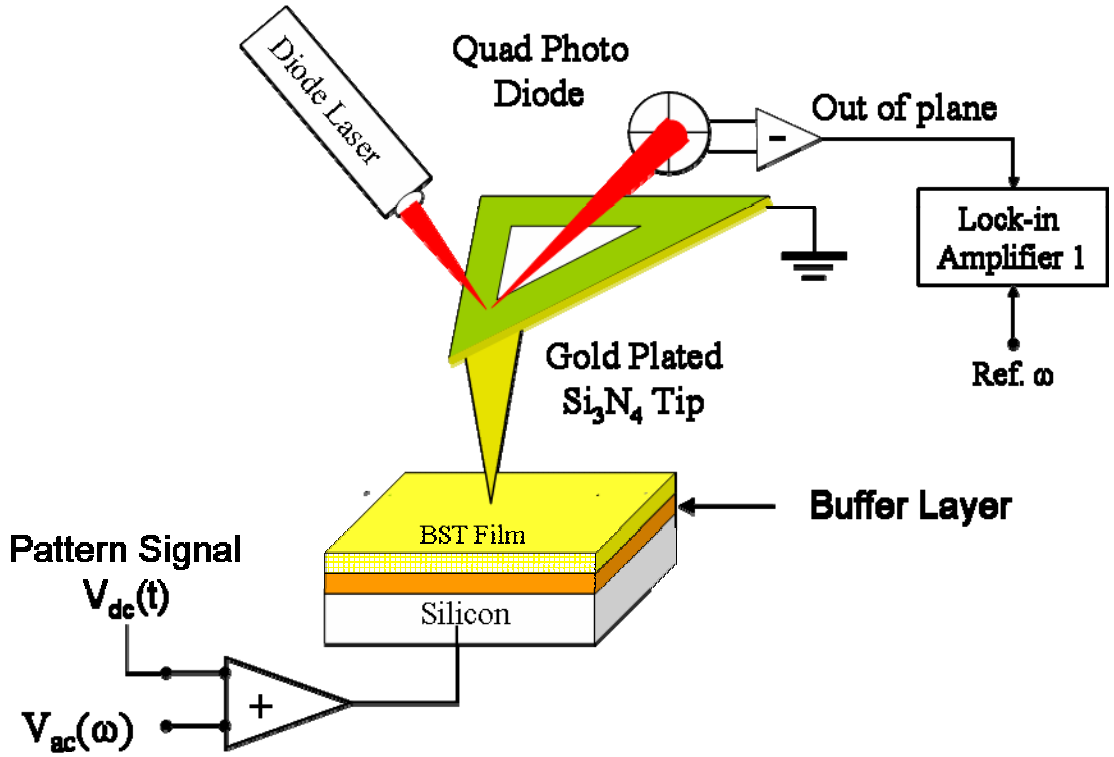

Figure 26 Piezoforce microscope configured to write and read out-of-plane ferroelectric domain pattern.

The checker pattern was written with +/-10 poling voltages correspond to black or white squares, and read with V_{dc}=0, V_{ac} = 0.30V_{rms} at f =63.7kHz. The relatively smaller checker pattern is residual domains of previous scan. In the same fasion, a horse picture was written to this sample. The original picture and readout from the film is show in Figure 30.

A 100 Å $BaTiO_3$/300 Å $Ba_{0.7}Sr_{0.3}TiO_3$/Si (001) sample is tested on a commercial Asylum MFP 3D AFM. Its circuit is modified to carry out the similar writing and reading function in

piezo force microscopy mode. V_{dc} = +/-2 Volts are applied to pole the domains while V_{ac} =0.07V_{rms} is typically used to read out (Figure 28).

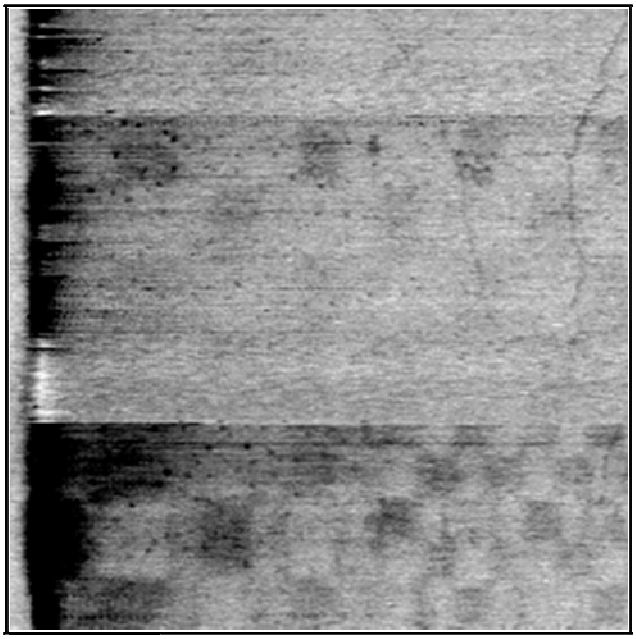

Figure 27 Checker pattern written on $BaTiO_3$/Silicon heterostructure. AFM contact mode is used to write the pattern and piezoforce microscopy is used to do read out. This image is obtained on the home built AFM. Images size is 5 μm × 5 μm.

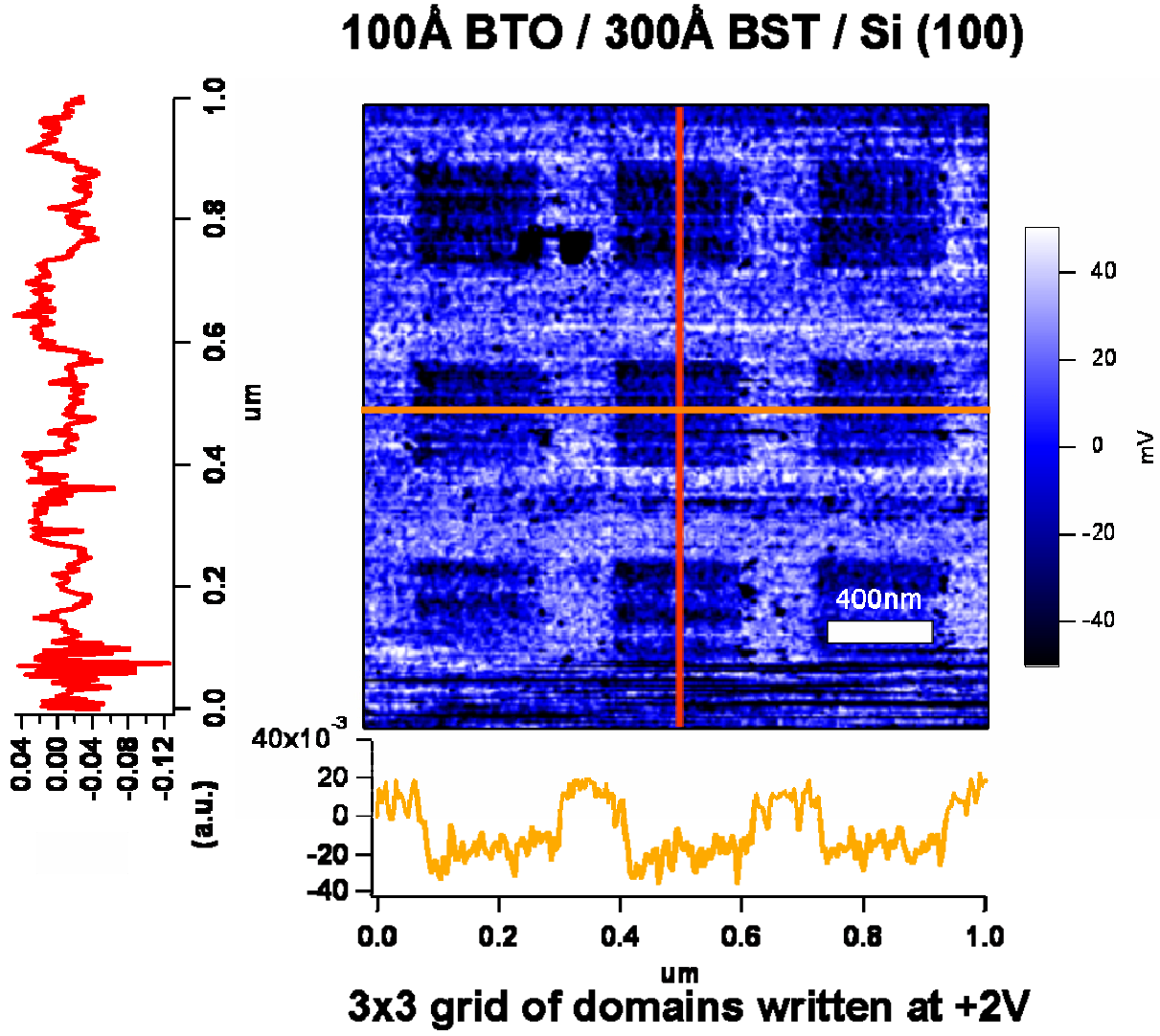

Figure 28 Square domains written on $BaTiO_3$/Silicon heterostructure. This image is obtained on a commercial Asylum MFP3D AFM modified to work at piezo force microscopy mode.

We repeated the write-read, erase-read and rewrite-read steps. The corresponding readouts are shown in Figure 29. The reversibility of domains convinced us that the film is ferroelectric and has out-of-plane polarization.

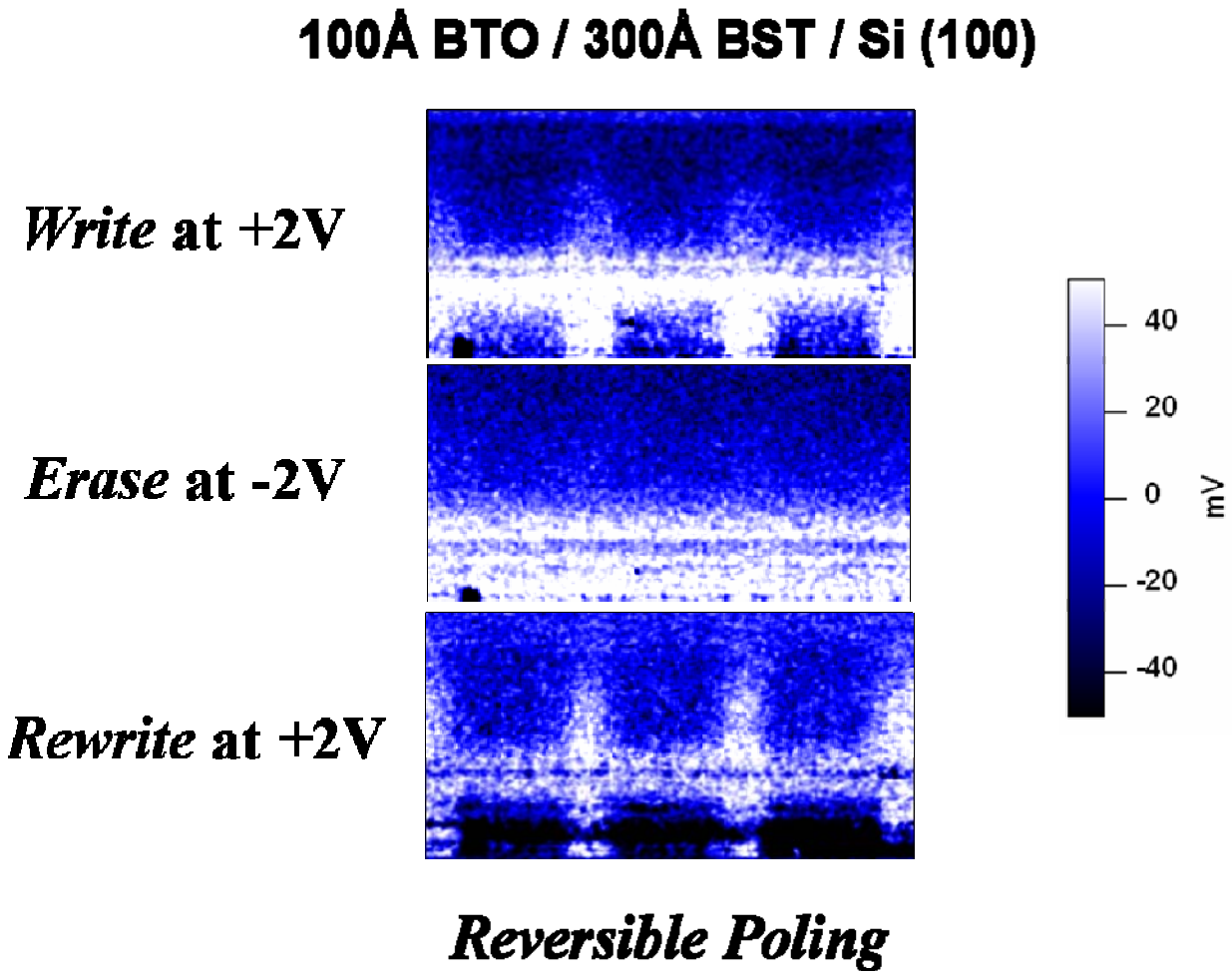

Figure 29 All three images are readouts with V_{dc}=0. Color level scales with the lock-in amplifier output. Each square pattern is 400 nm x 400 nm in size.

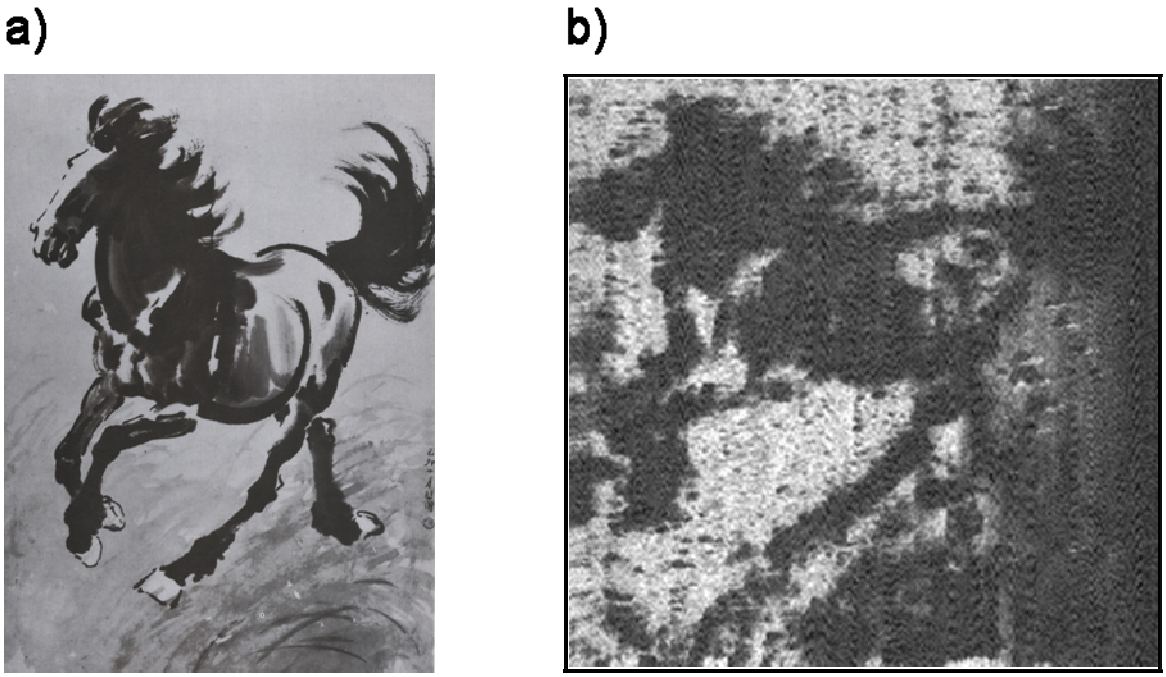

Figure 30 A horse pattern written on a BTO/BSTO/Si heterostructure. a) is the original picture and b) is the readout (5 μm x 5 μm) a few minutes after the writing (poling) step.

2.2 CONFOCAL SCANNING OPTICAL MICROSCOPY (CSOM)

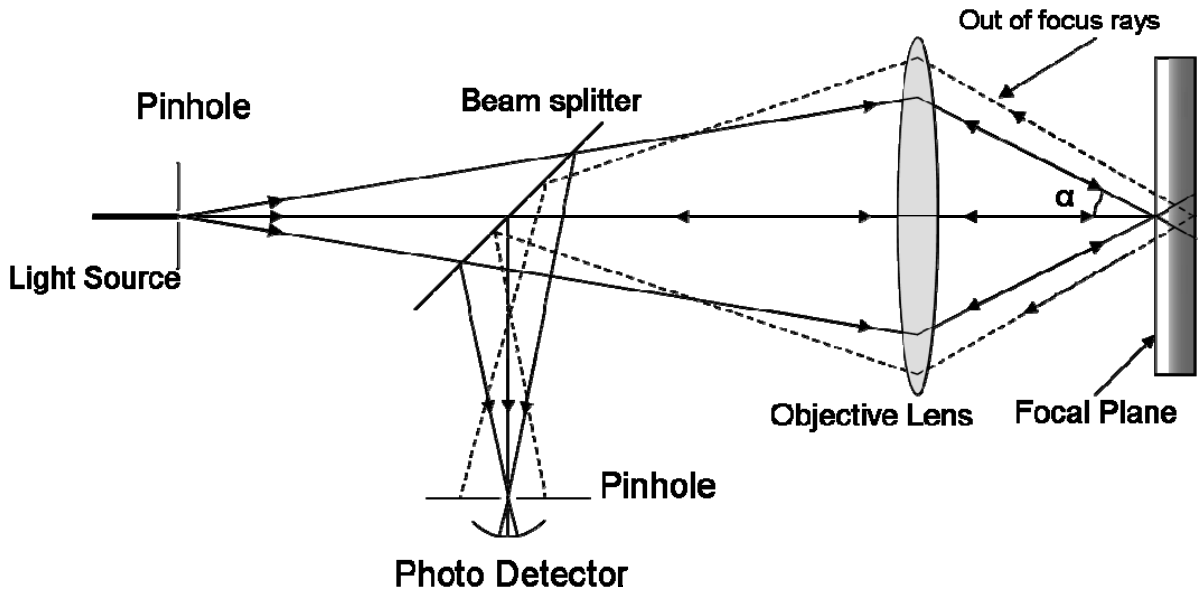

Figure 31 Principle of Confocal Scanning Optical Microscopy. Scattering from out of focus region in the object is rejected by the pinhole (spatial filter) at the image focal plane.

Confocal scanning optical microscopy is a powerful imaging technique used extensively in the characterization of ferroelectric thin films. Figure 31 shows the working principle for CSOM. A light source goes through a small pinhole and is focused by an objective lens onto the specimen. The same lens collects reflected light and focuses it at the conjugate back focus point where a pinhole is inserted before the detector. The first pinhole works as a spatial filter to remove higher spatial modes in the light source other than the fundamental Gaussian mode. The detector pinhole reduces the amount of unwanted stray light reaching detector by allowing only light from the vicinity of objective forward focus point to get through. The application of both pinholes improves the lateral and axial optical resolution. In such a configuration, assuming no geometrical aberration introduce by optics, diffraction limited lateral resolution is achieved which is given by[41]

$$\Delta x = 0.82\frac{\lambda}{NA} \tag{25}$$

NA is the numerical aperture of optical system and λ is the wavelength of the light source. If a flat surface is in place of the sample, a simple paraxial theory can be applied to model this response as

$$I(u) = \left(\frac{\sin \frac{1}{2} u}{\frac{1}{2} u} \right)^2, \qquad (26)$$
$$u = \frac{8\pi}{\lambda} z \sin^2 \frac{1}{2} \alpha$$

where z represents the axial distance of the flat surface. z =0 means the flat surface is at the focal plane. s*inα* is the numerical aperture. The axial (z depth) resolution is given by:

$$\Delta z = \frac{\lambda}{2(NA)^2} \qquad (27)$$

where Δz is the FWHM of the $I(z)$ against z curve.

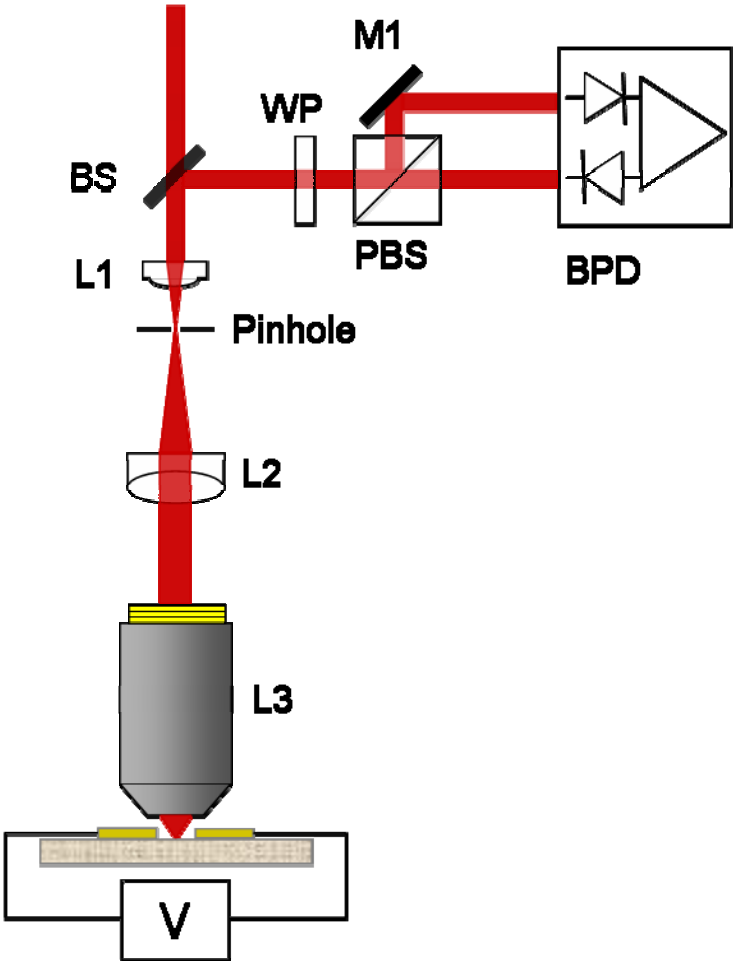

Figure 32 Reflection mode Confocal Scanning Optical Microscope (CSOM) configured for infinity corrected objective lens. BS: Non polarized beam splitter. PBS: polarized beam splitter. WP: Waveplate. L1: Aspherical lens. L2: Collimation lens. L3: Objective lens. BPD: Balance Photo Detector. M1: Flat Mirror.

Figure 32 shows the beam path of our confocal scanning optical microscope based on an infinity-corrected optical system, which allows insertion of parallel optics without introducing optical aberration to the image. Parallel optics includes filter, polarizer, wave plate, AOM, etc. According to Eq. (26), we measured our system performance. Figure 33 shows the reflection intensity detected as a flat mirror surface translate through the focus plane (z = 0) of a Zeiss (NA=0.95) objective lens. The solid curve represents the calculation using Eq. (26). The discrepancy between theory and measured value indicates somehow sub-optimal optical configuration.

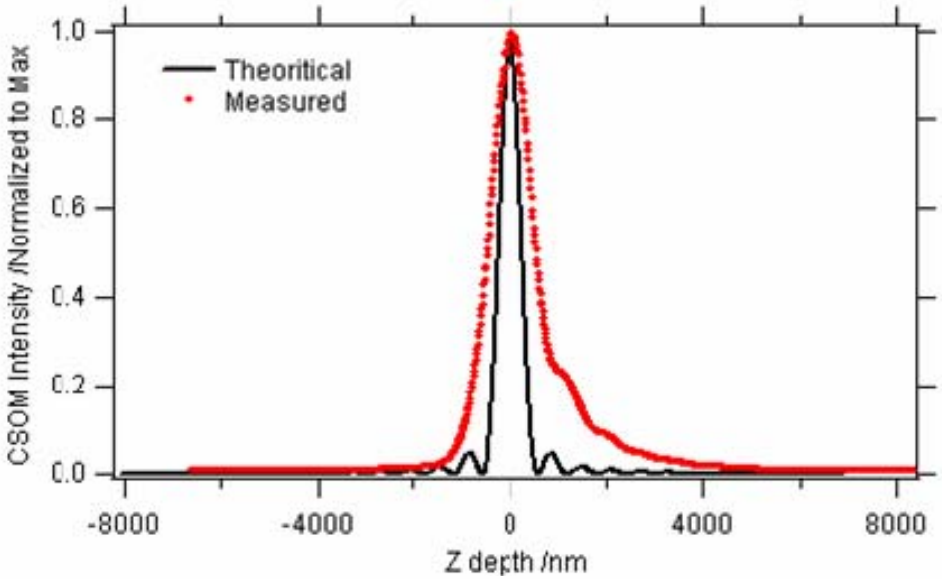

Figure 33 Measured plane response of one of our Confocal system using a Zeiss objective with NA 0.95.

The theoretical z-depth resolution is given by:

$$\delta Z = \frac{\lambda}{2(NA)^2}, \text{ FWHM plane response}$$
$$for \lambda = 820nm, NA = 0.95, \delta Z = 454nm$$

Using the system with a Zeiss objective, the measured z resolution is about 900 *nm.*

The axial resolution made confocal microscope is an ideal tool for ferroelectric thin film domain imaging[42,43,44,45]. Figure 34 shows CSOM images of a 50 nm $SrTiO_3$ thin film deposited epitaxially on a $DyScO_3$ substrate. Polarized light is used to illuminate the sample. The direct reflection intensity is recorded as in a). The dark region is the electrode and the light region is the bare film. The film thickness is an order smaller than the light wavelength (820 nm) and the axial resolution. To enhance the contrast between domain structures, an AC electric field (85 kHz) is applied and a lock-in amplifier is used to obtain image b), where strip structures are revealed. A detailed optical measurement was done on this sample.

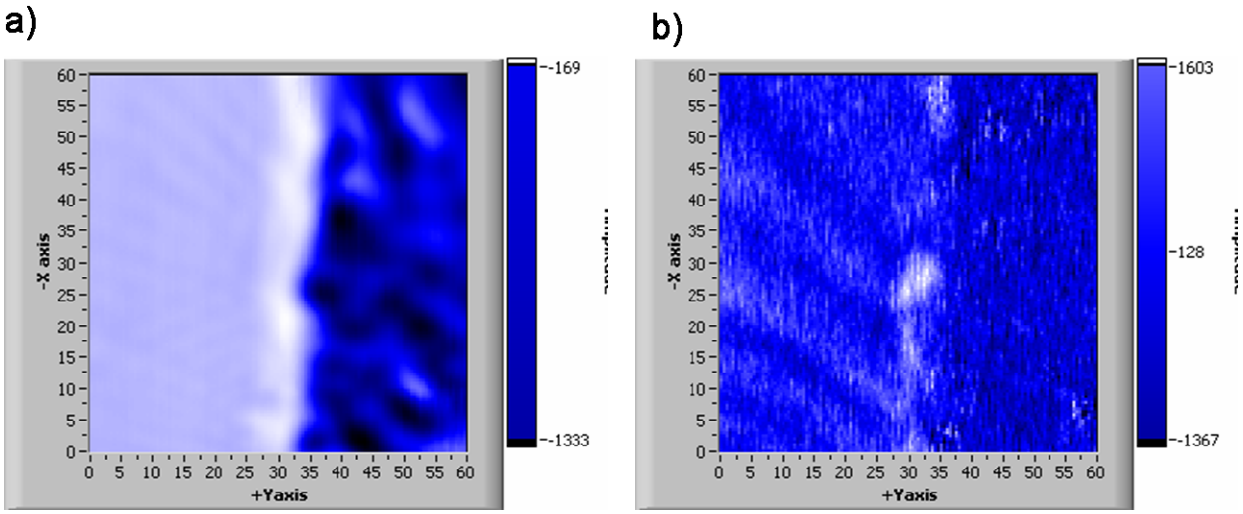

Figure 34 CSOM Images of $SrTiO_3$(500Å)/$DyScO_3$. a) DC intensity signal. b) Lock-in channel reveals strip structures which indicate variation of optical axis. Image sizes are 20 μm x 20 μm

2.3 APERTURELESS NEAR FIELD SCANNING OPTICAL MICROSCOPY (ANSOM)

2.3.1 Beyond the Optical Diffraction Limit

Conventional optical microscopy has a theoretical resolution limit close to about $\lambda/(2NA)$, where NA is the numerical aperture, as pointed out by E. Abbe in 19th century. It was also believed that $\lambda/2.3$ is the lower bound for optical imaging and recording. Since then, various methods have been developed that yield optical resolution much better than this. Abbe's rule still holds, but the newer methods people use differ from conventional optical microscopy either in the way that the object is illuminated, or in the way that light is collected. Alternately, super-resolution can arise due to a nonlinear interaction between a local probe and the target object. Two photon fluorescence microscopy makes use of the non-linear photon absorption of fluorophores to achive enhanced resoluiton[46,47]. Two photon quantum entanglement has also been implemented to get better resolution[48,49], and theoretical proposals have been developed that would enable one to achieve λ/n spatial resolutions for lithography in which n-photon excitation create n-photon quantum entanglements[50]. The spatial mode of a Gaussian beam can also affect the resolution.

By turning the linear polarized Gaussian beam into radially polarized light, the intensity distribution at the focus sharper, thus enhance the resolution[51]. Volker Westphal *et. al.* have claimed to achieved λ/50 resolution using Stimulated Emission Depletion for fluorescence microscopy[52]. All these successful and promising methods and proposals can be implemented for far-field optical microscopy.

Another branch of high-resolution optical microscopy combines the techniques of scanning probe and near field optics. The first modern optical near-field instrument was referred to as an "optical stethoscope", in analogy with a doctor's stethoscope used for measuring a patient's heart beats. The sound frequencies of the heart range from 30-100 Hz, corresponding to a wavelength of around ~100 m for biological tissue. The stethoscope, placed close to the heart, can resolve the location of a beating heart to within 10 cm, this accuracy corresponds to a spatial resolution of ~ λ /1000 for the system. The near-field optics uses a tapered optical fiber with an aperture about 20~100 nm in diameter defined by metallic coating. This aperture is brought close to surface of interests with feedback control similar to AFM. The illumination and collection of light can go through the other end of fiber or another objective lens, corresponding to collection mode or illumination mode respectively. Due to the penetration depth (10-20 nm) of light in to metal cladding, the actual size of the aperture is limited to around 20 nm, hence the resolution has a lower boundary limited by the actual aperture size. To further increase the resolution of near field optics, the use of a sharp probe–with no aperture–was proposed.

The first Apertureless Near-field Scanning Optical Microscope (ANSOM) was reported in 1994[53]. Its ultimate optical resolution is theoretically predicted to be ~0.1 nm, close to the atomic scale. Since then, a variety of ANSOM systems have been developed in different groups over the world for a range of applications, in parallel to the maturing of scanning probe techniques. Keilmann's group uses side illumination for materials surface infrared spectroscopic imaging[54,55,56,57]. Our ANSOM system is modified from the scheme of Zenhausern et. al[39]. It is composed of a confocal microscope and an atomic force microscope. The transparent ferroelectric thin film (on substrate) is sandwiched between an objective lens and a Pt coated AFM tip, as shown in Figure 37.

2.3.2 Dipole-dipole Interaction model

The role of the conic probe in near-field optics can be elucidated by considering a dielectric sphere in proximity to a dielectric plane. The optical field is treated as a plane wave for simplicity with wavelength λ. The sphere has radius a which is in the Rayleigh limit ($a << \lambda$), and polarizability[58]

$$\alpha = 4\pi(\frac{\varepsilon_s - 1}{\varepsilon_s + 2})a^3 \tag{28}$$

When the electric field **E** is applied, the dipole moment of the sphere becomes $\mathbf{p} = \alpha\mathbf{E}$. The electric field generated by the dipole in return is, in the near-field limit ($2\pi r << \lambda$).

$$\mathbf{E}_p^{\parallel} = \frac{2\mathbf{p}}{4\pi\varepsilon_0 r^3}, \quad \mathbf{E}_p^{\perp} = \frac{\mathbf{p}}{4\pi\varepsilon_0 r^3} \tag{29}$$

Here r represents the distance from sphere centre, for the parallel and perpendicular condition, as indicated in Figure 35.

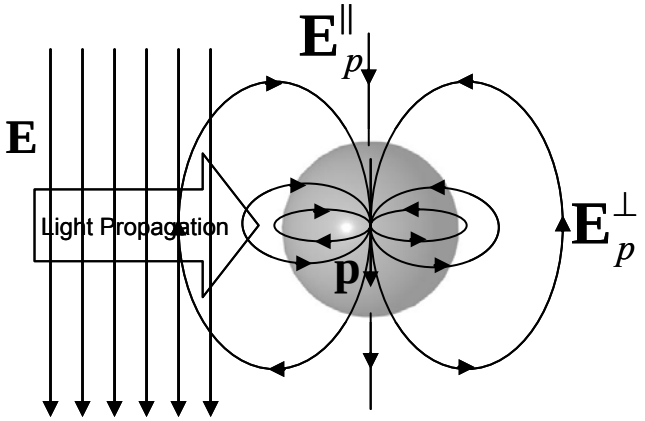

Figure 35 Dipole like behavior of a dielectric sphere in electric field

When this dielectric sphere is placed a distance r from a plane with dielectric constant ε, it induces an image dipole moment in the dielectric plane symmetrically at position r from the surface. If the applied electric field is perpendicular to the surface

$$p' = \beta p \quad \text{and} \quad \beta = \frac{\varepsilon - 1}{\varepsilon + 1} \tag{30}$$

then the electric field from the image dipole will be superimposed onto the applied electric field. The dipole moment of the sphere is then

$$p = \alpha\left(E + \frac{p'}{16\pi r^3}\right)$$

p can be derived to be $p = \frac{\alpha E}{(1 - \frac{\alpha\beta}{16\pi r^3})}$

$$\alpha_{eff}^{\perp} = \frac{\alpha(1+\beta)}{(1 - \frac{\alpha\beta}{16\pi r^3})} \tag{31}$$

The electric field at the surface $E_s = E(\frac{16\pi r^3 + \alpha}{16\pi r^3 - \alpha\beta})$

If the applied electric field is parallel to the surface

$$p' = -\beta p,$$

$$p = \alpha\left(E + \frac{p'}{32\pi r^3}\right) \tag{32}$$

p can be derived to be $p = \frac{\alpha E}{(1 + \frac{\alpha\beta}{32\pi r^3})}$

The dielectric constant of the sphere is generally complex: $\varepsilon_s = \varepsilon_s' + i\varepsilon_s''$. If the sphere is resonantly polarized at the Frőhlich frequency [59], $\varepsilon_s' = -2$ and the absorption ratio is low, α is large and the $\alpha_{eff}^{\perp}$ is a highly nonlinear function of the distance between sphere and surface. For electric fields parallel to the tip axis, the induced image dipole moment is in the reversed orientation of the sphere dipole at the Rayleigh limit, so they almost cancel at the surface. The effective polarizability is much lower compared with the former case. Hence, the p-polarized light will scatter much more efficiently compare to s-polarized light in the ANSOM configuration.

The shape of a small particle can greatly affect its polarizability, even though its dimensions may be much smaller than the wavelength of light. Ellipsoidal, rod like and cone-shaped particles all have strong field enhancement at the elongated ends. Two metallic triangles in a bowtie arrangement and two metallic rods separated by a small gap both give enhancement of electric field strength in their gaps at certain wavelengths[60,61]. When probes with such geometry are placed close to a dielectric surface, the condition becomes similar to a dielectric

sphere. There will be a large localized enhancement for incident light with electric field polarized along the probe principal axis. However, if the incident light beam is tightly focused by an objective, the situation becomes more complicated than the incident plane-wave model[62]. Numerical simulations show that when the polarization is perpendicular to the probe axis, there will still be a localized enhancement in the vicinity of tip, although the enhancement is weaker than the parallel illumination condition[63], as shown in Figure 36.

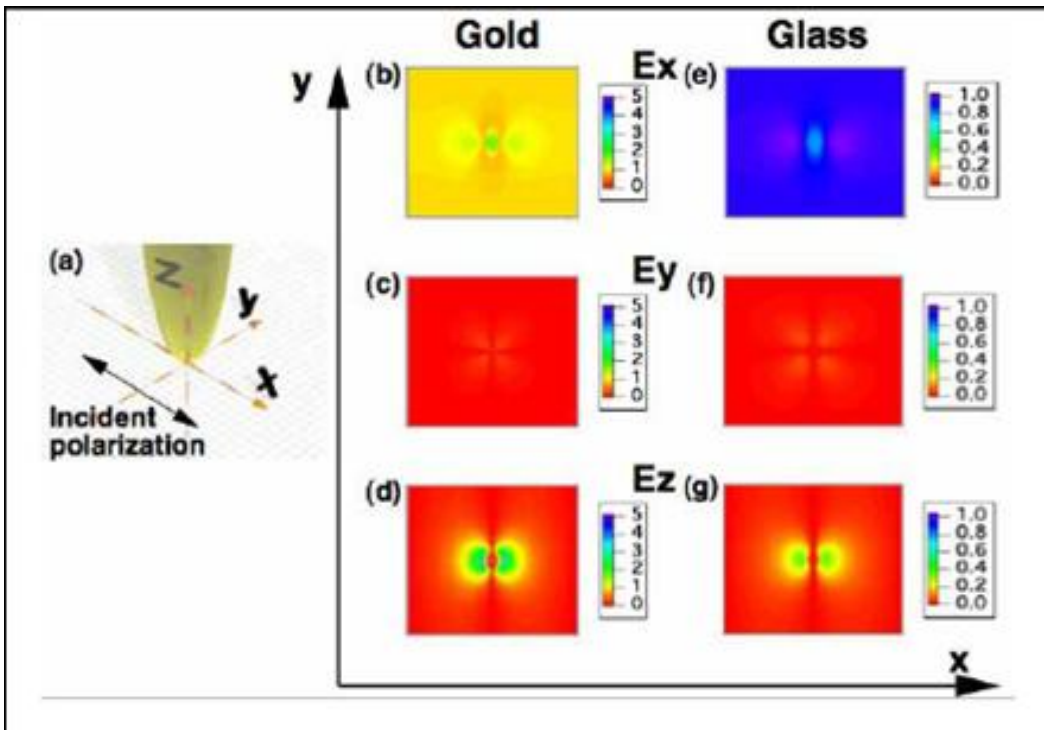

Figure 36 Electric field component calculated at the vicinity of gold and glass tips. Light is tightly focused from the bottom and a dielectric layer is inserted before the tip. From Ref [63].

2.3.3 Transmission-mode ANSOM

In our ANSOM system, the ferroelectric thin film is located between an objective and a metallic tip or a metal coated silicon tip, as shown in Figure 37. The near-field enhancement occurs when the tip is close to the surface in nano-meter range, and is confined to the tip vicinity. The light that is back-scattered contains dielectric information of the nano-scale area $\mathbf{E}_s$, a function of the tip-surface separation and the XY position for an inhomogeneous sample. However, light is still collected using far-field optics. The diameter of focused beam, in the diffraction limit, is about 0.5 μm. This is one order or magnitude larger than the size of tip. Therefore, the light scattering

from the sample bottom surface, plus scattering from the tip shaft, dominate in the far-field collected light. One has to take care on the signal detection to distinguish the near-field information from the far-field background.

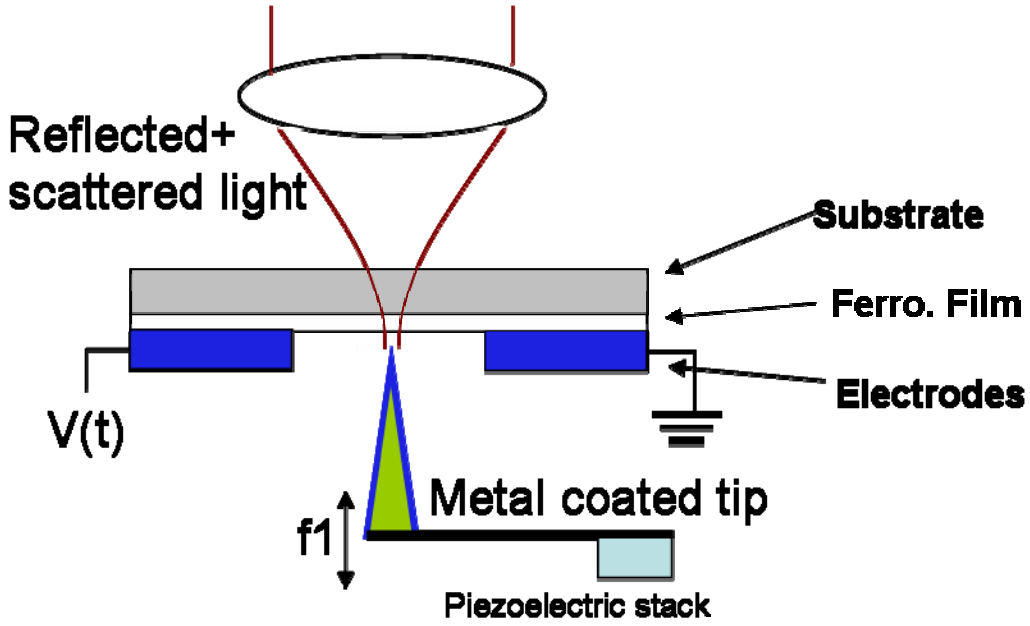

Figure 37 Aperture less Near Field Scanning Optical Microscope Setup.

Here we analyze the source of our ANSOM signal. First we assume the film has nanoscale inhomogeneous birefringence that we want to learn about. Laser light is focused at the tip-sample interface. Both reflected light field E_r from sample surface and scatted light of the vicinity of tip E_s will return through the original optical path. The polarization of reflected light is a function of the averaged birefringence over the diffraction limited spot area. The scatted light is also a function of the birefringence of the area in the tip vicinity. When the tip is closer to the surface, E_s becomes stronger, and more dependent on the localized nanoscale region; when it is further away from surface, E_s is weaker and provides average information over a larger area. So the polarization of E_s will oscillate with tip vibration. And $E_s << E_r$

$$E_s^{\parallel} = c_1^{\parallel}\cos(\omega t) + c_2^{\parallel}\cos(2\omega t) + c_3^{\parallel}\cos(3\omega t) + higher\ harmonics$$

$$E_s^{\perp} = c_1^{\perp}\cos(\omega t) + c_2^{\perp}\cos(2\omega t) + c_3^{\perp}\cos(3\omega t) + higher\ harmonics$$

$$E = E_r^{\parallel} + E_r^{\perp} + E_s^{\parallel} + E_s^{\perp}$$

After the polarized beam splitter,

$$I^{\perp} = \left|E_r^{\perp} + E_s^{\perp}\right|^2 = \left|E_r^{\perp}\right|^2 + \left|E_s^{\perp}\right|^2 + 2E_r^{\perp}E_s^{\perp}$$

$$I^{\parallel} = \left|E_r^{\parallel} + E_s^{\parallel}\right|^2 = \left|E_r^{\parallel}\right|^2 + \left|E_s^{\parallel}\right|^2 + 2E_r^{\parallel}E_s^{\parallel}$$

We can choose the polarization so that,

$\left|E_r^{\perp}\right|^2 = \left|E_r^{\parallel}\right|^2$, and using the balanced detection scheme, the detector output will be, taking into account the fact that $E_s << E_r$,

$\Delta I \approx 2E_r^{\perp}E_s^{\perp} - 2E_r^{\parallel}E_s^{\parallel} = 2E_r(E_s^{\perp} - E_s^{\parallel})$, where the $\left|E_s^{\perp}\right|^2$ and $\left|E_s^{\parallel}\right|^2$ terms have been neglected. The contribution from near field effect is amplified by a factor of E_r / E_s.

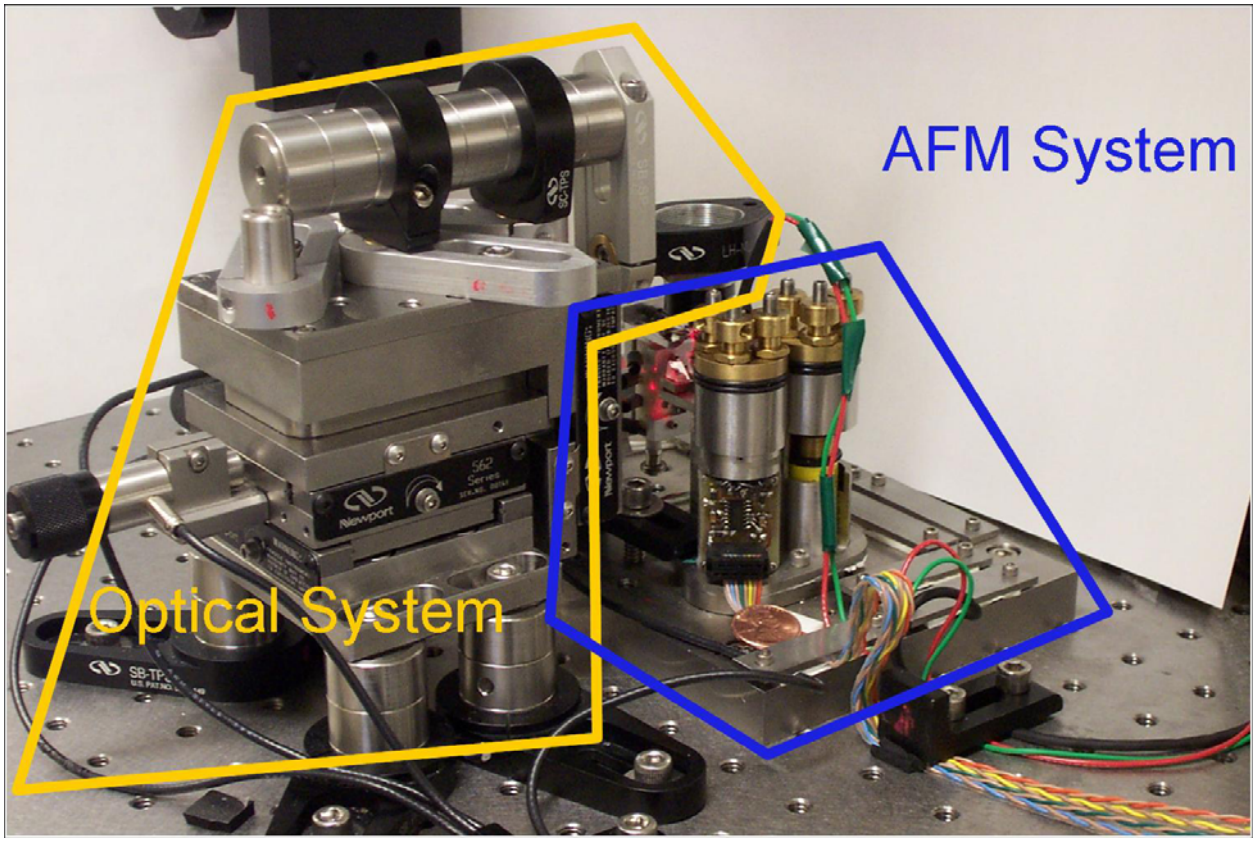

Figure 38 The ANSOM system consist of a inverted AFM and a confocal microscope

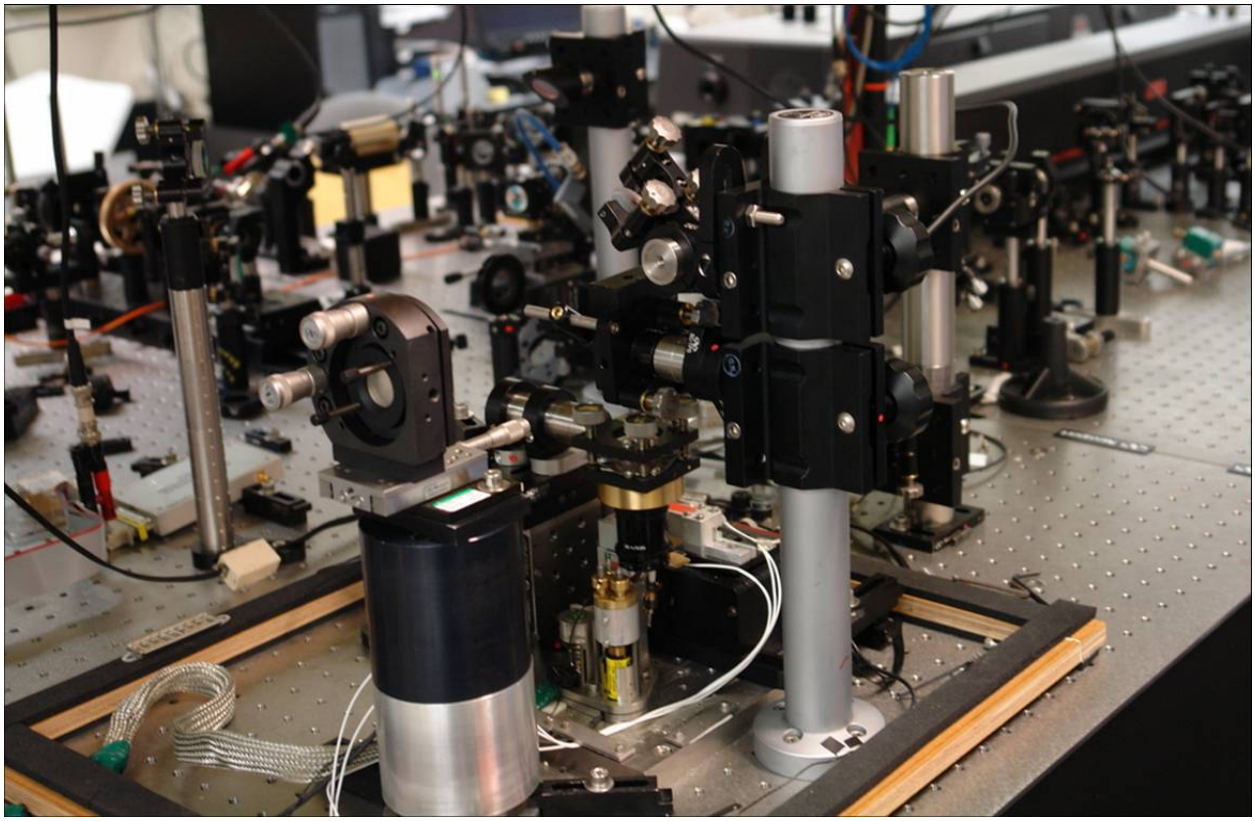

Figure 39 Another setup for ANSOM. A Zeiss high NA objective is mounted to get better depth resolution.

2.3.4 Second Harmonic Detection

In addition to the near field scattering, there is also far-field scattering from the tip shaft. The near-field effect exhibits a nonlinear dependence to the separation between tip and sample surface. By using second harmonic lock-in detection, the far-field background scattering can be effectively eliminated[57].

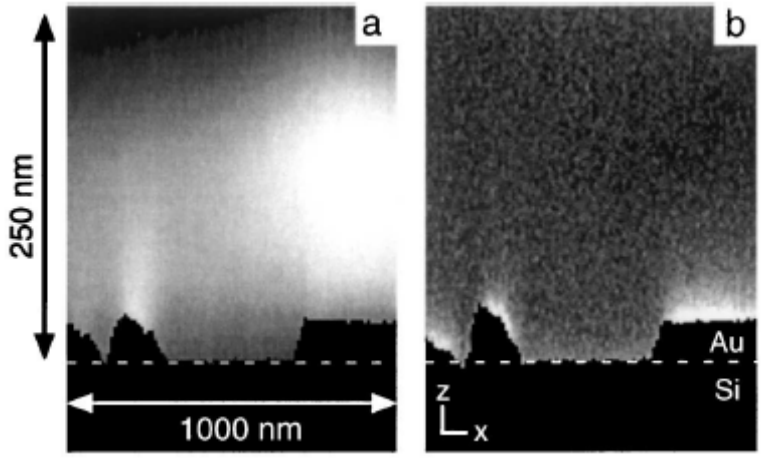

Figure 40 Back ground scattering can be reduced by using second harmonic lock-in detection scheme. From Ref. [57]

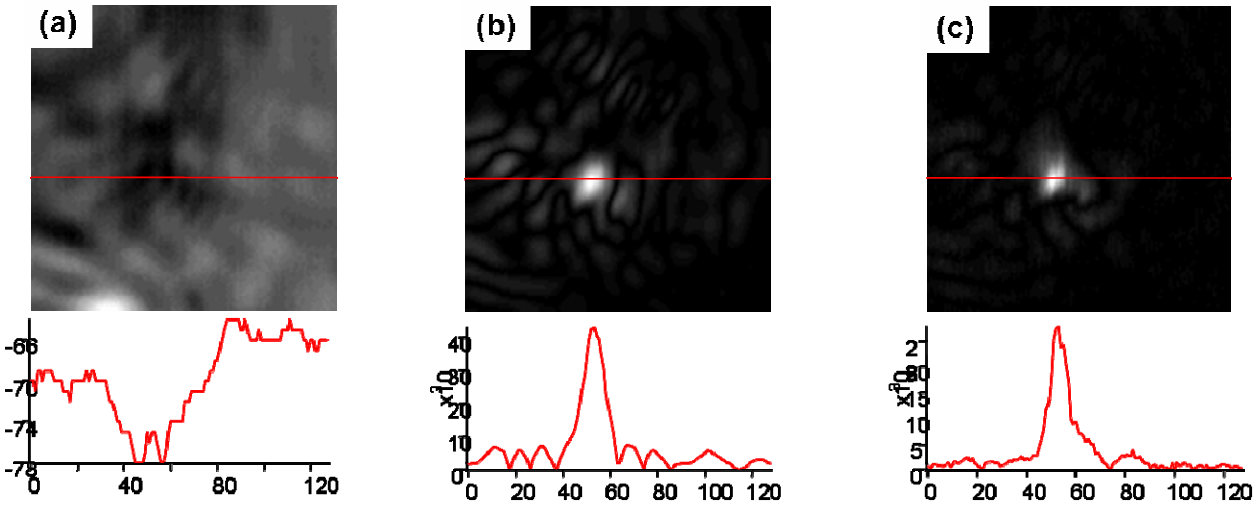

Figure 41 CSOM Images of tungsten tip of different channels. a) Signal intensity. The tip cannot be identified in this image. b) Lock-in channel at tip oscillation frequency, tip shows strong signal with background signal. c) Second harmonic detection scheme, background signal is reduced and scattering from tip end is enhanced.

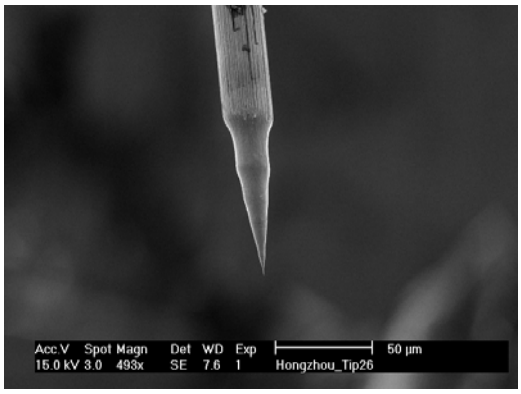

Figure 42 SEM image of the tungsten tip used for CSOM imaging in figure 19. Ferroelectric thin film is sandwiched between tip and objective

The CSOM tip images are 15 μm ×15 μm, which is smaller than the tungsten wire diameter (25 μm). So the background is from the shaft of tip, not the tuning fork tine.

Figure 43 shows an AFM topographic image and the corresponding obtained ANSOM signal by 2nd harmonic detection. Despite of strong correlation between optical 2nd harmonic (b) and mechanical (a) signal, 2nd harmonic shows features unrevealed by AFM measurements. Those features revealed by 2nd harmonic have resolution much better than diffraction limited resolution. However, an important question is the following: how to decouple the optical signal from topographic features? The answer appears in the following chapters (Chapter 5).

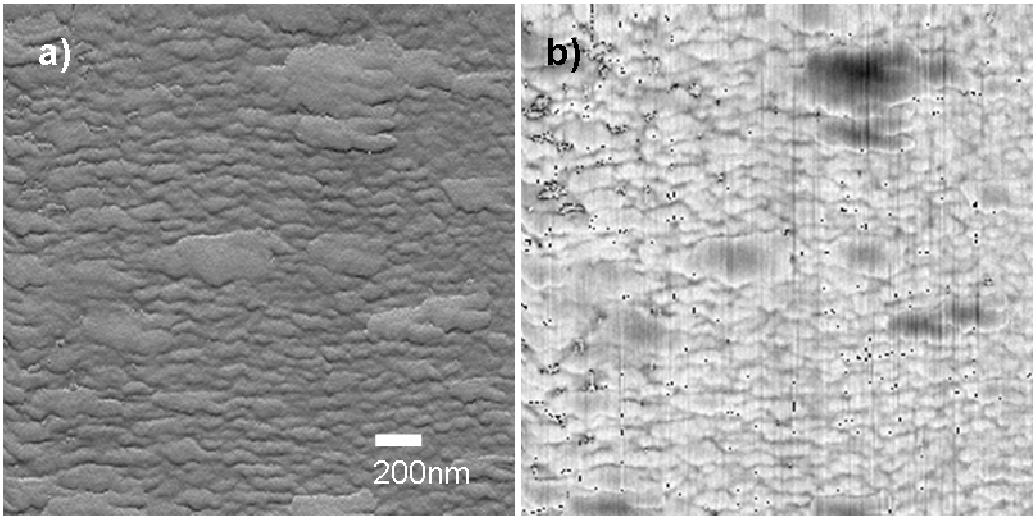

Figure 43 AFM image a) and simultaneously obtained ANSOM signal b) by second harmonic detection

2.4 ULTRA FAST TIME RESOLVED MEASUREMENTS

To learn about microwave properties of ferroelectric thin films, fast probes and sensitive measurement methods are needed. We have developed a system that combines an ultrafast laser, phase locking microwave electronics, and cascading lock-in detection techniques to achieve this goal. The three techniques are described briefly in the following sections.

2.4.1 Ultrafast Laser

Ultrafast laser pulses are generated through mode-locking of multiple longitudinal modes in a laser cavity. The field amplitude of optical wave is the integration of all the existing modes.

$$A = \sum_{n=-N}^{N} A_n e^{-i(\omega + n\frac{2\pi c}{2L})t + i\varphi_n} = e^{-i\omega t} \sum_{n=-N}^{N} A_n e^{-2\pi i n \frac{c}{2L} t + i\varphi_n} \tag{33}$$

L is the cavity length. In the CW mode, each mode has random phase φ_n. When it is mode locked, all modes have the same phase. The integration take the form:

$$A = e^{-i\omega t + i\varphi} \sum_{n=-N}^{N} A_n e^{-2\pi i n \frac{c}{2L} t} \tag{34}$$

All modes add up constructively at $t = m\frac{2L}{c}$. And the laser output are pulses at a fixed repetition rate $T = \frac{2L}{c}$, as shown in Figure 44. The pulse width is determined by the number N of locked modes in the cavity, and the relative amplitude of each mode. For a Gaussian distribution of amplitude between those modes, the pulse shape is also Gaussian. The pulse duration is $\Delta t = \frac{0.44}{N\Delta\nu}$, $\Delta\nu = \frac{c}{2L}$, alternately

$$\Delta t = \frac{0.44}{bandwidth} \tag{35}$$

The actual pulse with is affected by the dispersion in the laser cavity and the actual amplitude of each modes. Ti:Sapphire-based laser systems have a large gain bandwidth, ranging from 650 nm to 1100 nm. The most efficient range is near λ=800 nm and the spectral width with

achievable gain is about 100 nm. For L=1 m, Δv=1.5×10^8 Hz. While the band width is $\Delta\lambda \cdot c/\lambda^2$ = 4.69×10^{13} Hz. The theoretical shortest pulse width can be estimated as Δt=9.4 fs.

Our system includes a Coherent Mira 900 laser which is pumped by a multi-line Coherent Innova 300 Argon ion laser. At λ=820 nm, the largest spectrum range we measured is ~10 nm (Table 1), corresponding to a bandwidth of 4.4×10^{12} Hz. In this case, the pulse width is ~100 fs.

March 26, 2004 Innova 310+ Mira 900
Innova 310 I = 54.4A, Output power 8.0W

Mira λ /nm	FWHM/ nm	Mira Putput Power /mw	BPF Reading /mm	BP2 Reading /mm
770				
780		760	5.11	10.39
790		850	5.155	1.04
800		940	5.21	9.005
810		920	5.25	9.03
820	10	880	5.29	8.51
830		800	5.33	8.14
840		700	5.38	8.28
850		680	5.42	7.18
860		580	5.46	6.93
880	16	460	5.54	6.01
900	Failed to modelock		5.61	

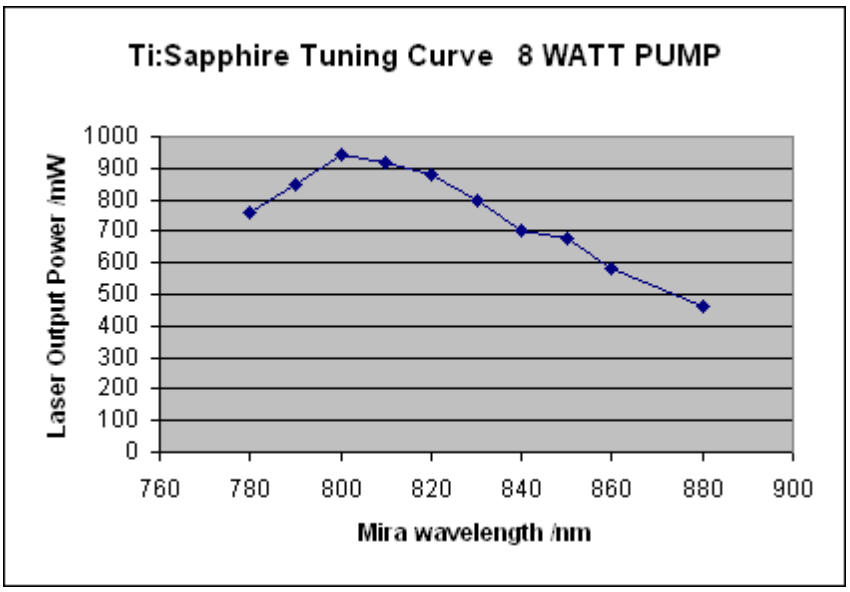

Table 1. Mira 900 center wavelength and bandwidth. Inset is the curve of measured maximum output power against center wavelength.

Pulses with duration such short or even shorter have been widely used for time resolved measurements. In our system, it works as a time domain probe to acquire fast electro-optic responses at microwave frequencies.

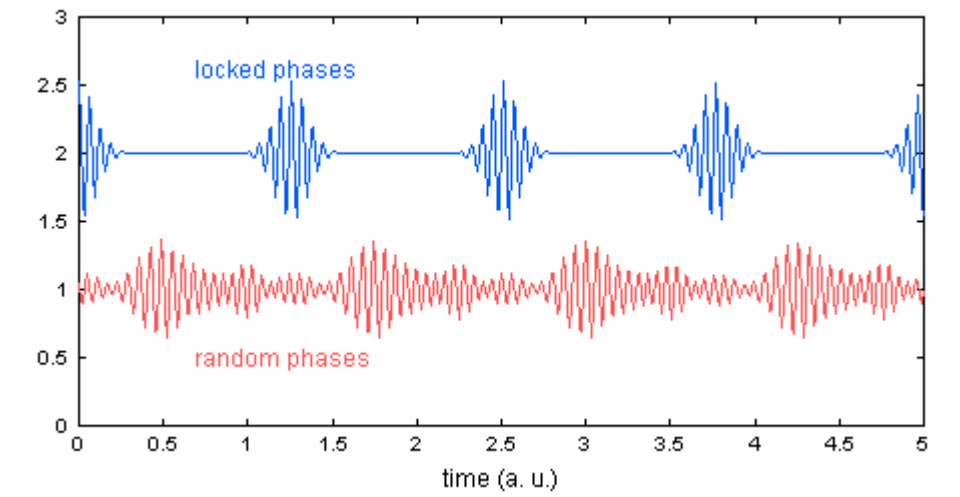

Figure 44. Difference between phase-locked and unlocked light from a laser cavity, adapted from the website of encyclopedia of laser physics and technology[64].

2.4.2 Phase Lock YIG Oscillator (PLO) at Microwave Frequencies

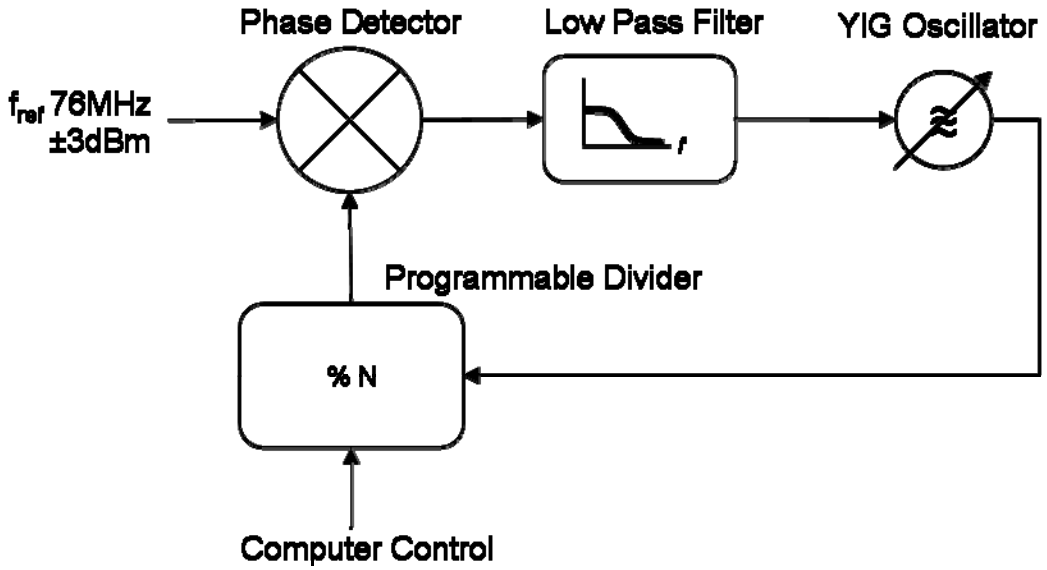

Figure 45 Simplified block diagram of phase-locked YIG oscillator.

The working principle of a microwave PLO is illustrated in Figure 45. The reference signal has a lower frequency. We use ~76 MHz, the repetition rate of our Mira 900 laser, as the reference. The YIG (Yttrium Iron Garnet) oscillator is the key to generating a microwave signal. The quality of signal is measured in terms of phase noise. Phase noise is the relative power as measured in frequency window offset from center frequency. As depicted in Figure 46, the lower the phase noise, the better the oscillator performance. The YIG sphere behaves as a low-loss microwave cavity[65]. Combined with a microcircuit (Figure 47), it creates stable microwave signals with very low phase noise. The instrument we employed has a phase noise lower than -115dBc/Hz @ 100kHz offset.

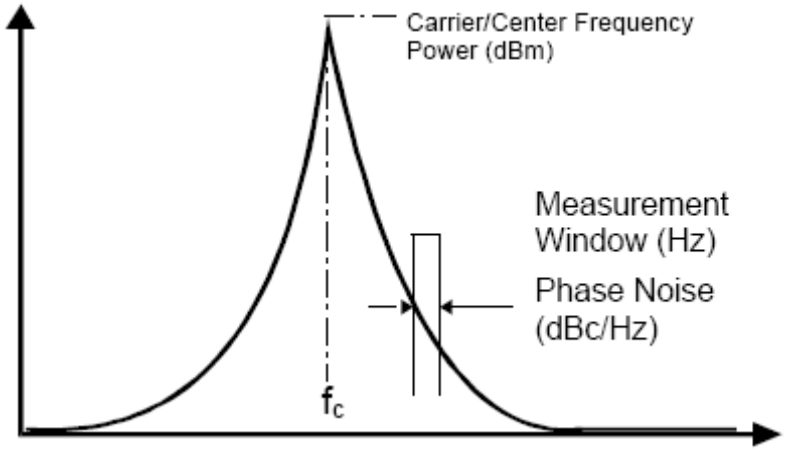

Figure 46 Phase noise definition, adapted from technique articles from Micro Lambda Wireless Inc.

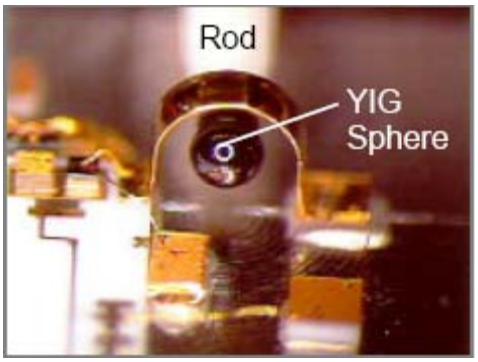

Figure 47 Micro circuit with YIG sphere to form a microwave oscillator. From same sources as Figure 46

The frequency of the YIG oscillator is tuned by magnetic field. A fixed DC current creates a permanent magnetic field through a coil around it. Another smaller coil with a smaller current is used to rapidly tune the field in response to feedback from the phase detector. The generated microwave passes through a divider. The divisor N can be can be controlled through a digital

port. The phase between generated signal and reference is converted to a voltage using a phase detector followed by a low pass filter. This voltage is stable only when the microwave frequency is an integer multiple of the reference. Therefore, the stability of voltage level is used to judge whether the microwave is locked to the laser repetition frequency.

2.4.3 Programmable Delay Line

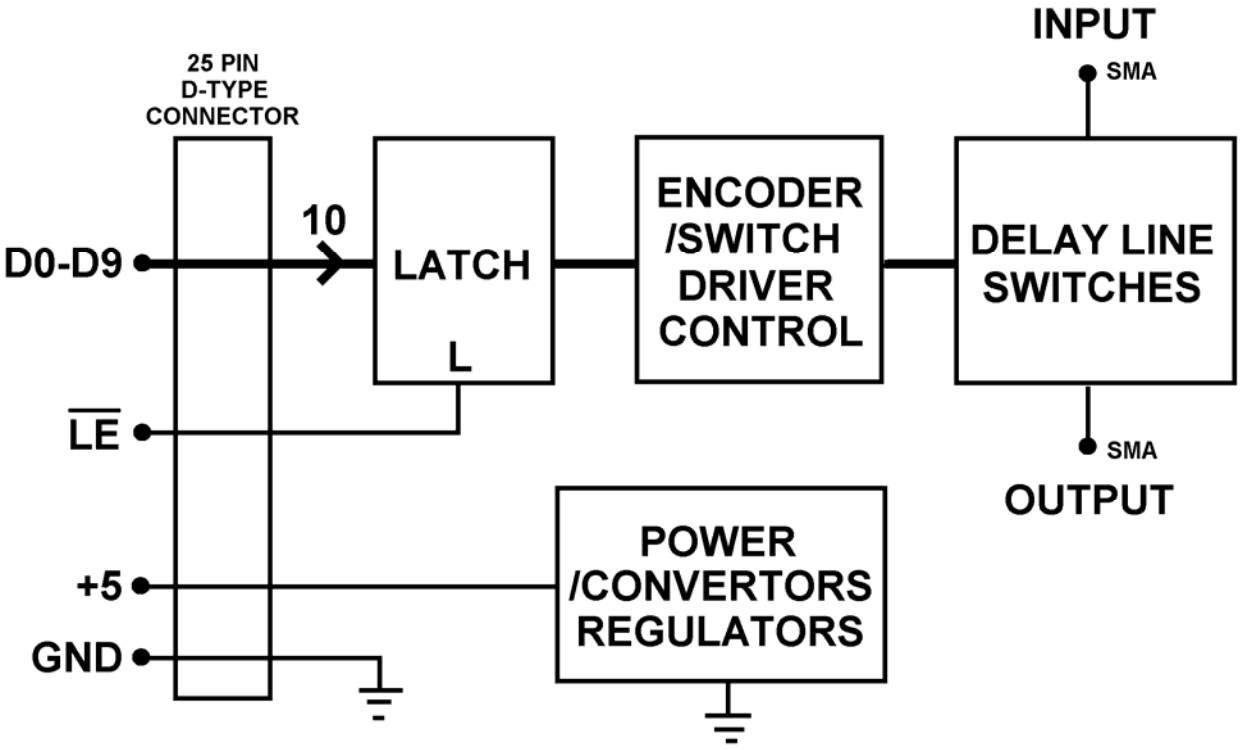

Figure 48 The delay line consists of passive GaAs microwave transfer switches. The switch network series resistance losses are matched with shunt resistance to ground for improved wide-band matching. From Gigabaudics Inc. technical articles.

A Gigabaudics PADL10 programmable delay line is used in our system to adjust microwave phase quickly. The PADL is a programmable delay line instrument designed for adjusting the time delay or phase of radio, microwave or even digital signals with bandwidths from DC to 3 GHz. Delays are controlled via a TTL bus. Compared with those manually operated, hand-cranked line stretchers, this instrument has the advantage of lower mismatch, higher bandwidth and higher range. It employs GaAs passive microwave switched line technology. Lines are switched in series so that each delay occurs additively with any other

switched-in delays. 10 bits digital lines control delay precisely in standard step size of 10, 20, 40, … , 5120 ps, giving a total of 1024 delay steps from 0 ps to 10230 ps.

Fast TTL control logic is used in this instrument for application requires rapid delay changes. Response time is usually in the order of ns which is negligible in our application where switch rates of several kHz are adopted.

The relative insertion loss of PADL between each delay is measured with a Schottky diode detector (Figure 49), which works as a rectifier to convert microwave signal into a DC voltage that is proportional to input power. The transmission ratio is obtained instead of insertion loss.

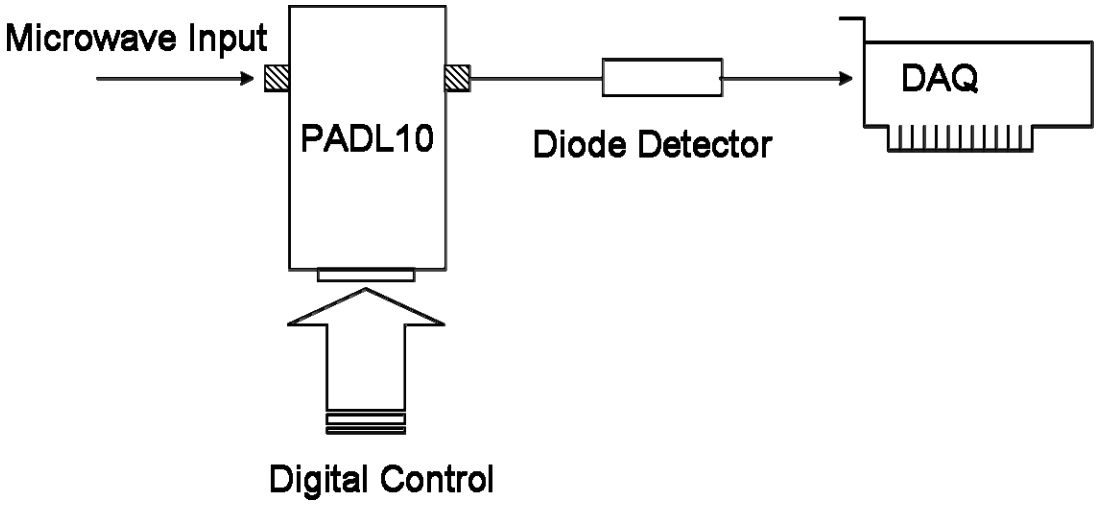

Figure 49 PADL insertion loss calibration

The relative transmission ratio is obtained as show in Figure 50. We then pick up a pair of delays which have small power transmission difference. One of those pairs we choose has less than 0.2% difference and 80 ps delay as indicated in the figure. These two lines are quickly switched in and out by applying corresponding digital signal at 1~2 kHz. In this way, we can get 80 ps phase modulation to the microwave signal while minimizing the power variation.

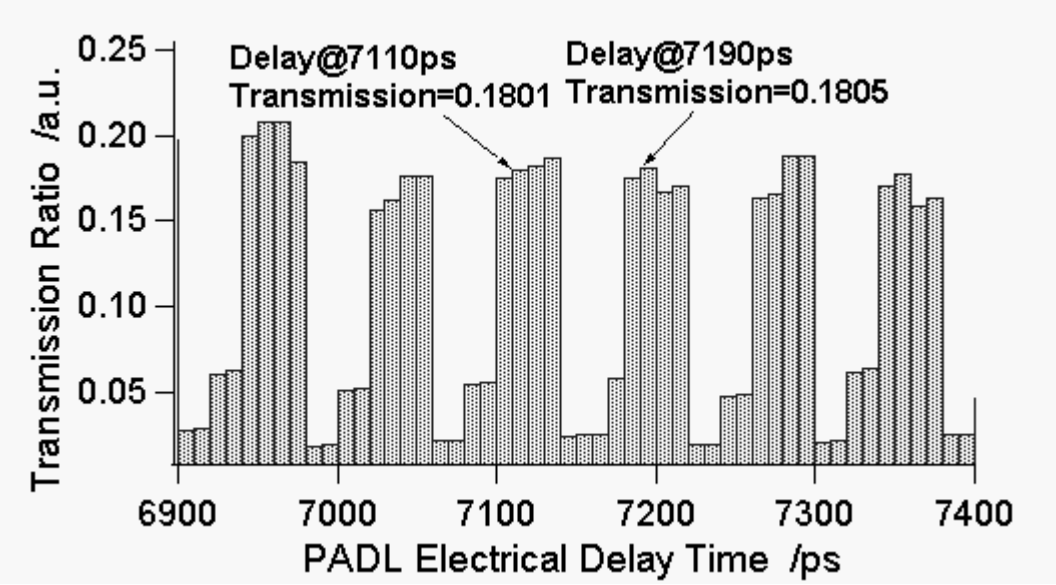

Figure 50 PADL transmission ratio at various delay settings. The PADL switches between two selected delays as marked in the figure.

3.0 $(Ba_{0.5}Sr_{0.5})TiO_3$/MgO LATTICE SCALE DOMAIN DYNAMICS DETECTED WITH PIEZOFORCE MICROSCOPY (PFM)

Ferroelectric domain walls are atomically thin, and consequently their dynamics are sensitive to the periodic potential of the underlying lattice. Despite their central role in domain dynamics, lattice-scale effects have never been directly observed. We investigate local domain dynamics in thin film ferroelectrics using atomic-force microscopy. Upon combined dc and ac electric driving, fluctuations in the local piezoresponse are observed. Fourier analysis of the fluctuations reveals the presence of narrow band and broad band noise, and Barkhausen jumps. The narrow band noise is attributed to dynamics associated with lattice-scale pinning and is reproduced by a simple physical model.

Nearly all of the interesting and useful properties of ferroelectrics can be traced back to the patterns and dynamics of domain walls, the boundaries that separate regions of uniform electric polarization[66]. Unlike magnetic domain walls, whose widths $\xi_M \sim 10-100$ nm are much larger than the lattice constant a, ferroelectric domain walls are atomically thin, with $\xi_E \gtrsim a$. More than fifty years ago, Landauer noted[67] that since the domain wall is comparable in extent to the interatomic spacing (see Figure 51 a), it should be strongly pinned by the lattice itself (also known as the Peierls potential[68]). Domain motion can occur through thermal

activation over the Peierls potential, and an applied electric field E can strongly influence the rate.

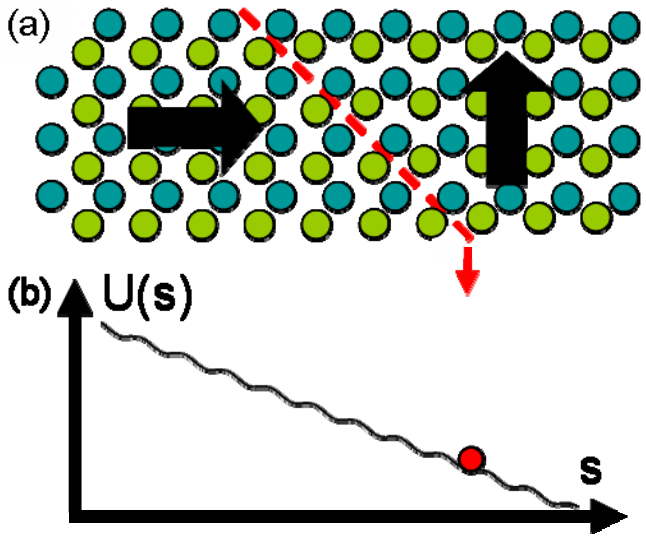

Figure 51 (a) Lattice model of a 90° wall in a ferroelectric. (b) Sketch of energy function for the domain wall coordinate, showing the effects of an external field (overall slope) and atomic-scale periodicity.

When a domain wall is driven externally, the periodic Peierls potential should in principle produce oscillations in the domain wall velocity, similar to "narrow-band noise" in charge-density-wave (CDW) conductors[69] or the ac Josephson effect in superconductors[70]. All three physical systems can be represented abstractly by a single configurational coordinate *s* (i.e., domain wall displacement, CDW or superconducting phase) subject to a global and periodic potential $V(s)$ (Figure 51 b).

Here we report what we believe to be the first direct observation of lattice-scale domain wall dynamics in a ferroelectric thin film. The measurements were conducted with an atomic force microscope (AFM) used not for ferroelectric imaging[71] or poling[72], but rather as a sensitive microphone. The local, noninvasive nature of the measurement, combined with a sample that

exhibits a low barrier for domain motion, has allowed these effects to be observed for the first time.

We concentrate on the mechanical noise associated with domain wall dynamics in ferroelectric thin films. A wide range of velocities for 180º domains have been observed experimentally, ranging from Angstroms per second to centimeters per second[73], and the behavior is in reasonable agreement with phenomenological models that invoke lattice pinning[74]. More recent investigations show that 180º domain dynamics in epitaxial thin films also proceeds *via* thermal activation over the Peierls potential[19]. Clamping by the substrate[75] is known to inhibit strongly the movement of 90º domains in thin films[76]. However, recent experiments have shown empirically that control over oxygen pressure during the growth and annealing of (Ba,Sr)TiO_3 films can reduce the tetragonality, causing the films to become nearly cubic[27]. Two different films were investigated. Both consist of 500 nm thick ($Ba_{0.5}Sr_{0.5}$)TiO_3 films grown by pulsed laser deposition on MgO substrates[28]. One sample was deposited at 50mTorr O_2 pressure, while the second was deposited at 500 mTorr O_2. Optical investigations of films grown under similar conditions indicate that the polarization of both films are primarily out-of-plane oriented, and that applied in-plane electric fields can induce local reorientation of the ferroelectric polarization of the 50mTorr film[77]. Interdigitated electrodes were deposited on top of the films, with a gap spacing between the electrodes $d = 10$ μm. More details about the growth and structural properties are described in Ref. [28].

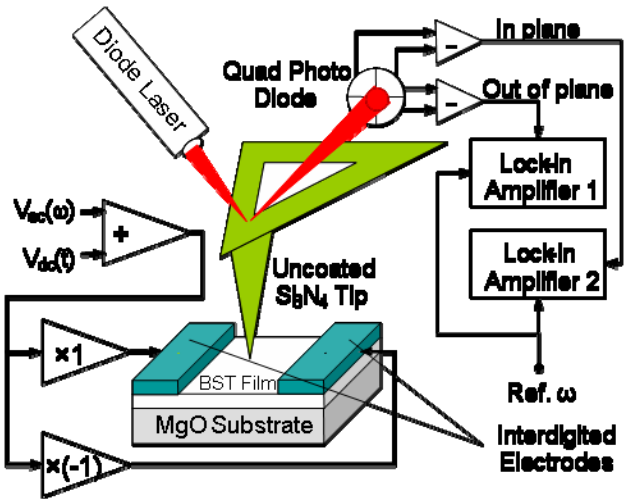

Figure 52 Experiment arrangement

Figure 52 shows a block diagram of the experimental arrangement. A home-built atomic-force microscope (AFM) is used to investigate the in-plane and out-of-plane piezoresponse of the film. A commercially available, insulating sharpened Si_3N_4 tip is used for topographic imaging and local measurements. The film is driven electrically using a balanced pair of voltage signals, so that the potential is always close to ground in the center of the film where the measurements are typically made. The AFM is operated in contact mode, and the vertical displacement of the cantilever is used to provide vertical feedback control. The piezoresponse of the film is measured by applying an in-plane dc+ac electric field $E(t)=E_{dc}+E_{ac}\cos(\omega t)$ and measuring the deflection of the cantilever using a standard optical bridge. The feedback setpoint is chosen to minimize non-piezoelectric (*e.g.*, electrostatic) contributions to the signal. Two lock-in amplifiers detect in-plane and out-of-plane deflections of the tip at the ac driving frequency $\omega/2\pi \sim 30$ kHz.

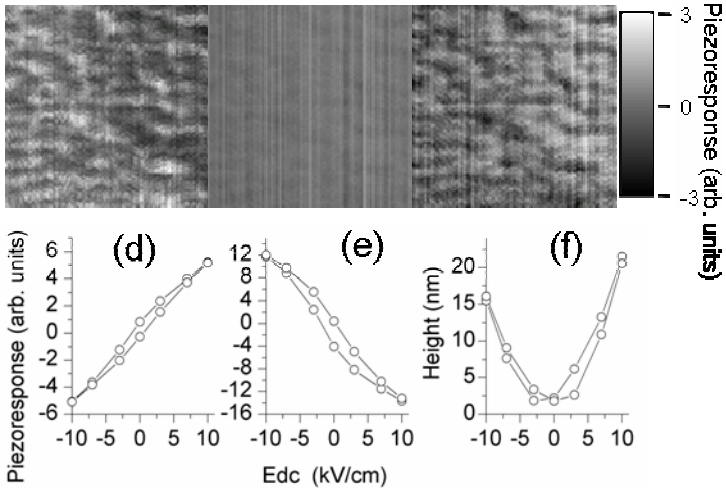

Figure 53 Interleaved piezoresponse images of a $Ba_{0.5}Sr_{0.5}TiO_3$ thin film deposited in oxygen pressure $P(O_2)$=50 mTorr. A total 14 interleaved images are acquired at different dc electric fields E_{dc}, three of which are shown. The mean values of the image have been subtracted for clarity. (a) E_{dc}=-10 kV/cm; (b) E_{dc}= 0 kV/m; (c) E_{dc}= +10 kV/cm; (d) –(f) local hysteresis observed by averaging the interleaved images over a 50 nm x 50 nm area. (d) In-phase piezoresponse. (e) Out-of-phase piezoresponse. (f) Hysteresis in the sample surface height.

Images of the sample topography and piezoresponse are obtained simultaneously by raster-scanning the sample and recording the corresponding vertical height and lock-in signals. To minimize effects associated with thermal drift, several images are scanned in an interleaved fashion[78], using a repeating sequence of dc electric fields (E_{d1}, E_{d2},…, E_{dn}) to acquire successive scan lines. Figure 53 (a-c) show representative images of the out-of-plane piezoresponse for the $P(O_2)$=50 mTorr sample. Without a dc bias (Figure 53 (b)), the response at the driving frequency ω is nearly absent, providing strong evidence that the spontaneous polarization is primarily out-of-plane. Upon application of an in-plane bias field (Figure 53(a,c)), a distinct response is observed. Changes in the piezoresponse are associated with nanopolar reorientation of the ferroelectric polarization from out-of-plane to in-plane.

The local piezoresponse can be obtained from this dataset by averaging over a small area (~50 nm) and plotting the topographic response (Figure 53(f)), in-phase (Figure 53 (d)) and out-of-phase (Figure 53 (e)) piezoresponse as a function of the applied electric field. For the data shown, a total of 14 interleaved images were taken, enough to illustrate the hysteretic response of the film. Changes in the film displacement, shown in Figure 53 (f), are approximately quadratic functions of the applied dc field, showing small but measurable hysteresis. The piezoresponse curves also exhibit hysteresis (Figure 53 (d,e)), indicative of domain motion, and the quadratic response is consistent with a predominantly out-of-plane polarization. The control sample ($P(O_2)$=500 mTorr) shows no hysteresis, and a much weaker field-induced piezoresponse.

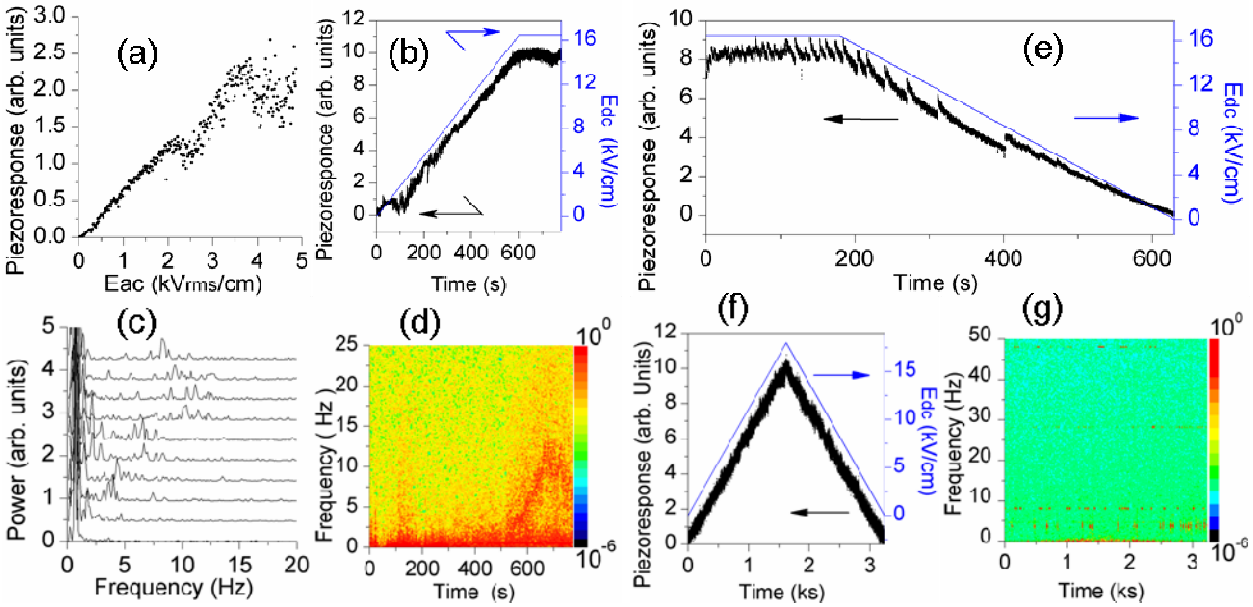

Figure 54 Local noise measurements for $Ba_{0.5}Sr_{0.5}TiO_3$ grown at $P(O_2)$= 50 mTorr. (a) Piezoresponse versus ac amplitude. (b) Piezoresponse and dc bias versus time. (c) Fourier transform of temporal response at ten different times. (d) Intensity graph showing Fourier spectrum versus time. (e) Piezoresponse showing Barkhausen-type noise. (f) Piezoresponse and dc bias versus time for $Ba_{0.5}Sr_{0.5}TiO_3$ grown at $P(O_2)$= 500 mTorr. (g) Intensity graph showing Fourier spectrum versus time for $Ba_{0.5}Sr_{0.5}TiO_3$ grown at $P(O_2)$=500 mTorr.

Investigations of fluctuations or noise in the piezoresponse[79] are obtained by fixing the tip at a single location on the sample, slowly ramping the dc electric field, and digitizing the time-dependent piezoresponse[80]. The qualitative features of the measured piezoresponse depend strongly on the amplitude of the ac driving. Two distinct regimes are observed (see Figure 54 (a)). For low ac driving, the response is linear and rms fluctuations are small. Above a well-defined threshold (~2 kV_{rms}/cm), the response becomes nonlinear and fluctuations increase significantly. For Figure 54 (b), an ac amplitude E_{ac}=1 kV_{rms}/cm was chosen. As the dc field is slowly ramped at a rate (27 V/cm·sec), and is kept constant for $600 \text{ sec} < t < 800 \text{ sec}$, during which a corresponding change in the piezoresponse is observed.

To help analyze the response, a joint time-frequency analysis of the time series is performed, using a sweeping time interval of T=1.024 sec and Hanning windowing[81]. The corresponding power spectra are displayed in a waterfall plot (Figure 54 (c)). There is clear evidence of a well-defined "narrowband" noise over the interval shown, sustained over much of the time interval during which the dc field is held constant. Figure 54 (d) shows an intensity plot of the noise spectra over the full time interval. The narrowband noise is clearly distinguished from lower frequency "broadband noise". Its central frequency appears to be correlated with the applied dc bias, appearing only for bias fields above ~12 kV/cm. The highest center frequency is approximately 15 Hz, which is small compared to the driving frequency ω and large compared to the inverse waiting interval.

Narrowband noise has been observed in a number of locations on the sample, but not everywhere. The observation method is highly local, and noise is therefore expected to be observed only directly above a domain wall that is sufficiently mobile. Repeated experiments do

not always produce the same noise signals, and the reason may be due to thermal drift (as much as 100 nm over the 13 minute measurement interval).

The narrowband noise is distinct from Barkhausen jumps[82], also observed in this sample. Figure 54 (e) shows typical Barkhausen jumps over the time interval 100 sec < t < 300 sec. The jumps are significantly larger in amplitude than the narrowband noise, and no Fourier transform is need to discern them.

For the sample where $P(O_2)$=500 mTorr, similar experiments and analyses were performed. For this sample, no discernable noise of any kind is observed (Figure 54 (f)). That includes narrowband, broadband and Barkhausen noise. Very small intermittent bursts were observed at discrete frequencies; however, this noise appears when the cantilever is withdrawn from the sample surface, and is therefore attributed to instrumental sources (Figure 54 (g)). The absence of narrow-band noise for the control sample helps to rule out a large number of potential sources of artifacts for the observed effect.

The experimental results on the $P(O_2)$=50 mTorr sample are consistent with the interpretation that fluctuations in the piezoresponse are associated with lattice-scale domain dynamics. This sample shows appreciable hysteresis, in contrast to the $P(O_2)$=500 mTorr sample which exhibits no hysteresis and no fluctuations in the piezoresponse. The larger electro-optic response of films grown under conditions of low oxygen pressure is also consistent with this interpretation. The question then arises, what are the physical mechanisms giving rise to the various types of noise observed? Barkhausen jumps are commonly observed in bulk ferroelectrics[82], and it is natural to ascribe the sudden and sometimes regular jumps in the measured piezoresponse to Barkhausen events. The physical mechanism undoubtedly is related to the depinning of domain walls from defect sites in the film, of which there are many. The

other sources of noise, "broadband" and "narrow-band", are more difficult to assign. The presence of both types are strongly reminiscent of behavior observed in sliding charge-density wave conductors[69], which exhibit narrowband and broadband noise associated with the sliding of a periodic charge density over fixed defects in the crystal. For the case of a domain wall in a ferroelectric, the lattice itself forms a periodic potential that can lead to oscillations in the domain wall velocity and in the associated piezoresponse.

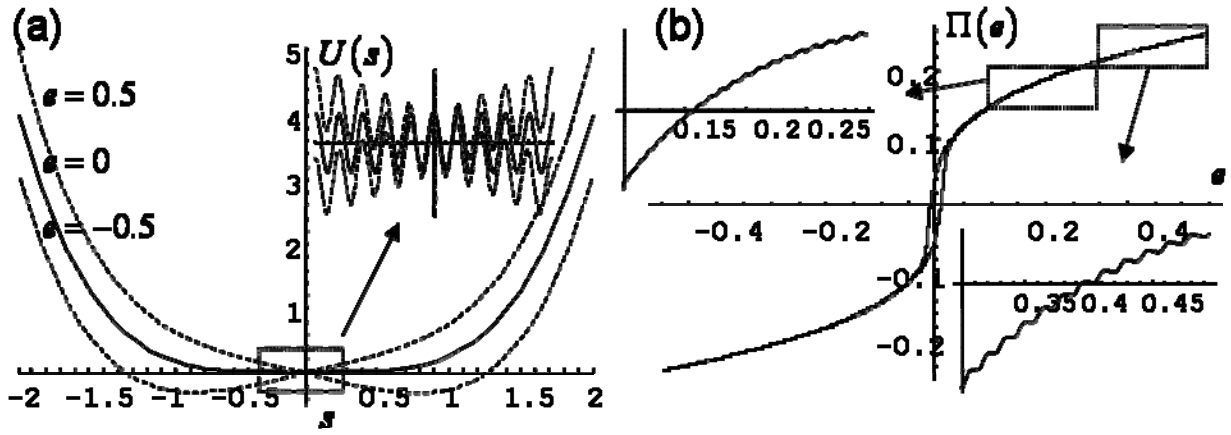

Figure 55 One-dimensional model of ferroelectric domain wall to explain the origin of narrow band noise. (a) Solid curve represents Peierls potential at zero dc bias. Dashed curves represent the tilted potential when an external electric field is applied. The inset shows a close-up of the potential near $s = 0$. (b) Calculated piezoresponse as a function of dc bias, showing narrow band noise associated with lattice-scale domain wall dynamics

Here we propose a simple model to describe a physical mechanism for the narrowband noise. The dynamics of the domain wall coordinate s is presumed to be governed by a one-dimensional potential: $U(s) = as^4 + (h/k)\cos(ks) - es$. The quartic term provides global confinement of the wall, and is intended to model long-range effects of strain that is built up by the translation of 90º walls. The periodic lattice-scale Peierls potential is parameterized by a strength h and wave number k. An applied electric field e couples directly to the domain wall coordinate. Figure 55 (a) displays a plot of $U(s)$ for three values of e. Domain wall dynamics

are assumed to be overdamped, with a velocity given by $\dot{s} = -\nabla U(s)$. When a dc bias is applied, the potential is tilted, resulting in a displacement of the domain wall within the atomic-scale potential[83]. If the combined dc+ac field is large enough, the time-averaged Peierls barrier is lowered sufficiently to allow domain wall oscillation. The resulting piezoresponse is calculated by numerically simulating the domain dynamics and measuring the extent of domain motion as a function of the dc electric field, as shown in Figure 55 (b). A close-up of the piezoresponse at large dc bias shows oscillations in the piezoresponse. Further analysis reveals that these oscillations correspond to domain wall amplitudes that alternate between *n* and *n*+1 Peierls periods. That is, this model exhibits behavior that agrees qualitatively with the experimental results shown in Figure 54.

This simple model cannot explain the more complicated responses of the real physical system, such as broadband or Barkhausen noise. However, it does capture several important features of the experimental data, including the existence of narrowband noise, and its dependence on the driving amplitude. Further experimental investigations of this effect in uniaxial films (with 180 degree walls) are underway.

4.0 ELECTROOPTICAL MEASUREMENT OF THIN FILM SrTiO3/DyScO3 USING CONFOCAL SCANNING OPTICAL MICROSCOPY (CSOM) MEASUREMENT

Strained $SrTiO_3$ grown epitaxially on bulk $DyScO_3$ substrates exhibit room-temperature ferroelectricity and associated remarkable properties such as sharp field-dependent microwave permittivity. Electro-optic measurements provide complementary insight into the properties and help explain the behavior of ferroelectric $SrTiO_3$ at room temperature. The electro-optic response is measured as a function of light polarization and applied in-plane bias magnitude and direction. Hysteresis is observed at room temperature, indicative of ferroelectricity. Optical images shows uniformity of films. However, the effective electro-optic coefficients are bias-field dependent. A simple model incorporating non-180° domains can account for most of the experimental observations.

Bulk $SrTiO_3$ is not ferroelectric, even at absolute zero temperature. The absence of a true phase transition has been attributed to quantum fluctuations of the soft phonon mode; for this reason $SrTiO_3$ is often referred to as a "quantum paraelectric"[25]. The low-temperature state, while non-ferroelectric, is nevertheless highly sensitive to dopants or strain[84,85,86].

Recent advances in thin-film fabrication and substrate engineering have resulted in thin films of $SrTiO_3$ with ferroelectric phase transitions near room temperature[26]. These films are grown on the [110] plane of $DyScO_3$, which is pseudo-cubic with a lattice constant that is 0.8% larger than that of $SrTiO_3$ [26]. This lattice mismatch generates uniform in-plane strain and causes

orthorhombic structural distortion, resulting in ferroelectricity with an in–plane easy axis[87]. Sharp dielectric tuning curves at microwave frequencies are observed with an in-plane dielectric constant as high as 7000 at 10 GHz, dropping by a factor of 5 under modest electric fields (~70 kV/cm). The "frequency-agile" properties of these materials are promising for tunable microwave devices.

The optical properties of bulk and thin film $SrTiO_3$ have been studied extensively[88, 89, 90, 91, 92,93]. Optical probes can help relate structural and dielectric properties, and can be used to map polarization dynamics on GHz—THz frequency scales[94,95,96,97]. Information obtained from electro-optic studies can be used to determine the polar response to applied fields, and may find use in applications involving integrated waveguides or other optical devices.

Our measurements on $SrTiO_3/DyScO_3$ reveal a strong field-dependent electro-optic response. The effective electro-optic coefficients are field tunable, similar to the manner in which the microwave-frequency dielectric constant is tunable. We have also detected hysteresis in the electro-optic coefficients which is associated with room-temperature ferroelectricity. Such hysteresis has not been observed by conventional remnant polarization measurements[98]. We attribute the field dependence to the co-existence of nanoscale multi-domains too small to resolve using diffraction-limited optical techniques.

Confocal scanning optical microscopy [42] (CSOM) is used to measure the local birefringence and electro-optic effect of a 25 nm-thick $SrTiO_3$ film grown on $DyScO_3$ (Figure 56). Linearly polarized light from a laser source (Mira 900, λ=820 nm, power =10 mW) is first spatially filtered by a pinhole and a collimator, and then converted into circularly polarized light using a quarter-wave plate. Linearly polarized light of an arbitrary orientation is produced with a second polarizer placed after the quarter-wave plate, mounted on a computer-controlled rotation

stage. A beam splitter is placed between the pinhole and microscope objective. One beam is directed to a microscope objective (40×, NA 0.65) and focused on the sample surface. Light reflected from sample surface is collected by the same objective and its intensity I_r is measured with the signal channel of the balanced photodetector; the other beam is directed to the reference channel.

Ferroelectrics are in general birefringent materials with strong electro-optic effects. To observe the electro-optic response, in-plane electric fields are applied to the sample using interdigitated electrodes. Both ac and dc voltages are applied in order to map out the full field-dependent response. In order to measure orientation-dependent effects, the electrodes are oriented at several angles with respect to the crystallographic axis. An applied ac electric field will produce a corresponding modulation of the birefringence and the overall refractive index. The refractive index change is related to the linear electro-optic coefficient, which is a third-rank tensor. The index change also depends on the light polarization and electric field angle. The field-induced reflectivity change is detected optically and isolated using a lock-in amplifier at the frequency of ac driving field. To minimize the noise due to laser power fluctuations and inhomogeneous surface reflectance, the lock-in output signal is normalized by the reflected light intensity I_r, to give $\Delta I_r / I_r$.

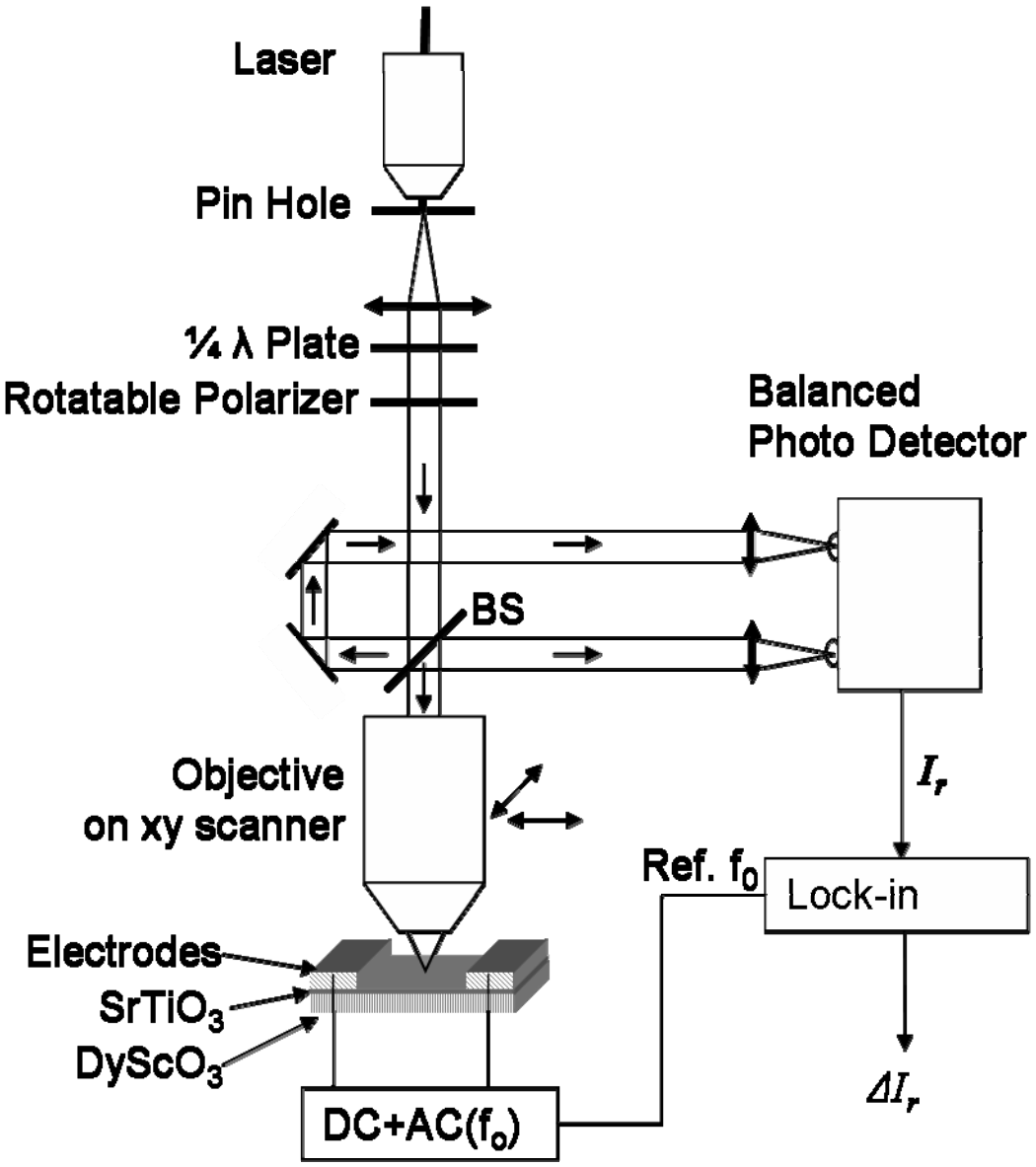

Figure 56. Confocal scanning optical microscopy setup for electro-optic measurements of $SrTiO_3/DyScO_3$.

The ac frequency is set to ~80 kHz, higher than most of the laser noise but within the bandwidth of the optical bridge. The electrodes are deposited at several angles (90°, 120°, 135°, 150°, 180°), as shown in Figure 57. The gap between electrodes d = 6 μm. The objective is mounted on a *xyz* stage which has both coarse (μm-sensitivity) and fine (nm-sensitivity) control over all three axes. The *xy* fine control scanning range is 15 μm ×15 μm. Reflectivity images are used as a guide to position the focused beam which is centered between the two interdigitated

electrodes. For these experiments the beam position is not scanned. The detected electro-optic signal is recorded as a function of light polarization, dc bias field and field angle.

Using the normal incident approximation, the reflectance *r* can be derived from Fresnel relation $r = (n-1)^2/(n+1)^2$, and the lock-in signal can be just expressed as its derivative with respect to electric field dr/dE. The normalized reflectance change can be expressed as

$$\frac{1}{r}\frac{dr}{dE} = \frac{4}{n^2-1}\frac{dn}{dE} \tag{36}$$

$$\eta_{eff} = \frac{d(\frac{1}{n^2})}{dE} = \frac{-\frac{2}{n^3}dn}{dE} = -(\frac{dr}{r})\frac{n^2-1}{2n^3}\frac{1}{dE} \tag{37}$$

For $SrTiO_3$, the published value $n = 2.34,$ was used, which is an average of n_o and n_e[99]. The electric field amplitude $dE=E_{ac}$ is calculated using $E_{ac}=V_{ac}/d$, and $\frac{dr}{r} = \frac{\Delta I_r}{I_r}$. Because of the equivalence between 180° light polarizations, the data is fitted to a general function

$$f(\theta) = a + b\sin(2\theta) + c\cos(2\theta) + ... \tag{38}$$

Higher order terms such as sin(4θ) and sin(6θ) are neglected because they are small and unrelated to the linear electro-optical effect, as will be explained below.

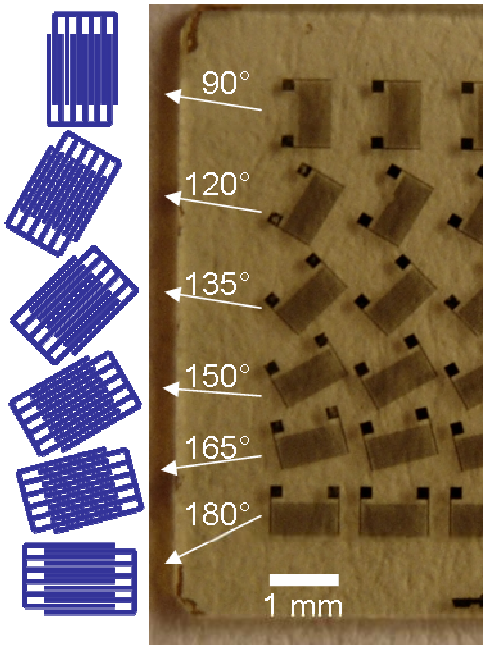

Figure 57. Top view of $SrTiO_3/DyScO_3$ sample with interdigitated electrodes. Six different orientations are available, and five of them were used**.**

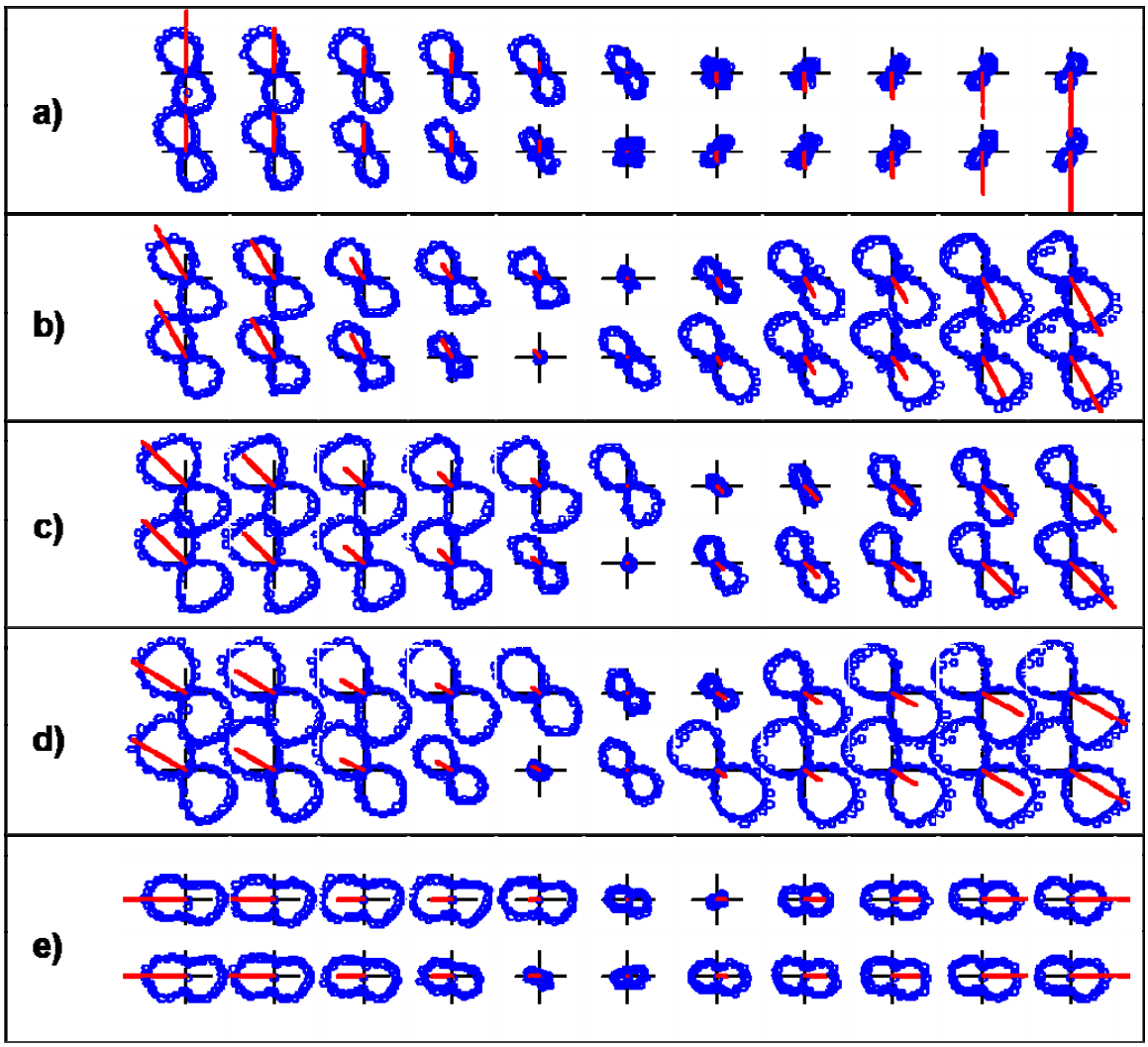

Figure 58. Electro-optic response versus light polarization plotted as a polar graph. 0° is chosen to be along the vertical axis, with angles increasing in the clockwise direction. Open dots are experimental data. Blue solid lines are fitted according to Eq. (38). Red bars represent the electric field strength and direction. The electric field angles are (a) 180° (or equivalently 0°), (b) 150°, (c) 135°, (d) 120°, (e) 90°. In each sub-figure, data was acquired starting from the top left and proceeding clockwise. The bias voltages are (in volts) -10, -7, -4, -3, -1.5, 0, +1.5, +3, +4, +7, +10, +10, +7, +4, +3, +1.5, 0, -1.5, -3, -4, -7, -10.

The normalized reflectivity $\frac{1}{r}\frac{dr}{dE}$, proportional to the electro-optic response, is plotted versus linear polarization angle for various values of the static electric field E_{dc}, shown in Figure 58. In each sub-plot, the magnitude and direction of the red line represents the magnitude and

direction of the applied electric field. Data was collected at a fixed polarization angle for 22 different voltages, and 36 different linear polarization angles.

The two-lobe and four-lobe angular distributions present in Figure 58 are signatures of birefringence. The crystal structure of bulk $SrTiO_3$ is central-symmetric with no birefringence or linear electro-optic effect. The existence of a linear electro-optic effect demonstrates that this symmetry is broken by the constraints imposed by the $DyScO_3$ substrate.

Both the magnitude and angular distribution of the electro-optic response depend sensitively on the strength and angle of the bias electric field. For a given field direction, the lobe orientation is not always constant, as can be seen in Figure 58 (a, e). The effective linear electro-optic coefficients are derived from fits to Eq. (37) and Eq. (38). In Figure 59, the coefficients in Eq. (38) are plotted versus light polarization and electric field strength. The coefficients show clear hysteresis that is attributed to remnant polarization.

From Figure 59, it is clear that the linear electro-optic response saturates above a critical field strength. To understand this phenomena, we calculate the linear electro-optic response based on a crystal with mm2 point group symmetry[87], using field strengths comparable to the experimental conditions. We find that the field-dependence of the observed electro-optic response cannot be described with a single-domain model. A single domain can only exhibit abrupt changes in electro-optic response due to uniform domain reversal. The model we consider allows for four different types of domains in the directions of 0°/180° and +/-90° to the possible symmetry axis. This symmetry axis is chosen to be in the direction of 135° of our coordinate systems according to the first principle density-functional calculation done by A. Antons *et. al*[87] Therefore the direction of chosen domains in our coordinate systems are +135°, -45°, +225°, +45°. We label the relative fractions of those types of domains as $f_1 f_2 f_3$ and f_4, with

the normalization constrain $f_1+f_2+f_3+f_4=1$. The co-existence of 90° domains is consistent with the fact that the measured *a* and *c* lattice constants are so close to each other. Landau free-energy simulations by Li *et a*[100]. also predict the coexistence of 180° and 90° domains[100]. The ratio between 90° domains is fixed because we assume that there is no 90° domain reorientation. In addition to 90° difference, we also assume there are anti-parallel ferroelectric domains. The ratio between anti-parallel domains depends on the applied electric field. The resulting electro-optic response is plotted in Figure 60-Figure 62 in a fashion similar to Figure 59. Details of the calculation are given in the Appendix below.

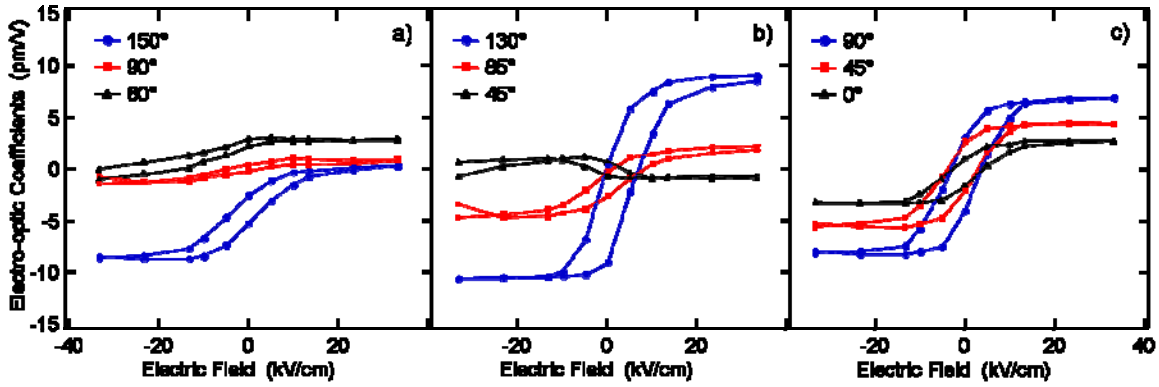

Figure 59. Effective linear electro-optic coefficients versus bias electric field strength at different light polarization and electric field angle. a) Electric field at 180°. b) Electric field at 135°. c) Electric field at 90°. The legends indicate light polarization. Eq. (37) is used to calculate the coefficients.

4.1 COMPARISON BETWEEN THEORY AND EXPERIMENT

For all simulations, we set E=20 V /(6 μm), dE=2 V/(6 μm), and one of the principal optical axes is chosen to be along 135° to the vertical axis[87,100]. Domains parallel and anti-parallel to this direction are referred to as 0° and 180° domains, respectively. A second principal

axis is chosen to be along 45°, and domains parallel and anti-parallel to this direction are referred to as +90° and -90° domains. Several relevant elements in the electro-optic tensor are chosen to be r_{13}=20, r_{33}=2, r_{51}=10. The dielectric impermeability is set to $(1/n_x^2)$=0.17 and $(1/n_z^2)$=0.16; n_x, n_z are chosen to be close to each other because the effective birefringence for thin films is small.

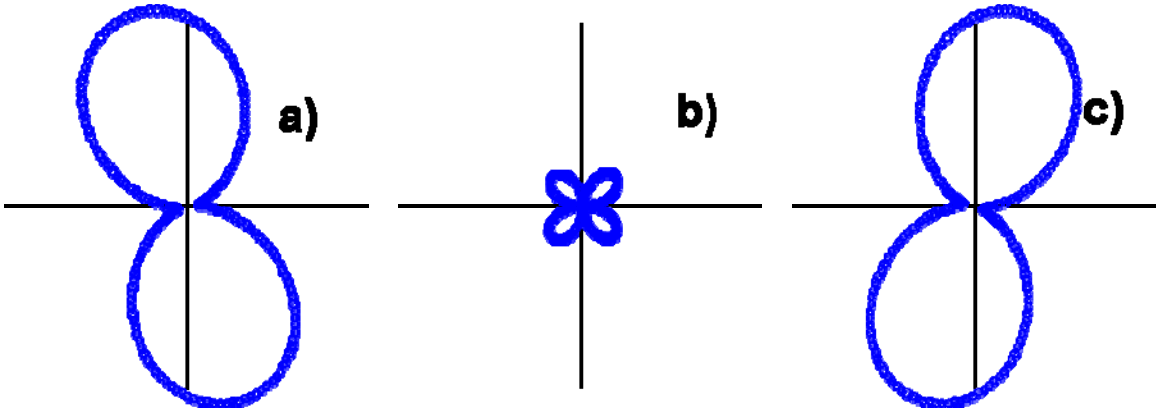

Figure 60. Simulated electro-optic responses for 180° (or 0°) electric field angle at different between 0°,180°, +90° and -90° domains. The fractions of domains oriented at 0°, 180°, +90° and -90° domains (f_1, f_2, f_3, f_4) are given by a) (0.2, 0.3, 0.5, 0), b) (0.35, 0.15, 0.35, 0.15), c) (1, 0, 0.2, 0.3).

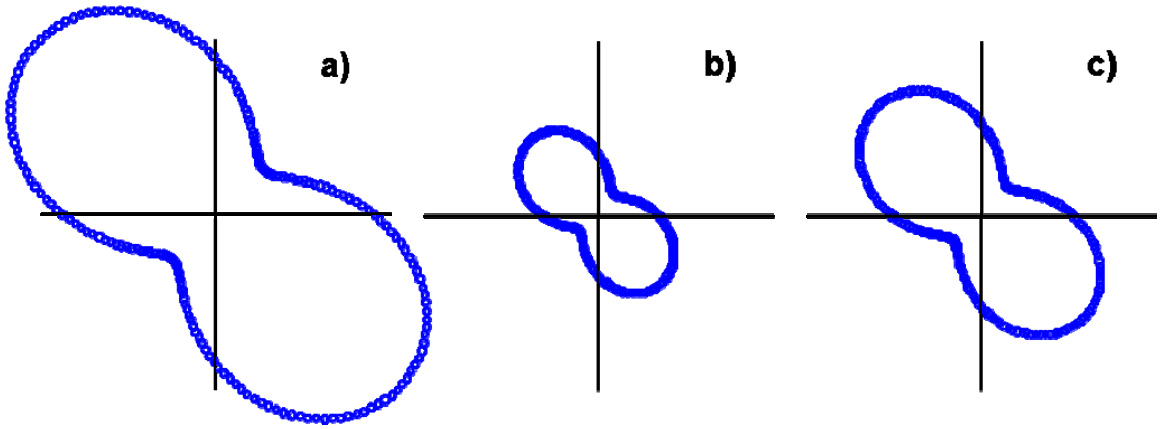

Figure 61. Simulated electro-optic responses for 135° electric field at different 0°,180°, +90° and -90° domains. The fractions of domains are given by (a) (0, 0.65, 0.175, 0.175), (b) (0.195, 0.455, 0.175, 0.175), c) (0.52, 0.13, 0.175, 0.175).

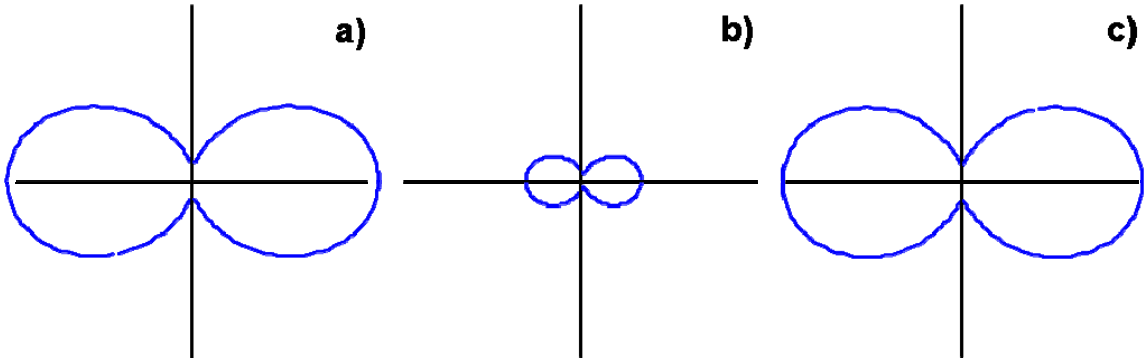

Figure 62. Simulated electro-optic responses for 180° electric field at different ratio between 0°,180°, +90° and -90° domains. The fractions of domains are given by a) (0.4, 0.1, 0.4, 0.1), b) (0.3, 0.2, 0.3, 0.2), c) (0.1, 0.4, 0.1, 0.4)

From these simulations, we find that the contribution of anti-parallel domains cancel out in the electro-optic response. In Figure 61, the electric field is 135°, which is perpendicular to the principal axis (or the polar axis of ferroelectric domain) for the +90° and -90° domains and parallel to 0° and 180° domains. The +90° and -90° domains are fixed at 50/50. In that case their total contribution turns out to be zero. The lobe shape and orientation do not change with the ratio between 0° and 180°—only the amplitude changes (as in Figure 59 c)). When the ratio between 0° and 180° domains saturates at high bias fields, all the domains (except +90° and -90° domains) contribute constructively to the electro-optic effect, consistent with experiment. In Figure 60, the electric field direction lies in between the 0° and 90° domains. All four polar domain orientations contribute equally (if one neglects the small difference between lattice constants). By combining them with various weights one can generate the various lobe shapes and orientations seen in Figure 59(a). However, the relation between the applied field, its history, and the domain fractions is complex and underdetermined by our electro-optic measurements. In Figure 62, the domains are in similar condition as in Figure 60, but the electric

field component in 90° domains are reversed compared with Figure 60. Again, the fraction is chosen to match observations shown in Figure 59(e).

4.2 SUMMARY

The $SrTiO_3$ films grown on $DyScO_3$ substrates appear spatially uniform under the optical microscope. However, as indicated from previous work, there is strong evidence that ferroelectric nanodomains exist[30,77,97], making it difficult to observe the domain structure using diffraction-limited optics. In this work, we developed a multi-domain model for the polarization to explain the experiment results. Calculations of the effective electro-optic coefficients, based on this model, agree qualitatively with experimental observations. Higher-resolution probes such as apertureless near-field scanning optical microscopy[97] are required to give more direct evidence for the existence of nanodomains. We thank Prof. Venkatraman Goplan for several valuable discussions and comments.

4.3 CALCULATE OF ELECTRO-OPTIC EFFECT OF STRAINED $SRTIO_3$

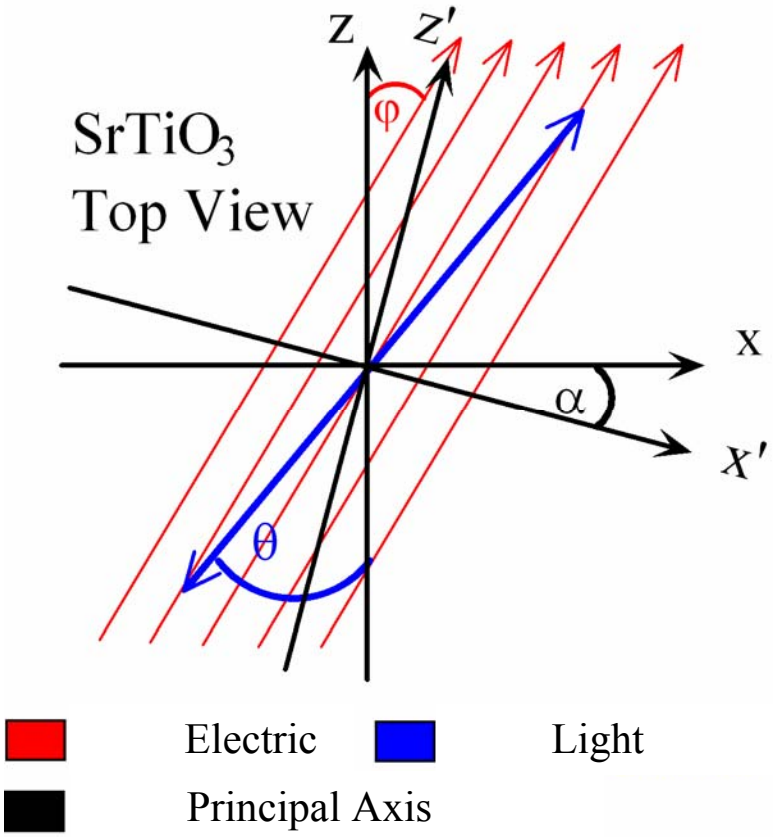

Figure 63. Definition of various angles. X and Z define the original principal axis of refractive index tensor. φ is the electric field angle to Z. X' and Z' is the new principal axis of refractive index tensor under external field. α is the angle of the rotation of principal axis.

The lattice structure of Bulk $SrTiO_3$ is centro-symmetric. The substrate produces tensile strain, causing the lattice structure to become orthorhombic. The relevant form of Pockels tensor (linear electro-optic coefficient) is given by[15,87],

$$r_{ij} = \begin{pmatrix} 0 & 0 & r_{13} \\ 0 & 0 & r_{23} \\ 0 & 0 & r_{33} \\ 0 & r_{42} & 0 \\ r_{51} & 0 & 0 \\ 0 & 0 & 0 \end{pmatrix} \tag{39}$$

The electric field angle φ and light polarization θ is defined with respect to the z axis in the coordinate system along original (zero electric field) crystal principal axis. In the absence of external electric fields, the impermeability tensor can be diagonalized

$$\frac{1}{n^2} = \eta = \begin{pmatrix} \eta_{11} & 0 & 0 \\ 0 & \eta_{22} & 0 \\ 0 & 0 & \eta_{33} \end{pmatrix} \tag{40}$$

Under external electric field applied in the *xz* plane, of which the y component is zero, the new impermeability tensor is given by

$$\frac{1}{n^2} = \eta = \begin{pmatrix} \eta_{11} + r_{13}E_z & 0 & r_{51}E_x \\ 0 & \eta_{22} + r_{23}E_z & 0 \\ r_{51}E_x & 0 & \eta_{33} + r_{33}E_z \end{pmatrix} \tag{41}$$

The new eigen values of above matrix is

$$\left(\frac{1}{n^2}\right)_{11} = \frac{1}{2}[\eta_{11} + r_{13}E_z + \eta_{33} + r_{33}E_z - \sqrt{(\eta_{11} + r_{13}E_z - \eta_{33} - r_{33}E_z)^2 - 4(r_{51}E_x)^2}\,] \tag{42}$$

$$\left(\frac{1}{n^2}\right)_{22} = \eta_{22} + r_{23}E_z \tag{43}$$

$$\left(\frac{1}{n^2}\right)_{11} = \frac{1}{2}[\eta_{11} + r_{13}E_z + \eta_{33} + r_{33}E_z + \sqrt{(\eta_{11} + r_{13}E_z - \eta_{33} - r_{33}E_z)^2 - 4(r_{51}E_x)^2}\,] \tag{44}$$

And the corresponding electric field vectors of eigen light polarization is,

$$\left\{1, 0, \frac{2r_{51}E_x}{\eta_{11} + r_{13}E_z - \eta_{33} - r_{33}E_z + \sqrt{(\eta_{11} + r_{13}E_z - \eta_{33} - r_{33}E_z)^2 - 4(r_{51}E_x)^2}}\right\} \tag{45}$$

$$\{0, 1, 0\} \tag{46}$$

$$\left\{1, 0, \frac{2r_{51}E_x}{\eta_{11} + r_{13}E_z - \eta_{33} - r_{33}E_z - \sqrt{(\eta_{11} + r_{13}E_z - \eta_{33} - r_{33}E_z)^2 - 4(r_{51}E_x)^2}}\right\} \tag{47}$$

Where $E_z = E\cos\varphi$ and $E_x = E\sin\varphi$.

The angle of rotation of principal axis is

$$\alpha = \arctan\left\{\frac{2r_{51}E_x}{\eta_{11}+r_{13}E_z-\eta_{33}-r_{33}E_z-\sqrt{(\eta_{11}+r_{13}E_z-\eta_{33}-r_{33}E_z)^2-4(r_{51}E_x)^2}}\right\} \tag{48}$$

What we measured in experiment is the variation of reflection form sample surface. The reflection ratio is

$$r'_x = \left(\frac{n'_x-1}{n'_x+1}\right)^2, r'_z = \left(\frac{n'_z-1}{n'_z+1}\right)^2 \tag{49}$$

Where n'_x and n'_z are the two principal refractive indices in the rotated principal coordinates, and

$$n'_x = \left(\left(\frac{1}{n}\right)^2_{11}\right)^{-1/2}, n'_z = \left(\left(\frac{1}{n}\right)^2_{33}\right)^{-1/2} \tag{50}$$

For arbitrary light polarization θ, relative to z axis, the reflection ratio is

$$r(\theta,E) = r'_x \sin^2(\theta-\alpha) + r'_z \cos^2(\theta-\alpha) \tag{51}$$

This is indeed the form of Eq. (38)

The lock-in detected value, after normalization, is

$$\frac{dI_r}{I_r} = \frac{dr}{r} = \frac{r(\theta,E+dE)-r(\theta,E)}{r(\theta,E)} \tag{52}$$

5.0 GHz APERTURELESS NEAR FIELD SCANNING OPTICAL MICROSCOPY OF THIN FILM FERROELECTRICS

Ferroelectric materials appear poised to make profound contributions in the areas of nanoelectronics and information technology[16,101,102]. Ferroelectrics possess a unique combination of desirable properties—non-volatile states useful for storing information, strong coupling to electric and optical fields, piezoelectric effects, and compatibility with many semiconductors, including silicon[103,104, 103]. Ferroelectric domains switch at speeds that rival or exceed current non-volatile memories (i.e., flash), and possess superparaelectric limits that are far smaller than their ferromagnetic counterparts. Ferroelectric thin films can be used to create active microwave elements for communications, radar, and other related applications, as well as optical modulators[105] and electrooptic frequency shifters[106].

Still, there are many materials problems to be addressed before ferroelectrics become mainstream components in advanced electronics technology. Nagging issues such as imprint and retention[101,106-111, 107, 108, 109, 110] still limit the rapid development of non-volatile ferroelectric memories. Many limitations on the performance of ferroelectrics at microwave frequencies are better understood, but not at a fundamental level. Critical factors related to the ultimate performance limitations of ferroelectrics as a function of reduced dimensions—important for forecasting the window of competitiveness of ferroelectrics versus rival technologies—are still largely unknown.

Many of the phenomena that ferroelectric materials exhibit occur at scales that are small compared to the wavelength of light. Over the last two decades, several forms of near-field scanning optical microscopy have been developed[39,112-115, 112,113], allowing the diffraction limit to be surpassed. Using apertureless near-field scanning optical microscope (ANSOM), static images of ferroelectric domains have been detected with 30 Å spatial resolution, well below the diffraction limit[39,115] (see Figure 1c). The method, based on an approach pioneered by Wickramasinghe[53,116], is sensitive to both the magnitude and phase of the scattered electric field, and presents unique opportunities when combined with time-resolved optical sources.

We have developed a novel GHz-frequency ANSOM (GHz-ANSOM) that combines the spatial resolution of Atomic Force Microscopy (AFM) with the time resolution inherent in ultrafast optical sources. It is to our knowledge the first time-resolved ANSOM to be demonstrated for any physical system. The working principle of GHz-ANSOM is shown in Figure 64. A mode-locked Ti:Sapphire laser (Coherent Mira 900) generates laser pulses with pulse width ~120 fs at repetition rate $\omega_1 / 2\pi = 76$ MHz. After passing through a spatial filter, the light is focused with a 40X microscope objective onto the end of a platinum-coated AFM tip. The transparent ferroelectric film and substrate are placed between the objective and tip, and the AFM operates in non-contact mode (resonant frequency f_1=280 kHz).

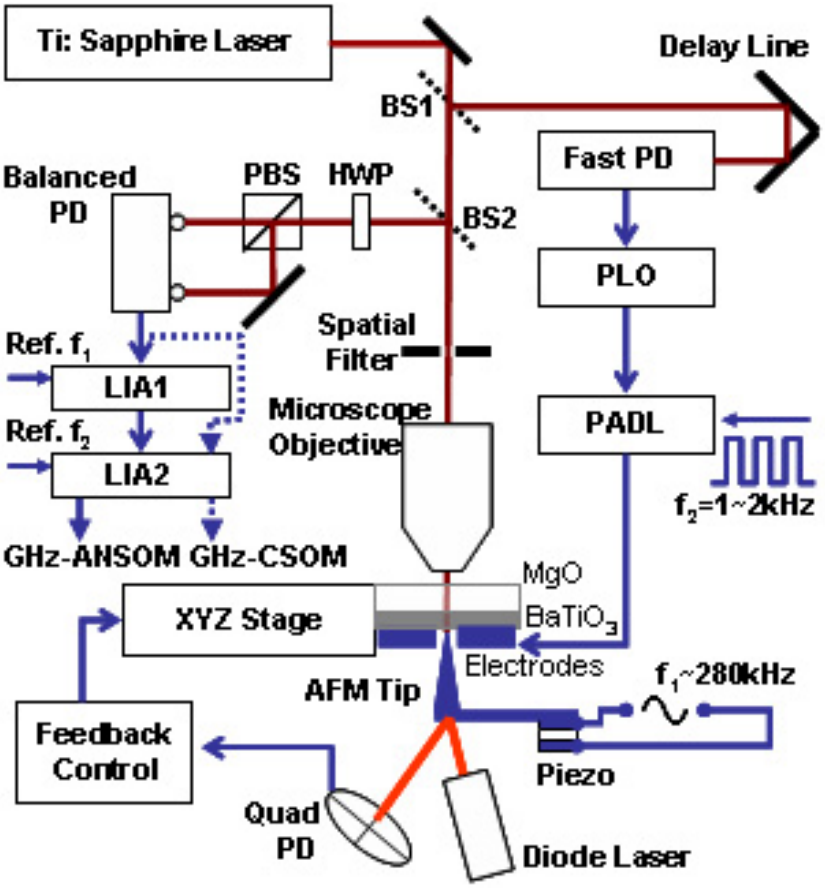

Figure 64. GHz-ANSOM Experiment Schematic. BS1: Beam Sampler. BS2: Non-polarized beam splitter. HWP: Half Wave Plate. PBS: Polarized beam splitter. Balanced PD: Nirvana 2007 balanced photodetector. LIA1: RF Lock-in amplifier. LIA2: Lock-in Amplifier. PD: 1 GHz bandwidth photodetector. PLO: Phase-locked oscillator. PADL: Programmable analog delay line.

The intensity and polarization of light scattered at the AFM probe depends on the complex refractive index tensor of both tip and sample, and depends nonlinearly on the tip-sample separation[117]. The relative intensity of the scattered light with two orthogonal polarizations (electro-optic configuration) is detected by an autobalancing photoreceiver (New Focus Nirvana 2007). To achieve greater sensitivity to scattered light at the very end of the probe, detection at twice the cantilever oscillation frequency $2f_1$ is performed[57].

Experiments are performed on a 500 nm thick $Ba_{0.5}Sr_{0.5}TiO_3$ film grown on MgO by pulsed-laser deposition[118]. The MgO substrate was first thinned to 110 μm, and then optically polished so that light could be transmitted and collected through the substrate.

The ferroelectric thin film is driven by in-plane microwave electric fields (amplitude ~3 Vrms), applied across the gap of two interdigitated electrodes (separation d=10 μm). Picosecond time resolution is achieved by driving the sample with a microwave phase-locked oscillator (PLO), similar to that used for time-resolved confocal scanning optical microscopy experiments[119]. The PLO generates microwaves at integer multiples of the laser repetition rate $\omega_n \equiv n\omega_1$, where n=26, 27,…,52. Rather than modulating the laser or microwave intensity (which affects the feedback), the phase of the microwave probe is modulated digitally at f_2=1-2 kHz using a programmable analog delay line (Gigabaudics PADL-10). The PADL periodically swaps in and out a fixed length of cable ($\Delta\tau$=80 ps), while having a negligible impact on the microwave amplitude (< 0.2%) or the feedback.

A double-modulation scheme involving two lock-in amplifiers (LIA1=SR844 RF lock-in, LIA2=EGG5210 lock-in), connected in cascade fashion, produces the GHz-ANSOM signal $\Delta\eta(t)$, where t is the delay between the microwave source and optical probe. It should also be noted that the GHz-CSOM signal $C(t)$ can also acquired simultaneously via lock-in detection at f_2.

The observed electrooptic response at a given location on the ferroelectric film under periodic driving is also periodic, and can be described by the following functional form: $\eta(t) = \eta_0 + A_1\cos(\omega_n t + \phi_1) + A_2\cos(2\omega_n t + \phi_2) + \ldots$, where t is the relative time delay between laser pulse and microwave controlled by optical delay line. Higher order harmonic responses are small and are neglected in the analysis that appears below. The fundamental response

(parameterized by A_1 and ϕ_1) corresponds to the linear electrooptic behavior due to in-plane ferroelectric polarization, while the second-harmonic response (parameterized by A_2 and ϕ_2) results from a quadratic electrooptic effect and is sensitive primarily to out-of-plane ferroelectric polarization[77]. In our experiment, we use phase modulation and lock-in detection to compare the electrooptic response at two discrete time delays; hence the GHz-ANSOM signal is proportional to the difference

$$\Delta\eta(t) = \eta(t+\Delta t) - \eta(t) = A_1 \cos(\omega_n t + \phi_1 + \Delta t/2)\sin(\omega_n \Delta t/2) \tag{53}$$

Thus, the phase modulation shifts the electrooptic response by a time $\Delta t/2$ and rescales it by a factor $\sin(\omega_n \Delta t/2)$.

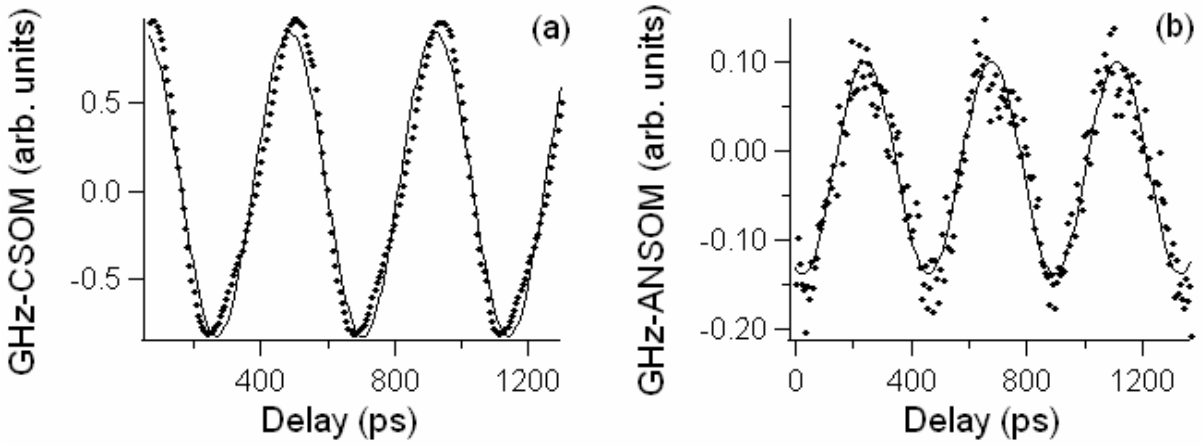

Figure 65. GHz-CSOM (a) and GHz- ANSOM (b) signal at different optical delays. The optical probe and/or AFM probe are fixed at one location on the sample during this experiment. Microwave frequency is 2.28 GHz for both cases. Solid lines are fitted to a sinusoidal function.

The two curves in **Figure 65** show typical time-resolved responses at a single location on the $(Ba,Sr)TiO_3$ thin film examined here. The microwave driving frequency for this experiment was

$\omega_n / 2\pi = 2.28$ GHz, corresponding to n=30. In **Figure 65**(a), GHz-CSOM is shown for purpose of comparison. The GHz-CSOM signal-to-noise ratio (SNR) is large because of the relatively large intensity of reflected light from the surface of the ferroelectric film. **Figure 65**(b) shows the fainter GHz-ANSOM response which is sensitive only to an approximate 50 nm x 50 nm area on the sample.

The low SNR of the GHz-ANSOM response necessitates long integration times, and a lock-in output filter setting TC (time constant) =300 ms, 6 dB/octave is typically used for these experiments. As a consequence, the acquisition of two-dimensional images can be time-consuming: about 5 hours are required to acquire a single 256 by 256 pixel image. During this time, thermal drifts between tip and sample can be non-negligible. To reduce the impact that these drifts can have on obtaining time-domain information, an interleaving method is implemented in which successive lines of the scans are taken at a sequence of different microwave delays[39]. Figure 66 (a-d) show four of sixteen GHz-ANSOM images obtained from this interleave method. The entire image shown (600 nm x 600 nm) is comparable to the resolution that can be obtained using diffraction-limited optics, and shows that there is significant inhomogeneity in the dynamic response at sub-100 nm scales. Variations in both the magnitude and phase (local dielectric loss) of the electrooptic response are summarized in Figure 66 (e,f), respectively. The magnitude of the response appears to be dominated by filamentary regions that may be associated with non-180° domain walls. The existence of microwave resonances associated with such walls was predicted by Arlt[120], but there has not been any direct evidence for this behavior. Variations in the phase of the electrooptic response (Figure 66(f)) indicate that polar contributions to dielectric loss are highly localized. Even taking into account

180° changes in phase associated with anti-parallel domains, there are significant local shifts that appear to be governed by local dispersive effects.

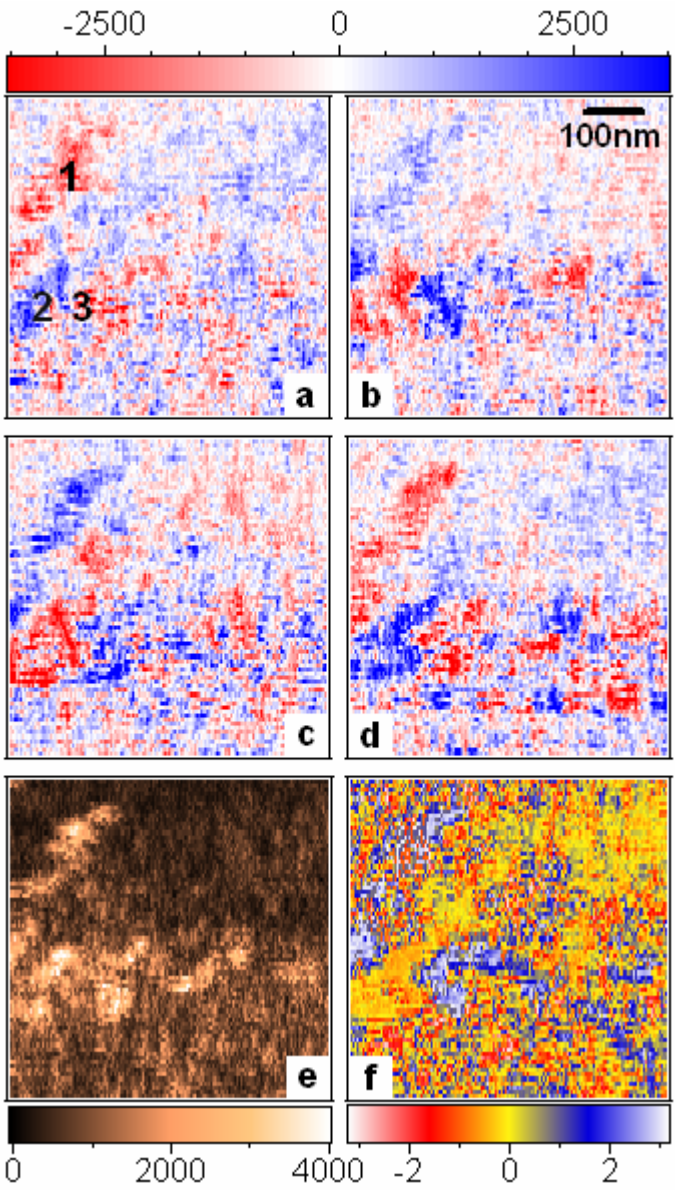

Figure 66. (a-d) are retrieved GHz-ANSOM images at microwave delay 0, 150, 240 and 390ps. At location 1,2,3, data is averaged over 20 nm x 20 nm to plot versus delay. Microwave frequency f=2.36GHz (corresponding to n=31). (e,f) Parameters from fitted curves based on Eq. (53). (e) electro-optic response strength for field at f=2.36GHz. (f) electro-optic response phases to field at f =2.36GHz.

By analyzing the temporal behavior over small regions (20 nm x 20 nm) of the image, one can compare the temporal response more directly. Figure 67(a-c) show the averaged GHz-ANSOM response of three areas selected from Figure 66(a) and locations 1-3. There are clear local differences in the phase of the response to uniform microwave driving at the nanoscale. These dynamics are clearly important for understanding switching dynamics at the nanoscale.

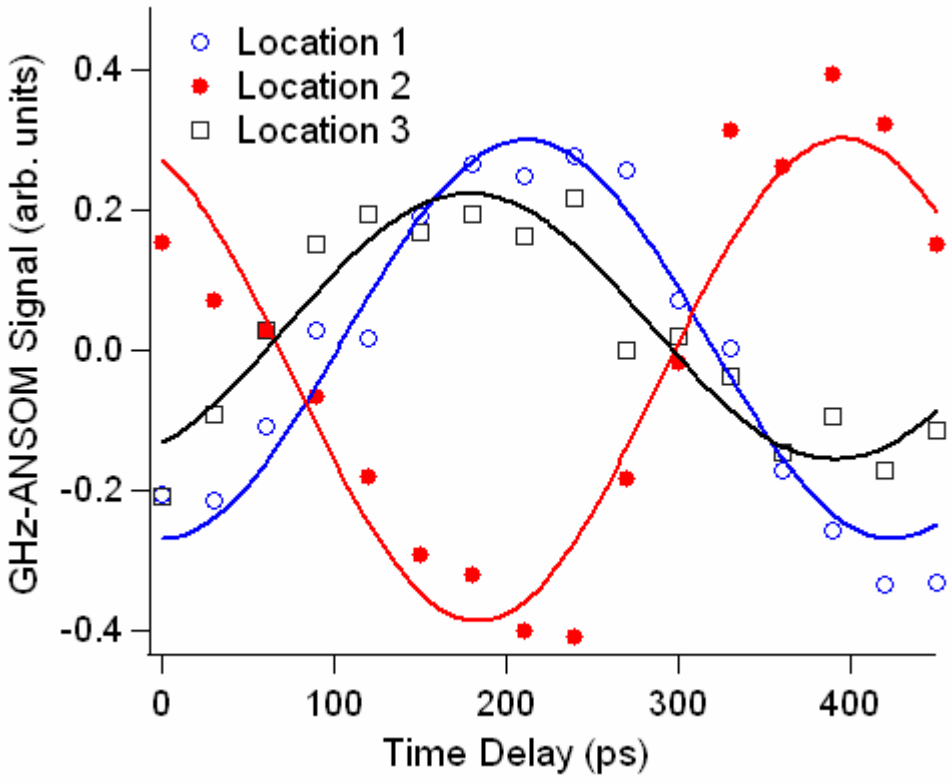

Figure 67. Localized GHz-ANSOM response versus microwave delay at three separate locations, representing averages over 20 nm x 20 nm regions. At each location, as indicated in Figure 66(a), sixteen different time delays are given; the solid lines show sinusoidal fits to the data.

In summary, we have demonstrated that a GHz-ANSOM system was developed to study thin film ferroelectric domain dynamics. Images at discrete phases of electric field at microwave frequencies were obtained with size similar to that of diffraction limited optical spot. Sub-

100nm spatial and sub-picosecond temporal resolution were achieved. A phase modulation scheme was implemented so that the electro-optical signal can be decoupled from topographic features. The experiment results also give direct evidence to existence of nano scale ferroelectric domains.

BIBLIOGRAPHY

[1] H.A. Jahn and E. Teller, "Stability of Polyatomic Molecules in Degenerate Electronic State. I. Orbital Degeneracy," Proc. Roy. Soc. Lon. Series A **161**, 220 (1937).

[2] C Kittel, *Introduction to Solid State Physics*, 8th ed. (John Wiley & Sons, Inc., 2005).

[3] R.H. Lyddane, R.G. Sachs, and E. Teller, "On the Polar Vibration of Alkali Halides," Phys. Rev. **59**, 673 (1941).

[4] J.F. Nye, *Physical Properties of Crystals*. (Oxford at the Clarendon Press, 1976), p.321.

[5] S. B. Lang, "Pyroelectricity: From ancient curiosity to modern imaging tool," Physics Today **58** (8), 31 (2005).

[6] B. Naranjo, J. K. Gimzewski, and S. Putterman, "Observation of nuclear fusion driven by a pyroelectric crystal," Nature **434** (7037), 1115 (2005).

[7] Jeffrey Geuther, Yaron Danon, and Frank Saglime, "Nuclear Reactions Induced by a Pyroelectric Accelerator," Physical Review Letters **96** (5), 054803 (2006).

[8] S. B. Lang, *Modern Bioelectricity*. (A. A. Marino, ed., Marcel Dekker Inc,, New York, 1988).

[9] H. Barkhausen, Z. Phys **20**, 401 (1919).

[10] R. R. Newton, A. J. Ahearn, and K. G. McKay, "Observation of the Ferro-Electric Barkhausen Effect in Barium Titanate," Physical Review **75** (1), 103 LP (1949).

[11] Eugene V. Colla, Lambert K. Chao, and M. B. Weissman, "Barkhausen Noise in a Relaxor Ferroelectric," Physical Review Letters **88** (1), 017601 (2001).

[12] A. G. Chynoweth, "Barkhausen Pulses in Barium Titanate," Physical Review **110** (6), 1316 LP (1958).

[13] Walter J. Merz, "Domain Formation and Domain Wall Motions in Ferroelectric $BaTiO_3$ Single Crystals," Phys. Rev. J1 - PR **95** (3), 690 LP (1954).

[14] Walter J. Merz, "Domain Formation and Domain Wall Motions in Ferroelectric BaTiO_{3} Single Crystals," Physical Review **95** (3), 690 LP (1954).

[15] David D Nolte, *Photorefractive effect and materials*. (Kluwer Academic Publishers, 1995).

[16] M. Dawber, K. M. Rabe, and J. F. Scott, "Physics of thin-film ferroelectric oxides," Rev. Mod. Phys. **77**, 1083 (2005).

[17] V. Y. Shur, E. L. Rumyantsev, E. V. Nikolaeva et al., "Formation and evolution of charged domain walls in congruent lithium niobate," Applied Physics Letters **77** (22), 3636 (2000).

[18] P. Paruch, T. Tybell, and J. M. Triscone, "Nanoscale control of ferroelectric polarization and domain size in epitaxial $Pb(Zr_{0.2}Ti_{0.8})O_3$ thin films," Appl. Phys. Lett. **79** (4), 530 (2001).

[19] T. Tybell, P. Paruch, T. Giamarchi et al., "Domain Wall Creep in Epitaxial Ferroelectric $Pb(Zr_{0.2}Ti_{0.8})O_3$ Thin Films," Phys. Rev. Lett. **89**, 097601 (2002).
[20] Hiromoto Uwe and Tunetaro Sakudo, "Stress-induced ferroelectricity and soft phonon modes in $SrTiO_3$," Phys. Rev. B J1 - PRB **13** (1), 271 LP (1976).
[21] N. A. Pertsev, A. G. Zembilgotov, and A. K. Tagantsev, "Effect of Mechanical Boundary Conditions on Phase Diagrams of Epitaxial Ferroelectric Thin Films," Physical Review Letters **80** (9), 1988 LP (1998).
[22] S. K. Streiffer, J. A. Eastman, D. D. Fong et al., "Observation of Nanoscale 180 degree Stripe Domains in Ferroelectric $PbTiO_3$ Thin Films," Physical Review Letters **89** (6), 067601 (2002).
[23] H. P. Sun, W. Tian, X. Q. Pan et al., "Evolution of dislocation arrays in epitaxial $BaTiO_3$ thin films grown on (100) $SrTiO_3$," Appl. Phys. Lett. **84** (17), 3298 (2004).
[24] K. J. Choi, M. Biegalski, Y. L. Li et al., "Enhancement of ferroelectricity in strained $BaTiO_3$ thin films," Science **306** (5698), 1005 (2004).
[25] K. A. Muller and H. Burkard, "$SrTiO_3$: An intrinsic quantum paraelectric below 4 K," Physical Review B **19** (7), 3593 LP (1979).
[26] J. H. Haeni, P. Irvin, W. Chang et al., "Room-temperature ferroelectricity in strained $SrTiO_3$," Nature **430** (7001), 758 (2004).
[27] W. T. Chang, C. M. Gilmore, W. J. Kim et al., "Influence of strain on microwave dielectric properties of (Ba,Sr)TiO_3 thin films," J. Appl. Phys. **87** (6), 3044 (2000).
[28] W. J. Kim, H. D. Wu, W. Chang et al., "Microwave dielectric properties of strained $(Ba_{0.4}Sr_{0.6})TiO_3$ thin films," J. Appl. Phys. **88** (9), 5448 (2000).
[29] V. Vaithyanathan, J. Lettieri, W. Tian et al., "c-axis oriented epitaxial $BaTiO_3$ films on (001) Si," J. Appl. Phys. **100** (2) (2006).
[30] F. Xu, S. Trolier-McKinstry, W. Ren et al., "Domain wall motion and its contribution to the dielectric and piezoelectric properties of lead zirconate titanate films," Journal of Applied Physics **89** (2), 1336 (2001).
[31] G. Binnig, C.F. Quate, and Ch. Gerber, "Atomic Force Microscope," Physical Review Letters **58** (9), 930 (1982).
[32] F. J. Giessibl, S. Hembacher, H. Bielefeldt et al., "Subatomic features on the silicon (111)-(7x7) surface observed by atomic force microscopy," Science **289** (5478), 422 (2000).
[33] F. J. Giessibl, "Atomic-Resolution of the Silicon (111)-(7x7) Surface by Atomic-Force Microscopy," Science **267** (5194), 68 (1995).
[34] Adam Foster, "PhD. Thesis."
[35] F. London, "The general theory of molecular forces," Trans. Farady Soc. **33**, 8 (1937).
[36] F. J. Giessibl, "Forces and frequency shifts in atomic-resolution dynamic-force microscopy," Physical Review B **56** (24), 16010 (1997).
[37] S. Rozhok, P. Sun, R. Piner et al., "AFM study of water meniscus formation between an AFM tip and NaCl substrate," Journal of Physical Chemistry B **108** (23), 7814 (2004).
[38] F. J. Giessibl, "Atomic resolution on Si(111)-(7x7) by noncontact atomic force microscopy with a force sensor based on a quartz tuning fork," Applied Physics Letters **76** (11), 1470 (2000).
[39] J. Levy, C. Hubert, and A. Trivelli, "Ferroelectric polarization imaging using apertureless near-field scanning optical microscopy," Journal of Chemical Physics **112** (18), 7848 (2000).

[40] J. Levy, "Quantum-information processing with ferroelectrically coupled quantum dots," Phys. Rev. A **64**, 052306 (2001).
[41] Max Born and Emil Wolf, *Principles of Optics*, 7 ed. (Cambridge University Press, Cambridge, 2002).
[42] C. Hubert, J. Levy, A. C. Carter et al., "Confocal scanning optical microscopy of $Ba_xSr_{1-x}TiO_3$ thin films," Appl. Phys. Lett. **71** (23), 3353 (1997).
[43] Oleg Tikhomirov, Hua Jiang, and Jeremy Levy, "Local Ferroelectricity in $SrTiO_3$ Thin Films," Physical Review Letters **89** (14), 147601 (2002).
[44] O. Tikhomirov, B. Red'kin, A. Trivelli et al., "Visualization of 180 degrees domain structures in uniaxial ferroelectrics using confocal scanning optical microscopy," J. Appl. Phys. **87** (4), 1932 (2000).
[45] O. Tikhomirov and J. Levy, "Study of the ferroelectric domain structure and phase transitions by confocal scanning optical microscopy," Ferroelectrics **292**, 161 (2003).
[46] W Denk, J.H. Strickler, and W.W Webb, "Two-Photon Laser Scanning Fluorescence Microscopy," Science **248** (4951), 73 (1990).
[47] E. Yablonovitch and R. B. Vrijen, "Optical projection lithography at half the Rayleigh resolution limit by two-photon exposure," Optical Engineering **38** (2), 334 (1999).
[48] T. B. Pittman, Y. H. Shih, D. V. Strekalov et al., "Optical imaging by means of two-photon quantum entanglement," Physical Review A **52** (5), R3429 LP (1995).
[49] T. B. Pittman, D. V. Strekalov, D. N. Klyshko et al., "Two-photon geometric optics," Physical Review A **53** (4), 2804 LP (1996).
[50] Agedi N. Boto, Pieter Kok, Daniel S. Abrams et al., "Quantum Interferometric Optical Lithography: Exploiting Entanglement to Beat the Diffraction Limit," Physical Review Letters **85** (13), 2733 LP (2000).
[51] R. Dorn, S. Quabis, and G. Leuchs, "Sharper focus for a radially polarized light beam," Physical Review Letters **91** (23) (2003).
[52] Volker Westphal and Stefan W. Hell, "Nanoscale Resolution in the Focal Plane of an Optical Microscope," Physical Review Letters **94** (14), 143903 (2005).
[53] F. Zenhausern, M. P. O'Boyle, and H. K. Wickramasinghe, "Apertureless near-field optical microscope," Appl. Phys. Lett. **65** (13), 1623 (1994).
[54] B. Knoll and F. Keilmann, "Scanning microscopy by mid-infrared near-field scattering," Applied Physics a-Materials Science & Processing **66** (5), 477 (1998).
[55] B. Knoll and F. Keilmann, "Near-field probing of vibrational absorption for chemical microscopy," Nature **399** (6732), 134 (1999).
[56] B. Knoll and F. Keilmann, "Enhanced dielectric contrast in scattering-type scanning near-field optical microscopy," Optics Communications **182** (4-6), 321 (2000).
[57] R. Hillenbrand and F. Keilmann, "Complex optical constants on a subwavelength scale," Physical Review Letters **85** (14), 3029 (2000).
[58] J.D. Jackson, *Classical Electrodynamics*, 3rd ed. (John Wiley & Sons, Inc., 1998).
[59] Craig F. Bohren and Donald R. Huffman, *Absorption and Scattering of Light by Small Particles*. (John Wiley & Sons, 1983).
[60] P. J. Schuck, D. P. Fromm, A. Sundaramurthy et al., "Improving the mismatch between light and nanoscale objects with gold bowtie nanoantennas," Abstracts of Papers of the American Chemical Society **229**, U730 (2005).
[61] D. P. Fromm, A. Sundaramurthy, P. J. Schuck et al., "Gap-dependent optical coupling of single "Bowtie" nanoantennas resonant in the visible," Nano Letters **4** (5), 957 (2004); P.

Muhlschlegel, H. J. Eisler, O. J. F. Martin et al., "Resonant optical antennas," Science **308** (5728), 1607 (2005).
62 L. Novotny, E. J. Sanchez, and X. S. Xie, "Near-field optical imaging using metal tips illuminated by higher-order Hermite-Gaussian beams," Ultramicroscopy **71** (1-4), 21 (1998).
63 Y. Gilbert, R. Bachelot, A. Vial et al., "Photoresponsive polymers for topographic simulation of the optical near-field of a nanometer sized gold tip in a highly focused laser beam," Optics Express **13** (10), 3619 (2005).
64 "http://www.rp-photonics.com/encyclopedia.html."
65 K. Kotzebue, presented at the WESCON/60 Conference Record, 1960 (unpublished).
66 M. E. Lines and A. M. Glass, *Principles and Applications of Ferroelectrics and Related Materials*. (Clarendon, Oxford, 1977).
67 Rolf Landauer, "Electrostatic Considerations in $BaTiO_3$ Domain Formation during Polarization Reversal," J. Appl. Phys. **28** (2), 227 (1957).
68 R. E. Peierls, *Quantum Theory of Solids*. (Oxford University Press, London, 1955).
69 G. Gruner, "The dynamics of charge-density waves," Reviews of Modern Physics **60** (4), 1129 (1988).
70 B. D. Josephson, Phys. Lett. **1**, 251 (1962).
71 F. Saurenbach and B. D. Terris, "Imaging of ferroelectric domain walls by force microscopy," Appl. Phys. Lett. **56** (17), 1703 (1990).
72 O. Kolosov, A. Gruverman, J. Hatano et al., "Nanoscale visualization and control of ferroelectric domains by atomic force microscopy," Phys. Rev. Lett. **74** (21), 4309 (1995).
73 Robert C. Miller and Albert Savage, "Further Experiments on the Sidewise Motion of 180 deg Domain Walls in $BaTiO_3$," Phys. Rev. **115**, 1176 (1959).
74 Robert C. Miller and Gabriel Weinreich, "Mechanism for the Sidewise Motion of 180 deg Domain Walls in Barium Titanate," Phys. Rev. **117** (6), 1460 (1959).
75 S. Stemmer, S. K. Streiffer, W. Y. Hsu et al., "The influence of Pt and $SrTiO_3$ interlayers on the microstructure of $PbTiO_3$ thin films deposited by laser ablation on (001) MgO," Journal of Materials Research **10** (4), 791 (1995).
76 F. Xu, S. Trolier-McKinstry, W. Ren et al., "Domain wall motion and its contribution to the dielectric and piezoelectric properties of lead zirconate titanate films," Journal of Applied Physics **89** (2), 1336 (2001).
77 C. Hubert, J. Levy, T. V. Rivkin et al., "Nanopolar reorientation in ferroelectric thin films," Applied Physics Letters **79** (13), 2058 (2001).
78 R. M. Feenstra, J. A. Stroscio, J. Tersoff et al., "[Atom-selective imaging of the GaAs (110) surface]," Physical Review Letters **58** (12), 1192 (1987).
79 Because the observed results for in-plane and out-of-plane response are so similar, only results for the out-of-plane response are shown.
80 with a 6 dB/octave The lock-in amplifier (EG&G 5210) time constants were set to TC = 1 ms, corresponding to an equivalent-noise bandwidth of 250 Hz. Most of the activity observed fell within 50 Hz, and hence a sampling interval of dt=10 ms was chosen.
81 Alan V. Oppenheim, Ronald W. Schafer, and John R. Buck, *Discrete-time signal processing*, 2nd ed. (Prentice Hall, Upper Saddler River, NJ, 1998), p.p.465.
82 A. G. Chynoweth, "Radiation Damage Effects in Ferroelectric Triglycine Sulfate," Phys. Rev. **113**, 159 (1959).

[83] Thermal excitation over the Peierls barrier, known to be important for domain dynamics in real systems, is not included in this model.
[84] J. G. Bednorz and K. A. Muller, "$Sr_{1-x}Ca_xTiO_3$: An XY Quantum Ferroelectric with Transition to Randomness," Physical Review Letters **52** (25), 2289 LP (1984).
[85] M. Itoh, R. Wang, Y. Inaguma et al., "Ferroelectricity Induced by Oxygen Isotope Exchange in Strontium Titanate Perovskite," Physical Review Letters **82** (17), 3540 LP (1999).
[86] S. Hyun and K. Char, "Effects of strain on the dielectric properties of tunable dielectric $SrTiO_3$ thin films," Appl. Phys. Lett. **79** (2), 254 (2001).
[87] A. Antons, J. B. Neaton, K. M. Rabe et al., "Tunability of the dielectric response of epitaxially strained $SrTiO_3$ from first principles," Phys. Rev. B J1 - PRB **71** (2) (2005).
[88] Oleg Tikhomirov, Hua Jiang, and Jeremy Levy, "Local Ferroelectricity in SrTiO_{3} Thin Films," Physical Review Letters **89** (14), 147601 (2002).
[89] Eric Courtens, "Birefringence of $SrTiO_3$ Produced by the 105K Structural Phase Transition," Physical Review Letters **29** (20), 1380 LP (1972).
[90] Hiroki Hasebe, Yuhji Tsujimi, Ruiping Wang et al., "Dynamical mechanism of the ferroelectric phase transition of $SrTi^{18}O_3$ studied by light scattering," Physical Review B (Condensed Matter and Materials Physics) **68** (1), 014109 (2003).
[91] M. Yamaguchi, T. Yagi, R. Wang et al., "Light scattering study of the ferroelectric phase transition in $SrTi^{18}O_3$," Phys. Rev. B J1 - PRB **63** (17), 172102 (2001).
[92] R. S. Katiyar S. Gupta, "Temperature-dependent structural characterization of sol-gel deposited strontium titanate ($SrTiO_3$) thin films using Raman spectroscopy," Journal of Raman Spectroscopy **32** (10), 885 (2001).
[93] J. Petzelt, T. Ostapchuk, I. Gregora et al., "Dielectric, infrared, and Raman response of undoped $SrTiO_3$ ceramics: Evidence of polar grain boundaries," Phys. Rev. B J1 - PRB **64** (18), 184111 (2001).
[94] P. Kuzel, F. Kadlec, H. Nemec et al., "Dielectric tunability of $SrTiO_3$ thin films in the terahertz range," Appl. Phys. Lett. **88**, 182901 (2006).
[95] M. Misra, K. Kotani, I. Kawayama et al., "Observation of TO1 soft mode in $SrTiO_3$ films by terahertz time domain spectroscopy," Appl. Phys. Lett. **87**, 182909 (2005).
[96] A. A. Sirenko, C. Bernhard, A. Golnik et al., "Soft-mode hardening in $SrTiO_3$ thin films," Nature **404**, 373 (2000).
[97] Hongzhou Ma and Jeremy Levy, "GHz Apertureless Near-Field Scanning Optical Microscopy of Ferroelectric Nanodomain Dynamics," NanoLetters **6** (3), 341 (2006).
[98] M. D. Biegalski, Y. Jia, D. G. Schlom et al., "Relaxor ferroelectricity in strained epitaxial $SrTiO_3$ thin films on $DyScO_3$ substrates," Appl. Phys. Lett. **88** (19), 192907 (2006).
[99] www.azom.com.
[100] Y. L. Li, S. Choudhury, J. H. Haeni et al., "Phase transitions and domain structures in strained pseudocubic (100) $SrTiO_3$ thin films," Physical Review B (Condensed Matter and Materials Physics) **73** (18), 184112 (2006).
[101] O. Auciello, J. F. Scott, and R. Ramesh, "The physics of ferroelectric memories," Physics Today **51** (7), 22 (1998).
[102] Rainer Waser, *Nanoelectronics and information technology*. (Wiley, 2003).
[103] F. Amy, A. S. Wan, A. Kahn et al., "Band offsets at heterojunctions between SrTiO3 and BaTiO3 and Si(100)," Journal of Applied Physics **96** (3), 1635 (2004).

[104] K. J. Hubbard and D. G. Schlom, "Thermodynamic stability of binary oxides in contact with silicon," Journal of Materials Research **11** (11), 2757 (1996).
[105] P. S. Tang, D. J. Towner, A. L. Meier et al., "Low-voltage, polarization-insensitive, electro-optic modulator based on a polydomain barium titanate thin film," Applied Physics Letters **85** (20), 4615 (2004).
[106] D. A. Farias and J. N. Eckstein, "Dynamic electrooptic frequency shifter for pulsed light signals," Ieee Journal of Quantum Electronics **41** (1), 94 (2005).
[107] John A. Rodriguez, Keith Remack, Katsushi Boku et al., "Reliability Properties of Low-Voltage Ferroelectric Capacitors and Memory Arrays," IEEE Transactions on Device Materials Reliability **4** (3), 436 (2004).
[108] S. L. Miller and P. J. McWhorter, "Physics of the Ferroelectric Nonvolatile Memory Field-Effect Transistor," Journal of Applied Physics **72** (12), 5999 (1992).
[109] C. A. P. Dearaujo, J. D. Cuchiaro, L. D. McMillan et al., "Fatigue-Free Ferroelectric Capacitors with Platinum-Electrodes," Nature **374** (6523), 627 (1995).
[110] W. L. Warren, D. Dimos, and R. M. Waser, "Degradation mechanisms in ferroelectric and high-permittivity perovskites," MRS Bulletin **21** (7), 40 (1996).
[111] B. H. Park, B. S. Kang, S. D. Bu et al., "Lanthanum-substituted bismuth titanate for use in non-volatile memories," Nature **401** (6754), 682 (1999).
[112] D. W. Pohl, W. Denk, and M Lanz, "Optical Stethoscopy," Appl. Phys. Lett. **44**, 651 (1984).
[113] E. Betzig, J. K. Trautman, T. D. Harris et al., "Breaking the diffraction barrier: optical microscopy on a nanometric scale," Science **251** (5000), 1468 (1991).
[114] J. Levy, V. Nikitin, J. M. Kikkawa et al., "Spatiotemporal near-field spin microscopy in patterned magnetic heterostructures," Phys. Rev. Lett. **76** (11), 1948 (1996).
[115] C. Hubert and J. Levy, "Nanometer-scale imaging of domains in ferroelectric thin films using apertureless near-field scanning optical microscopy," Applied Physics Letters **73** (22), 3229 (1998).
[116] H. K. Wickramasinghe and C. C. WIlliams, Patent No. 4,947,034 (April 1989 1989).
[117] F. Zenhausern, Y. Martin, and H. K. Wickramasinghe, "Scanning interferometric apertureless microscopy: optical imaging at 10 angstrom resolution," Science **269** (5227), 1083 (1995).
[118] K. R. Carroll, J. M. Pond, D. B. Chrisey et al., "Microwave measurement of the dielectric constant of $(Sr_{0.5}Ba_{0.5})TiO_3$," Appl. Phys. Lett. **62** (15), 1845 (1993).
[119] C. Hubert and J. Levy, "New optical probe of GHz polarization dynamics in ferroelectric thin films," Review of Scientific Instruments **70** (9), 3684 (1999).
[120] G. Arlt, U. Bottger, and S. Witte, "Emission of GHz shear waves by ferroelastic domain walls in ferroelectrics," Appl. Phys. Lett. **63** (5), 602 (1993).